IMPERIAL COLLEGE LONDON

Department of Earth Science and Engineering

Centre for Petroleum Studies

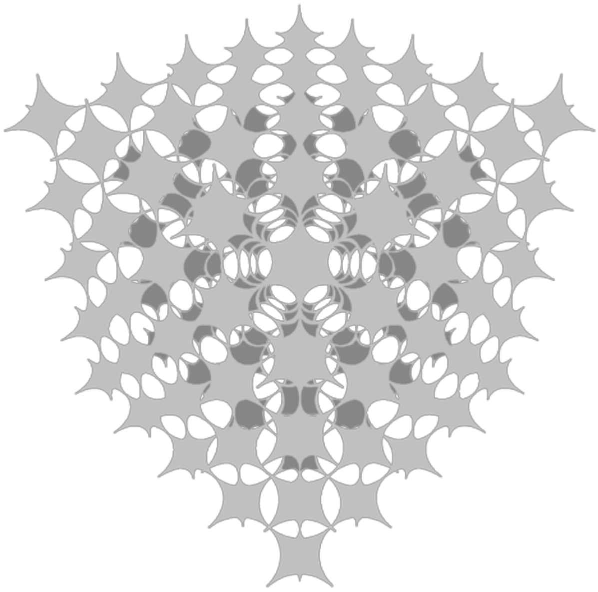

Directional measures to characterize anisotropy in pore-scale morphology and permeability

By

Lukas Mosser

A report submitted in partial fulfilment of the requirements for the MSc and/or the DIC

August 2016

DECLARATION OF OWN WORK

I declare that this thesis

"Directional measures to characterize anisotropy
in pore-scale morphology and permeability"

is entirely my own work and that where any material could be construed as the work of others, it is fully cited and referenced, and/or with appropriate acknowledgement given.

Signature:...
Name of student:... ....
Name of supervisor:...

Acknowledgment

Abstract

The ability of fluids to flow through reservoir rocks is a critical component in the process of recovering oil and gas from subsurface hydrocarbon accumulations. The formation of hydrocarbon bearing reservoirs is attributed to the deposition of siliciclastic grains or carbonate components followed by burial and diagenesis. Their ability to transport fluids is a function of these depositional environments and can be described on a variety of length scales. At the pore scale, modern solvers for the (Navier)-Stokes equations allow to evaluate intrinsic permeability on segmented high resolution Micro-CT images of individual samples. To integrate pore scale information in core, sector or field scale studies, upscaling of pore scale permeability is necessary. Knowledge about the existence of anisotropy in pore scale flow properties can have critical implications for processes occurring at the macro-scale.

This thesis aims to evaluate existing anisotropy at the pore scale by applying directional measures of statistical variation and pore-space morphology. The covariance was estimated directionally to investigate the possible existence of variation in REV size and pore geometry. We introduce a tensorial extension of Minkowski functionals allowing evaluation of orientational characteristics in the grain-void interface. These directional measures are shown to be physically well-defined and are directly related to the seminal work of Kozeny (1927) and Carman (1937, 1939).

Our results show that directional estimates of covariance can be used to evaluate pore-scale variation such as periodicity indicating the possible existence of stratification and gain information about the existence of REVs of different size in different directions. Directional estimates of the characteristic pore and mean grain size allow a qualitative estimate of the principal directions of flow. Evaluation of the surface orientation in the available samples using Minkowski tensors allows evaluation of REV size and variation in preferred surface orientation. By comparing numerical estimates of permeability and applying the theory of Bear and Bachmat (1986, 1990) we obtain directional estimates of the tortuosity factors for a variety of siliciclastic and carbonate samples. Our findings show that Minkowski tensors present a sensitive measure of anisotropy and can be applied to gain qualitative information on the existence of anisotropy at the pore scale as well as the preferred directions of flow.

Table of contents

List of Figures

List of Tables

Imperial College
London

Directional measures to characterize anisotropy in pore-scale morphology and flow properties

Lukas Mosser

Professor Olivier Dubrule, Professor Martin J. Blunt

Abstract

The ability of fluids to flow through sedimentary rocks is a critical component in the process of recovering oil and gas from subsurface hydrocarbon accumulations. The formation of hydrocarbon bearing reservoirs is attributed to the deposition of siliciclastic grains or carbonate components followed by burial and diagenesis. Their ability to transport fluids is a function of these depositional environments and can be described on a variety of length scales. At the pore scale, modern solvers for the (Navier)-Stokes equations allow to evaluate intrinsic permeability on segmented high resolution Micro-CT images of individual samples. To integrate pore scale information in core, sector or field scale studies, upscaling of pore scale permeability is necessary. Knowledge about the existence of anisotropy in pore scale flow properties can have critical implications on effective recovery strategies of oil and gas reservoirs.

This thesis aims to evaluate existing anisotropy at the pore scale by applying directional measures of statistical variation and pore-space morphology. The covariance was estimated directionally to investigate the possible existence of variation in REV size and pore geometry. We introduce a tensorial extension of Minkowski functionals allowing evaluation of orientational characteristics in the grain-void interface. These directional measures are shown to be physically well-defined and are directly related to the seminal work of Kozeny (1927) and Carman (1937, 1939).

Our results show that directional estimates of the covariance can be used to evaluate pore-scale variation such as periodicity indicating the possible existence of stratification and gain information about the existence of REVs of different size in different directions. Directional estimates of the characteristic pore and mean grain size allow a qualitative estimate of the principal directions of flow. Evaluation of the anisotropy in surface orientation in the available Micro-CT images using Minkowski tensors allows evaluation of REV size and variation in surface orientation. By comparing numerical estimates of permeability and applying the theory of Bear and Bachmat (1986, 1990) we obtain directional estimates of the tortuosity factors for a variety of siliciclastic and carbonate samples. Our findings show that Minkowski tensors present a sensitive measure of anisotropy in pore morphology and can be applied to gain qualitative information on the existence of anisotropy at the pore scale as well as the preferred directions of flow.

Introduction

Many factors governing the success of hydrocarbon exploration projects can be attributed to petrophysical properties of hydrocarbon saturated reservoir rocks. As fluids are transported from the high pressure reservoir to a low pressure well their preferred path of least resistance is highly dependent on the heterogeneities and anisotropies present in the reservoir. Depending on the recovery mechanisms applied to maximise recovery, such as secondary recovery by water flooding or tertiary methods, information on the presence of these heterogeneities can have major implications on the application of these methods.

On the field scale, anisotropies in reservoir properties can be identified using modern methods in seismic processing. Seismic attributes allow the identification of regional variations in mechanical properties of reservoir rock. These variations can be introduced in integrated reservoir modelling approaches to distinguish reservoir facies. These are linked with characteristic petrophysical property distributions gained from RCAL and SCAL analysis. Modern geostatistical methods allow the interpretation of ensembles of reservoir models to evaluate uncertainty inherent in the interpretation of the available data. To decrease the uncertainty, it is possible to incorporate pressure transient and production data in a history matching workflow.

To maximise recovery, enhanced oil recovery methods may be applied to increase production. To effectively apply many EOR methods another length scale of a porous medium must be investigated. The pore scale, defined as the scale where individual grains and fluid filled gas filled pores may be distinguished. The pore scale plays an important role in maximising the recovery of hydrocarbons beyond residual saturations. From viscous and capillary force balance it can be shown that these residual saturations are functions of pore geometry, wettability characteristics of the grain surfaces and fluid properties. Modern Micro-CT technology has made it possible to investigate these discplacement processes and analyse the controlling mechanisms

A variety of methods have been introduced in the analysis of pore scale morphology to characterise material properties of porous media such as porosity, grain size distributions or connectivity. To quantify single-phase and two-phase flow properties of sedimentary rocks at the pore scale, modern numerical solvers for the (Navier-) Stokes equations have been developed. Modern computational resources allow average single-phase flow properties to be determined in reasonable time. Obtaining directional estimates of permeability from high resolution Micro-CT images is a time and resource consuming process.
This thesis aims to evaluate two statistical measures that allow to determine the existence of anisotropy in a porous medium. Applied as a preprocessing step in a conventional upscaling workflow these methods help to identify directional variation in static and flow properties before applying computationally expensive methods to evaluate petrophysical properties at the pore scale. The integration of this data into modern upscaling and integrated reservoir modeling processes allows uncertainty to be reduced due to increased knowledge on anisotropy present in oil and gas reservoirs.

This thesis is structured as follows. We begin by highlighting relevant concepts derived from the seminal work of Guimer (1955) and Debye, Anderson, and Brumberger (1957) to introduce the covariance as a measure of the variance in pore morphology. Using simple geometric bodies and parametric models we introduce the concept of tensorial Minkowski functionals and their applications to characterise anisotropy in random porous media. These tensors measure the shape and orientation of geometric bodies and are a natural extension of the well-known scalar Minkowski functionals, volume, surface area, integral of mean curvature and the euler characteristic.

Seventeen Micro-CT images of sedimentary rock have been studied to evaluate the applicability of the suggested methods. By applying the directional extension of the covariance we evaluate anisotropic characteristics of sedimentary rocks and evaluate the qualitative implications on single-phase fluid flow. Triangulated representations of the grain-void interface allow us to evaluate Minkowski tensors and their variation as a function of the image size. This allows us to evaluate the applicability of these measures to quantify anisotropy in the studied samples. By linking tensorial Minkowski functionals to the macroscopic momentum balance introduced by Bear and Bachmat (1986, 1990) we estimate single-phase permeability and compare our results to numerical estimates of the directional permeability obtained from solution of the Stokes equations on binary representations of each sample.

Literature Review

Direct measurements of the effective permeability of porous media can be traced back to the experiments of D'Arcy (1856) to estimate permeability of soils. Indirect measurement of material properties of porous media using two-point probability functions can first be attributed to Guimer (1955). Later theoretical and experimental work by Debye, Anderson, and Brumberger (1957) on the scattering of X-Rays has shown that two-point probability functions provide the means to characterise key properties of random materials such as the specific surface area. A number of publications emphasize the physical relevance of two-point probability functions by showing that they arise in the description of effective properties governing a wide range of physical processes (S Torquato 1997) (Prager 1961).

Spatial statistics in the context of porous media with application to fluid flow problems were first considered by Matheron. While not only developing many image morphological concepts (Matheron 1975) his work on the estimation of the effective permeability of a porous medium (Matheron 1967) and his definition of a representative elementary volume or REV have revolutionised the characterisation of random materials with regards to flow in porous media. Based on Matherons seminal work a number of approaches have been developed to quantify bounds on the effective permeability of random materials (Rubinstein and Torquato 1989). Today, the general theory of deriving effective properties by volume averaging methods extends far beyond the field of flow in porous media.. The general theory of random materials (S. Torquato 2002) aggregates methods to characterise and quantify effective properties and provides a rigorous mathematical and physical foundation for application in materials science.

The mathematical methods of modelling and characterising the spatial distribution and morphology of objects are an active field of research in the more general concept of stochastic geometry (Stoyan, Kendall, and Mecke 1995). Many of the models developed in the context of stochastic geometry such as the Boolean model (Clausius 1858; Serra 1987) provide proxies for the description of natural random arrangements of objects and their statistical properties (Jacod and Joathon 1972). In earth sciences many concepts such as angularity or sphericity of clastic grains can be described using image morphological methods and stochastic geometry (Serra 1982).

The covariance and its related covariance functions have been widely applied in stereological applications. Image stereological relations allow volumetric material properties to be related to two dimensional estimates of the covariance. For three-dimensional heterogeneous and isotropic media it has been shown that the covariance is related to the specific surface area (Guimer 1955; Debye, Anderson, and Brumberger 1957).

The same relationship has been proven for the case of angular averaged estimates of the covariance for the case of anisotropic media (Berryman 1987). For the case of anisotropic media where averaging is not performed, coefficients can be obtained from integral geometric analysis (Gokhale, Tewari, and Garmestani 2005). These approaches allow determination of the specific surface area for a large variety of heterogeneous isotropic and anisotropic materials and therefore obtain an estimate of the effective permeability via the theory of Kozeny (1927) and Carman (1937, 1939).

Kozeny established a theoretical framework for estimating the permeability of a porous medium by deriving an analytical model for the permeability of a bundle of tubes. Carman later expanded on the work of Kozeny by evaluating Kozeny's method with available measurement data and estimating the range of validity of his equation. This early work of Carman provides an excellent compendium of experimental and analytical approaches to estimate the permeability of granular beds. A number of variations of empirical and analytical Kozeny-Carman equations exist (Chapuis and Aubertin 2003). Analytical models of the permeability of dilute and non-dilute beds of spheres have been developed and can be used to compare numerical or experimental measurements of permeability to analytical data (Childress 1972; Howells 1974).

The macroscopic momentum balance approach by Bear and Bachmat (1986, 1990) allows definition of the permeability tensor of an arbitrary three-dimensional porous medium as a function of the porosity, tortuosity and a measure of surface orientation. For isotropic porous media their theory reduces to the Kozeny-Carman equation. Recent advances refining the macroscopic momentum balance approach have allowed new upper and lower bounds for the tortuosity to be defined (Guo 2012, 2015) using an analytical form of the tortuosity for anisotropic media based on an orientation tensor of void space in a porous medium (Pietruszczak and Krucinski 1989).

A number of methods to estimate the permeability of a porous medium numerically from volumetric representations have been developed. The two most common approaches to solve the (Navier-) Stokes equations include the Lattice Boltzmann method (Pan, Hilpert, and Miller 2001; 2004) as well as finite-difference or finite-volume methods. Recent developments in efficient Stokes solvers have made the direct solution of these equations possible direct on binary representations of the pore and void space (Mostaghimi, Blunt, and Bijeljic 2013). These binary images result from segmentation in the post-processing of Micro-CT samples of sedimentary rock.

The mathematical field of integral and stochastic geometry allows characterization of random geometric bodies and their arrangement, such as the structures found in natural materials. The simplest morphological measures are the four scalar Minkowski measures first derived from Hadwigers Theorem (Hadwiger 1957): the volume, surface area, the mean curvature and the euler characteristic. Evaluating these measures as a function of a variable length scale leads to a highly effective descriptor of geometric arrangements. This was shown by applying scalar Minkowski functionals to analyse the large scale structure of the universe (Mecke, Buchert, and Wagner 1994). An extension of scalar Minkowski functionals to vectorial and tensorial measures of orientation have been presented by (Schröder-Turk et al. 2010). These tensorial measures allow the evaluation of orientational distributions of closed and open surfaces. Interfaces of binary materials images of porous media obtained from Micro-CT scanners represent open surfaces. For open surfaces only a subset of the tensorial Minkowski measures is well defined. These so called translation invariant tensors i.e. their measurement is independent of a reference location have been considered in this study. The additive property of Minkowski functionals makes them robust estimators and allow efficient computation on arbitrary domains by parallelization (Schröder-Turk et al. 2013). Hörrmann et al. (2014) give analytical estimators of the tensorial Minkowski functionals in two-dimensions for the Boolean model which have been used to estimate the orientation and intensity parameters of an underlying anisotropic Boolean model.

A variety of applications have shown that these tensorial measures can be used to quantify changes in the anisotropy in the structure of materials (Kuhn, Sun, and Wang 2015). Mecke and Arns (2005) highlight the use of Minkowski functionals to compare various modelling approaches for random porous media and show that these integral geometric measures allow prediction of effective material properties. In the context of fluids in porous media, integrals of curvature of fluid interfaces occur in the prediction of critical points. Theoretical models to predict capillary condensation have been shown to depend on scalar Minkowski functionals (Mecke and Arns 2005). Tensorial translation invariant Minkowski tensors arise in the theory of the evolution of the interface of two mixing fluids without capillary tension (Wetzel and Tucker 1999). The surface integrals involved in the theory of Bear and Bachmat (1986) has been shown in this work to be closely related to tensorial Minkowski functionals as morphological estimates of surface orientation

Methodology

Micro-CT Images and Pre-Processing

To evaluate and compare pore space anisotropy of various sedimentary rock samples, seventeen Micro-CT images that have been previously acquired are analysed. Their size ranges from 300 to 500 voxels edge length and resolutions between 2 and 9 μm. These images have been studied previously in the context of pore network extraction and modeling and evaluated in terms of their static and dynamic petrophysical properties (Dong and Blunt 2009). We also refer the reader to appendix 6 where we present a summary of the properties of each sample. The acquired Micro-CT images have been segmented using Otsu method and are represented as binary phases the pore phase and the grain phase. All images are available in the public domain including static and dynamic single-phase flow properties (Bijeljic 2015). To reduce computational cost in the estimation of permeability five images have been down sampled from a resolution of 1000^3 voxels to 500^3 prior to being used in the analysis.

Covariance

Following the convention defined by Chiu et al. (2013) we introduce the covariance $C(r)$ (Equation 1) as a measure that characterises the probability that two points at a distance **r** lie within the same phase of the porous medium. To make results of various samples comparable we have normalized the results (Equation 2).

$$C(\boldsymbol{r}) = P(o \in \Xi, \boldsymbol{r} \in \Xi)\ for\ \boldsymbol{r}\ \in \mathbb{R}^d \ldots\ldots\ldots\ldots\ldots\ldots\ldots\ldots\ldots\ldots\ldots\ldots(1)$$

$$\hat{C}(r) = \frac{C(r)-\phi^2}{\phi(1-\phi)} \ldots\ldots\ldots\ldots\ldots\ldots\ldots\ldots\ldots\ldots\ldots\ldots\ldots\ldots(2)$$

We will highlight three important characteristics of the covariance: The covariance at the origin is equal to the porosity ϕ of the observed phase Ξ.. The limit of the Covariance as the distance $\boldsymbol{r}$ approaches infinity, stabilizes at ϕ^2. Finally, as shown by Debye, Anderson, and Brumberger (1957) the first derivative of the covariance at the origin is related to the specific surface area S_v (Equation 3). Ghokale has shown that the coefficient associated with the specific surface area varies in the case that radial averaging is not applied and the covariance must include a measure of the orientation aligned with the direction of observation (Equation 4).

$$\frac{dC(0)}{dr} = -\frac{S_v}{4}\ for\ \boldsymbol{r}\ \in \mathbb{R}^3 \ldots\ldots\ldots\ldots\ldots\ldots\ldots\ldots\ldots\ldots\ldots\ldots\ldots(3)$$

$$\lim_{r\to 0}\left(\frac{C(r,\theta,\phi)}{r}\right) = S_v \int_0^{2\pi}\int_0^{\frac{\pi}{2}} |\cos\beta|\, G(r,\theta',\phi')d\theta' d\phi'/2,\ where\ \beta \sphericalangle (\theta,\phi),(\theta',\phi') \ldots\ldots\ldots(4)$$

$$\boldsymbol{r}_{c,i} = \frac{\phi(1-\phi)}{-C\prime(0)_i} \ldots\ for\ \boldsymbol{i} \in \{\mathrm{x,y,z}\} \ldots\ldots\ldots\ldots\ldots\ldots\ldots\ldots\ldots\ldots\ldots(5)$$

This has important implications for the later analysis of the available data. While the covariance can be extended to give directional information, it is always related to the total specific surface area and therefore does not allow any additional knowledge to be gained in terms of directional effective properties. Nevertheless, the Covariance can be used as a valuable tool to characterise pore scale morphology in multiple directions. Two characteristics that can be deduced are the characteristic pore size $\boldsymbol{r}_c$ (Equation 5) and the mean grain size $\boldsymbol{r}_m$. We wil use $\boldsymbol{r}_{c,i}$ where the subindex i denotes one of the three Cartesian directions $i \in \{x, y, z\}$ to distinguish from radial averages $\bar{\boldsymbol{r}}_c$.

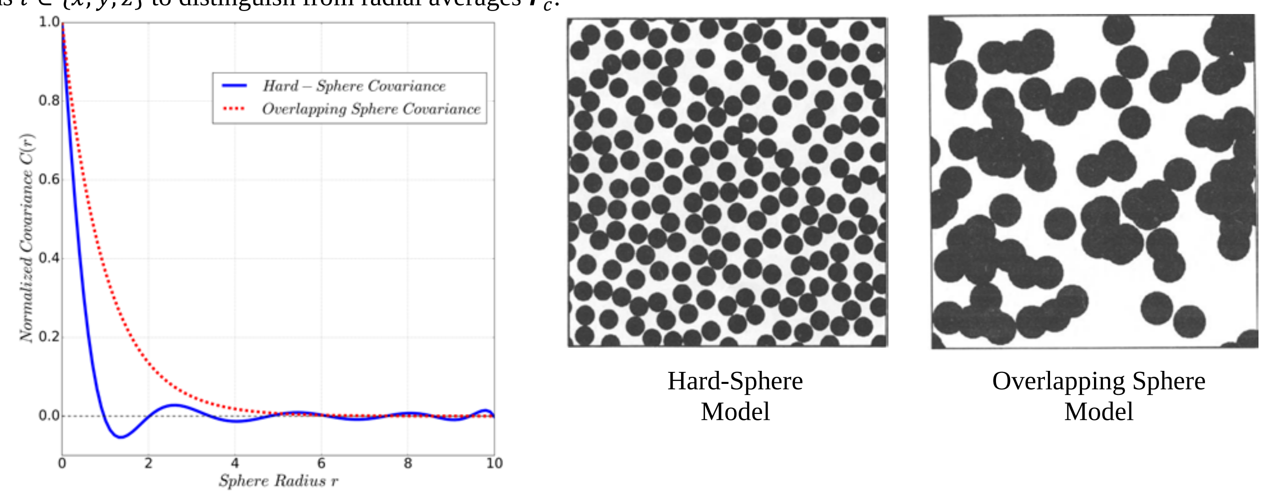

Figure 1: Comparison of the covariance for Hard-Sphere and Ovelapping Sphere Models ((Salvatore Torquato and Stell 1985)*. Illustriations reproduced from* Smith and Torquato (1988)

Furthermore, we can differentiate between qualitative shapes of the covariance. The existence of the so called “Hole-Effect” can indicate short scale order in a porous medium (Figure 1), which occurs due to volume exclusion effects and is typical in systems that can be modelled as non-overlapping spheres (Smith and Torquato 1988). Different shapes of the covariance in different directions indicate important directional differences in pore space morphology. The distance at which stabilization around ϕ^2 occurs is indicative of the size of the REV and may vary in different directions. If no stabilization occurs the true REV size has not been reached for the volume under investigation.

To obtain a directional estimate of the Covariance we follow the approach presented in (J[illegible] al. 2016). Computation of the covariance is therein performed along linear sections of the volumetric binary image in the direction of interest and averaged across all linear sections in that direction (Pant 2016). These algorithms and their implementations have been made available in the public domain (Appendix 5).

Scalar and Tensorial Minkowski Functionals

Minkowski functionals present valuable descriptors of pore space shape or morphology Mecke and Arns (2005). While the scalar Minkowski functionals allow mean values for a given porous medium to be obtained, tensorial Minkowski measures allow additional directional information to be gained. These have first been described by (Schröder-Turk et al. 2010) but are closely related to tensorial properties that arise in the mathematical description of physical processes involving interface problems such as mixing of two fluids (Wetzel and Tucker 1999) or characterisation of foams (Saadatfar et al. 2012).

We can define four scalar Minkowski functionals: volume, surface area, integral of mean curvature and the euler characteristic. It is important to note that due to the interface between pores and grains in sedimentary rocks typically being open surfaces i.e. the interface has disconnected edges, only translation invariant properties can be estimated.

Tensorial Minkowski functionals can be understood as indicators of how much of a scalar measure is oriented in the direction of observation. We will demonstrate this concept based on simple geometric objects. To better relate the scalar and tensorial Minkowski functionals we will use the notation defined by Schröder-Turk et al. (2010). Equation 6 represents the general equation from which all scalar, vectorial and tensorial Minkowski functionals can be derived. The sub index ν in equation 6 denotes the order of the scalar Minkowski functional whereas superscripts r, s relate to the exponents defined in the general form (Equation 6). To characterise pore space morphology two translation invariant tensors i.e. their estimation is independent of a reference location, have been considered. Due to mesh dependency effects only the first Minkowski tensor $W_1^{0,2}$ (Equation 8) can be applied (Appendix 4). It has been shown that the translation covariant tensor $W_1^{1,1}$ (Equation 14) is closely related to the tortuosity factor defined by Bear and Bachmat (1986). A normalization of $W_1^{0,2}$ by the surface area $W_1^{0,0}$ allows an intuitive interpretation of the first Minkowski tensor. This normalized tensor $\bar{W}_1^{0,2}$ represents the fraction of the total surface area oriented in the principal directions (Equation 9).

$$W_\nu^{r,s}(K) = \frac{1}{3}\int_{\partial K} G_\nu x^r n^s dA\, , \nu \ = \ 1, 2, 3 \ and \ (r,s) \ = \ (2,0), (1,1) \ or \ (0,2) \quad \ldots\ldots(6)$$

$$3W_1^{0,0}(K) = \int_{\partial K} dA \quad \ldots\ldots(7)$$

$$3W_1^{0,2}(K) = \int_{\partial K} \boldsymbol{n}^2 dA = \sum_i^{\#(Faces)} n_i n_j A_i \quad \ldots\ldots(8)$$

$$\bar{W}_1^{0,2}(K) = \frac{W_1^{0,2}(K)}{W_1^{0,0}(K)} = \frac{\int_{\partial K} \boldsymbol{n}^2 dA}{\int_{\partial K} dA} \quad \ldots\ldots(9)$$

$$\beta_1^{0,2} = \frac{\min\{eig(W_1^{0,2})\}}{\max\{eig(W_1^{0,2})\}} \quad \ldots\ldots(10)$$

An eigenvalue decomposition of $W_1^{0,2}$ has been used to define an index of anisotropy $\beta_1^{0,2}$ (Equation 10) which represents the ratio of the minimal and maximal eigenvalues. Combining the eigenvalues of $W_1^{0,2}$ with their respective eigenvectors these are interpreted as an oriented ellipsoid describing the directions and magnitude of anisotropy of the evaluated surface.

To illustrate the use of the first Minkowski tensor as a measure of anisotropy, a number of simple geometric bodies have been evaluated (Figure 2). The random bundle of non-intersecting tubes was chosen to resemble the theoretical model used to derive the Kozeny-Carman equation (Equation 11).

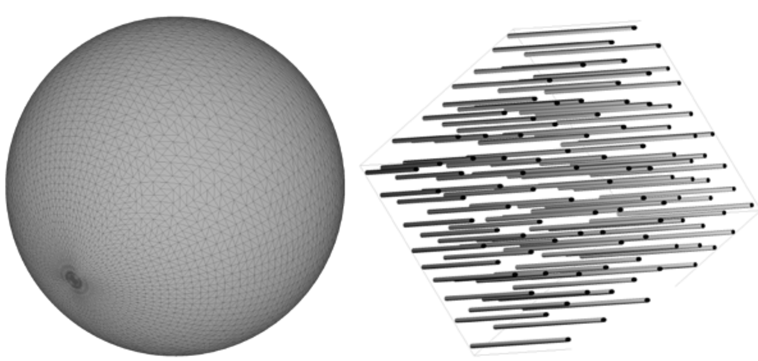

Figure 2: Triangulated representation of a sphere and bundle of tubes to illustrate Minkowski tensor valuations for simple geometric bodies.

	$\bar{W}_1^{0,2}$	$\beta_1^{0,2}$
Sphere	$\begin{bmatrix} 0.333 & 0 & 0 \\ 0 & 0.333 & 0 \\ 0 & 0 & 0.333 \end{bmatrix}$	1.0
Planes	$\begin{bmatrix} 1.0 & 0 & 0 \\ 0 & 0 & 0 \\ 0 & 0 & 0 \end{bmatrix}$	Not defined
Bundle of Tubes	$\begin{bmatrix} 0.5 & 0 & 0 \\ 0 & 0.5 & 0 \\ 0 & 0 & 0 \end{bmatrix}$	Not defined

Table 1: Minkowski tensors for a sphere, arrangement of parallel planes and a bundle of tubes.

Table 1 presents the first Minkowski tensor and the corresponding anisotropy index $\beta_1^{0,2}$ for the evaluated geometries. For a sphere the first Minkowski tensor shows pure axis aligned isotropy. This is emphasized by the anisotropy index being equal to one. Computing $\overline{W}_1^{0,2}$ for the arrangement of planar surfaces shows that the surface has only one primary orientation. Finally, the bundle of tubes is isotropic in the plane representing the base of the tubes and zero in the third direction as the tubes are open and therefore no surface area is oriented in this direction.

Anisotropic parametric models as pore-grain analogues

While simple geometric models such as spheres and bundles of tubes are able to highlight the most basic characteristics of the Minkowski tensors, all these models show isotropic behavior. To highlight the effect of anisotropy on the evaluated Minkowski tensor functionals and relate these simple models to the complex pore space found in sedimentary rocks a number of parametric models were derived. A NURBS (Non-Uniform-Rational-B-Spline) representation of an equally spaced array of spheroids was used to extract a pore-void interface that mimics the grain surfaces seen in natural sedimentary rocks. By rescaling two of the three axis aligned ellipsoids we introduce anisotropy into the geometry. A detailed description of the parametric modeling process can be found in appendix 3. We present here three parametric models of spheres and ellipsoids. By keeping the radius constant in the z-direction and reducing the radius of the ellipsoids in the x-y plane anisotropy is introduced between the x-y plane and the z-direction.

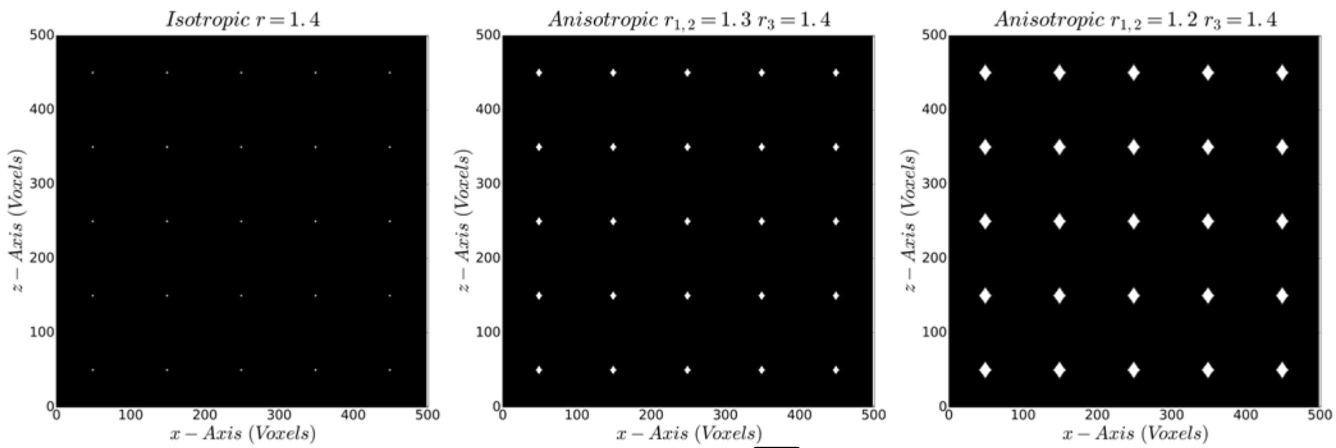

Figure 3: Isotropic and anisotropic models used to evaluate the influence of introduced anisotropy for an arrangement of equally spaced spheroids. X-Z Plane is shown where anisotropy increases from left to right.

Table 2 shows the resulting Minkowski tensors and anisotropy indices for the range of parametric models. We observe that the tensorial Minkowski functional indicates isotropic behavior in the x-y plane. Even though the change in the diameter is small this measure is highly sensitive and indicates significant anisotropy of the pore grain interface.

Where parametric description of boundary surfaces is possible, analytical equations of the Minkowski functionals can be derived. For pore-grain interfaces this is not possible and therefore computations must be performed on a triangulated approximation of the interface extracted from the binary Micro-CT images using a triangulation algorithm such as marching cubes (Figure 4) (Appendix 4)

	$\overline{W}_1^{0,2}$	$\beta_1^{0,2}$
Isotropic $r_{1,2,3} = 1.4$	$\begin{bmatrix} 0.333 & 0 & 0 \\ 0 & 0.333 & 0 \\ 0 & 0 & 0.333 \end{bmatrix}$	1.0
Anisotropic $r_{1,2} = 1.3$ $r_3 = 1.4$	$\begin{bmatrix} 0.361 & 0 & 0 \\ 0 & 0.361 & 0 \\ 0 & 0 & 0.277 \end{bmatrix}$	0.77
Anisotropic $r_{1,2} = 1.2$ $r_3 = 1.4$	$\begin{bmatrix} 0.382 & 0 & 0 \\ 0 & 0.382 & 0 \\ 0 & 0 & 0.235 \end{bmatrix}$	0.61

Table 2:Minkowski tensors of parametric pore-grain models

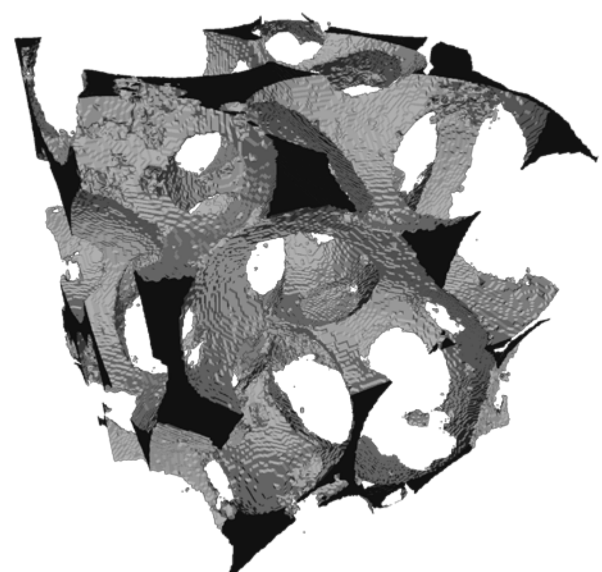

Figure 4: Extracted pore-grain interface of the Ketton sample

Numerical computation of directional permeability

The first analytical models to estimate permeability of a porous medium can be attributed to the seminal work of Kozeny (1927) and later Carman who verified and generalized Kozenys approach and compared it to experimental data for various grain size distributions. Kozenys original formulation (Appendix 1B) also introduced the concept of tortuosity and is considered as a measure of length of the true path a particle being transported through a porous medium takes. Equation 11 commonly referred to as the Kozeny-Carman equation allows estimation of the effective average permeability of a porous medium when the specific surface area and its tortuosity are known. For our purpose specific areas have been determined by evaluating the covariance (Equation 1) as well as from the computation of the scalar Minkowski functional $W_1^{0,0}$(Equation 7). The factor C_α is a shape factor depending on the shape of the pores and commonly assumed as $C_\alpha = 2$ for circular pores.

$$k_{eff} = \frac{\phi^3}{C_\alpha S_v^2 \tau^2} \quad (11)$$

Using a macroscopic momentum balance Bear and Bachmat (1986) derive a theoretical expression for the permeability tensor k_{ij} (Equation 12). Comparing the surface integrals appearing in their derivation we can see that the first Minkowski tensor $\overline{W}_1^{0,2}$ (Equation 9) appears in the parameter α_{ij} which incorporates the effect of orientation of the grain-fluid interface $S_{\alpha\beta}$ (Equation 13). Additionally, the expression of the tortuosity factor (Equation 15) can be expressed in terms of the translation co-variant Minkowski Tensor $W_1^{1,1}$ (Equation 14).

$$k_{ij} = \frac{\phi^3}{C_\alpha S_v^2} \alpha_{il}^{-1} T_{lj}^* = \frac{\phi^3}{C_\alpha S_v^2} \alpha_{ij}^{-1} \frac{1}{\tau^2} \quad (12)$$

$$\alpha_{ij} = \delta_{ij} - \frac{1}{S_{\alpha\beta}} \int n_\alpha^i n_\alpha^j dA = \delta_{ij} - \frac{\int_{S_{\alpha\beta}} n^2 dA}{\int_{S_{\alpha\beta}} dA} = \delta_{ij} - \overline{W}_1^{0,2} \quad (13)$$

$$3W_1^{1,1}(K) = \int_{\partial K} \boldsymbol{xn} dA \quad (14)$$

$$T_{ij}^* = \frac{1}{\phi V} \int x^i n^j dA = \frac{3W_1^{1,1}}{\phi V} \quad (15)$$

By computing numerical estimates of the permeability in the three axis aligned directions direct on the segmented binary image of the pore space (Mostaghimi, Blunt, and Bijeljic 2013) we are able to compare numerical results of the permeability with estimates derived from the theory of Bear and Bachmat incorporating the use of the first Minkowski Tensor $\overline{W}_1^{0,2}$. This allows us to estimate the factor $C_\alpha \tau^2$ (Equation 16) which can later be used e.g. to obtain an empirical relationship for the directional permeability without the need to compute the directional permeability using computationally expensive numerical methods.

$$C_\alpha \tau^2 = \frac{\phi^3}{C_\alpha S_v^2 k_{ij}} \alpha_{ij}^{-1} \quad (16)$$

Results

For this study seventeen Micro-CT images have been analysed in terms of their directional static characteristics as well as their single-phase permeability. To highlight the use of the covariance and Minkowski tensors as measures of pore space anisotropy, we will consider three distinctive samples (Figure 5). Beadpack is an artificial sample of ceramic grains with a diameter of 100 μm. Ketton represents an oolitic limestone with spheroidal grains, whereas Estaillades is a complex carbonate of biogenic origin showing no distinct grains. Appendix 6 outlines results and characteristics of all samples considered in this study.

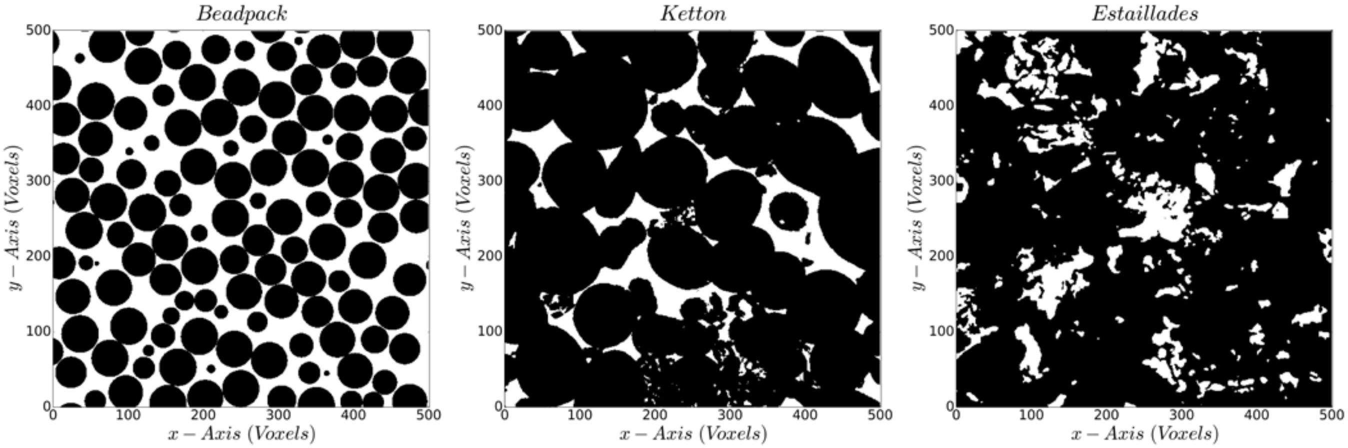

Figure 5: Three Micro-CT images of artifical and sedimentary rock used to illustrate directional measures to quantify pore morphology

Covariance Estimation

The directional covariance was estimated using an implementation of the algorithm presented by Pant (2016) (Appendix 6). The Beadpack sample shows periodicity in all three directions due to the presence of a significant hole effect. The mean grain size and specific surface area are in close agreement to the theoretical values of $r_{grain} = 100$ [μm] and $S_v = 38250$ [m^{-1}]. Ketton shows a significantly smaller characteristic pore size in the z direction with strong periodicity indicating a structural difference in the vertical and horizontal directions. By comparing the covariance of hard and non-overlapping spheres (Figure 1) with the results shown in figure 6 we find that Beadpack closely resembles the expected hard-sphere model. Ketton shows similarity to the hard-sphere model in the z-direction whereas the x and y direction are interpreted as overlapping grains. Finally, Estaillades shows no periodicity in the covariance arising due to the complex structure of the pore space.

To estimate the REV scale for these samples, the directional variations in pore space morphology must be taken into account. The size of the REV is the same in all directions for the Beadpack. For Ketton the size of the REV is direction dependent as stabilization occurs later for the z-direction. Consequently, the largest stabilization distance must be chosen as the REV scale. No stabilization can be observed in the Estaillades sample and therefore no distinct REV size can be defined.

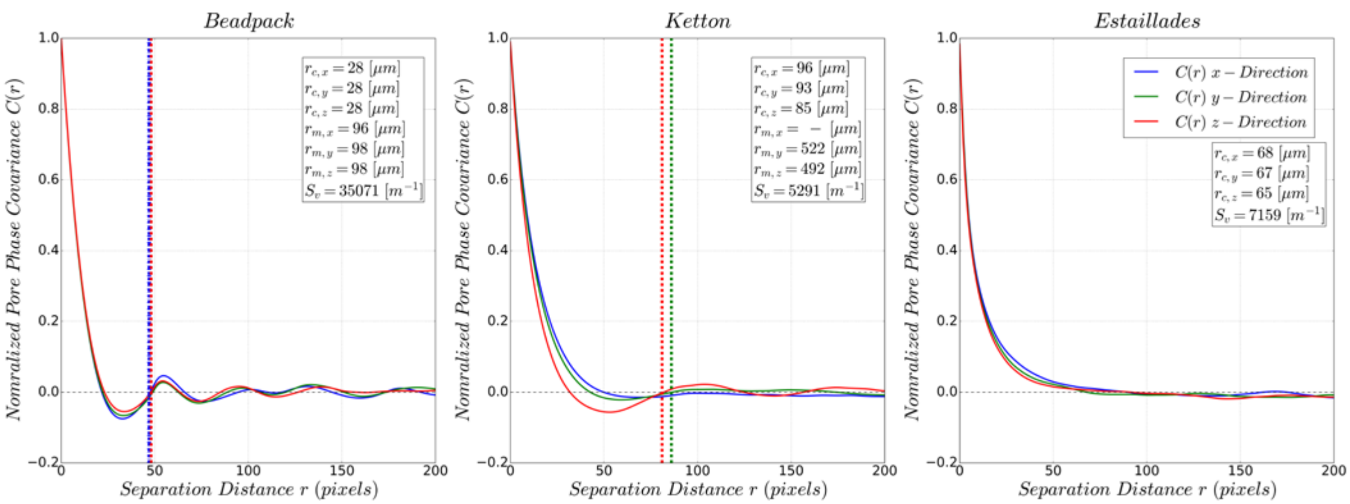

Figure 6: Estimated directional covariance for Beadpack, Ketton and Estaillades samples. Directional variations show structural differences which is supported by the analytical shape of the covariance of hard and non-overlapping spheres (Figure 1).

Minkowski Tensors as measures of pore space anisotropy

The grain pore interfaces of the analysed samples have been discretised using a marching cubes algorithm (Appendix 4). The anisotropy index $\beta_1^{0,2}$ was evaluated numerically as a function of the window size. This allows the definition of an anisotropy based REV where the shape of the graph $\beta_1^{0,2}(r)$ stabilizes and the intrinsic anisotropy of the material is reached (Figure 7).

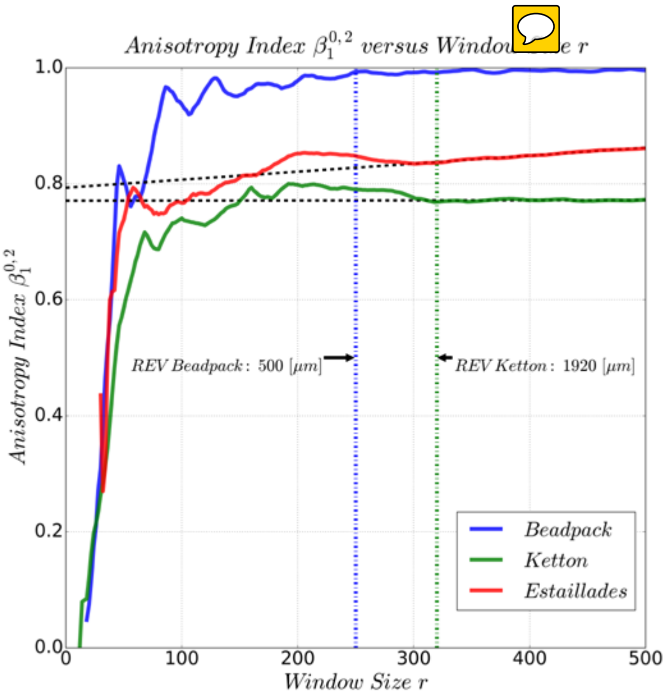

Figure 7: Comparison of the anisotropy indices for artificial and sediementary samples as a function of image size. Stabilisations indicate the REV determined from surface anisotropy.

	$\bar{W}_1^{0,2}$ [-]	$\beta_1^{0,2}$ [-]
Beadpack	$\begin{bmatrix} 0.333 & 0 & 0 \\ 0 & 0.333 & 0 \\ 0 & 0 & 0.333 \end{bmatrix}$	0.99
Estaillades	$\begin{bmatrix} 0.316 & 0 & 0 \\ 0 & 0.321 & 0 \\ 0 & 0 & 0.364 \end{bmatrix}$	0.86
Ketton	$\begin{bmatrix} 0.306 & 0 & 0 \\ 0 & 0.322 & 0 \\ 0 & 0 & 0.372 \end{bmatrix}$	0.77

Table 3: Anisotropy indices and Minkowski tensor of the full image size for the presented samples.

For the Beadpack, isotropic behaviour can be observed where $\beta_1^{0,2}$ approaches unity and an REV of approximately 500 μm can be identified. This is equivalent to five times the diameter of the individual grains (d=100 μm). Early fluctuations can be explained by the image containing individual spherical grains at 50, 80 and 120 voxels respectively.

Ketton shows a clear stabilization at 1920 μm, additionally highlighted by the horizontal dashed straight line fit. Fitting a straight line for the Estaillades samples shows that no stabilization is obtained within the image. This indicates that the REV has not been reached as the material exhibits a change in anisotropy. While a short stabilization is reached at 200 voxels it is necessary to evaluate the significance of this anisotropy by averaging over an ensemble of sub volumes at this length scale. Table 3 presents the normalised first Minkowski tensor $\bar{W}_1^{0,2}$ and the anisotropy index $\beta_1^{0,2}$ at the full images size for each sample.

From these results we were able to deduce directional trends of the pore-grain interface. The Beadpack sample shows clear isotropic behaviour and no preferential orientation. For Ketton, we can observe a preferential orientation where 40% of the interface is oriented in the z-direction. While the anisotropy index has been evaluated for Estaillades for the full image, it is not possible to define the orientation of the complex pore-grain interface as representative for an REV and may change when larger samples of the carbonate are acquired and analysed. Where distinct grains in the material can be identified such as Ketton or Beadpack, the magnitude of the anisotropy index can be interpreted as the ratio of the shortest and longest half axis of a representative grain. For Ketton the estimated anisotropy may occur due to preferential cementation of the calcite oolites leading to deformation of the individual grains.

Decomposition of the Minkowski tensor into eigenvalues and eigenvectors allows directional information of the pore grain interface as a function of the sub volume size to be obtained. Using a stereonet projection of the eigenvectors we can analyse the three dimensional vectors and their change in orientation (Figure 8). Furthermore, we have attributed the eigenvectors with their respective eigenvalues showing the directions of minimum (blue), intermediate (green) and maximum (red) eigenvalues. Increasing saturation in colours corresponds to increasing sub volume size. Coloured diamonds indicate the orientation of the eigenvectors at full image size. Isocontours indicate the 2 sigma range for the density of eigenvectors.

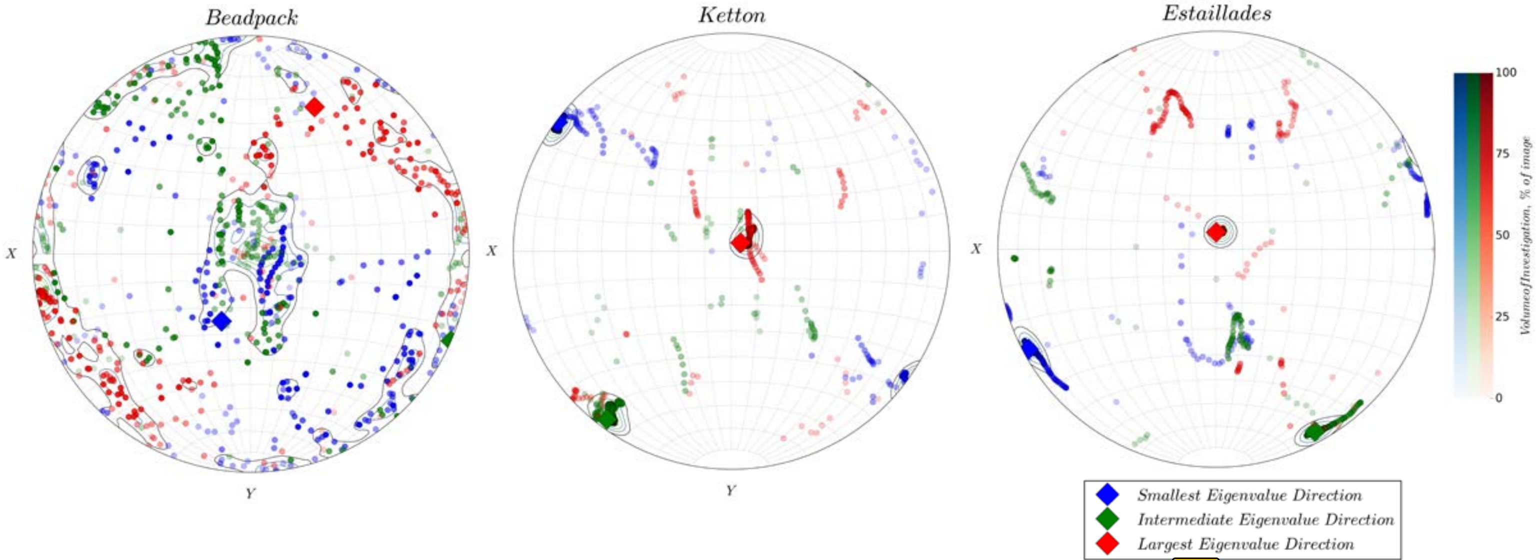

Figure 8: Stereonet projections of the eigenvectors and eigenvalues as a function of images size for three presented samples. Diamonds indicate the directions of minimum (blue), intermediate (green) and maximum (red) eigenvalues. Increased color saturation indicates larger image size.

The random dispersed pattern seen for the artificial Beadpack sample (Figure 8) arises from the isotropic nature of the Minkowski tensor for this sample. This is due to the fact that for isotropic media the eigenvalues tend towards $\frac{1}{3}$ and all orientations i.e. the eigenvectors, are equally likely to occur. Contrary to the Beadpack sample, Ketton shows a well-defined preferred orientation at small sample size (low colour saturation). This indicates that there exists one intrinsic anisotropy and orientation in the material. This trend follows our previous observation (Figure 7 middle) that there is a well-defined REV scale for the Ketton sample. Estaillades has been shown not to exhibit an REV at the full image scale which can also be observed from the directional distribution of the eigenvectors of the Minkowski tensor. We observe a wandering of the orientation across the stereonet with multiple subscales of different orientations.

To summarise our findings on evaluating the anisotropy of the material using Minkowski tensors we conclude that it is possible to define two criteria to establish an REV. To estimate the size of the REV for anisotropic samples based on the Minkowski tensor $\overline{W}_1^{0,2}$ it is necessary for stabilization of the anisotropy index to occur over a sufficient range of consecutive sample sizes. This establishes a scale and magnitude of intrinsic anisotropy in the material. For sedimentary or carbonate samples consisting of distinct grains this information can be used to infer the shape of the average grains in terms of a representative spheroid (Hörrmann et al. 2014). The second criterion can be established from the eigenvector decomposition. For materials exhibiting isotropic behaviour random scattering is expected. If the analysed material has an intrinsic preferred orientation, a dense cluster of orientations can be observed in the stereonet projection of the eigenvectors. For sedimentary samples for which no REV can be defined no stabilisation in the anisotropy index or the distribution of eigenvectors can be found.

Single-Phase Flow Properties

Prediction of single-phase permeability from directional covariance

Permeability was computed on the binary segmented representations of the acquired seventeen Micro-CT datasets using a finite difference method to solve the Stokes equation (Mostaghimi, Blunt, and Bijeljic 2013). The theory of Kozeny and Carman relates the effective permeability for isotropic media to the specific surface area S_v and the tortuosity of the pore space. We have showed in the methodology section that the directional covariance is directly related to the specific surface area (Equation 4). This implies that only the average effective permeability can be obtained from the covariance using the Kozeny-Carman relationship (Equation 11). The directional characteristic pore size $r_{c,i}$ has been correlated with the numerical directional permeability. Smaller characteristic pore radii are expected to correlate with smaller permeabilities whereas larger pore radii with higher permeabilities in the corresponding direction. Figure 9 shows a correlation matrix of the directional permeability with the characteristic pore size obtained from the directional covariance estimates. Good directional agreement for many samples can be observed including the complex Estaillades sample. Deviations from this trend can be explained by the fact that the size of the images for samples S1 and C1-2 may not be sufficient to accurately estimate the covariance.

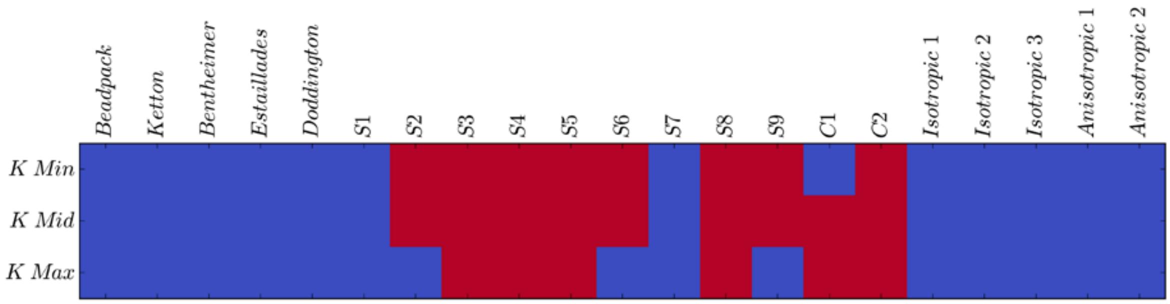

Figure 9: Qualitative comparison of the numerical permeability tensor and the characteristic pore size derived from the estimated directional covariance. Blue shading indicates a qualitative correlation. Red shadings indicate deviation from the expected relationship.

Minkowski Tensors as Qualitative indicators of directional permeability

The Kozeny-Carman equation (Equation 11) allows us to establish a qualitative link between the first Minkowski tensor and the directional permeability. As we have shown earlier the first Minkowski tensor can be interpreted as the orientational distribution of the surface area of the pore-grain interface. Due to the inverse relationship with the specific surface area, the direction of the largest eigenvalue will align with the direction of the smallest permeability and the direction of the smallest eigenvalue corresponds to the largest permeability. Figure 10 summarises the results in terms of this qualitative relationship for twenty-two samples of which five are artificial parametric models as presented in the methodology section (Appendix 3). A blue shading indicates that the eigenvalues of the first Minkowski tensor are aligned with the permeability according to the theory of Kozeny-Carman; a red shading indicates otherwise.

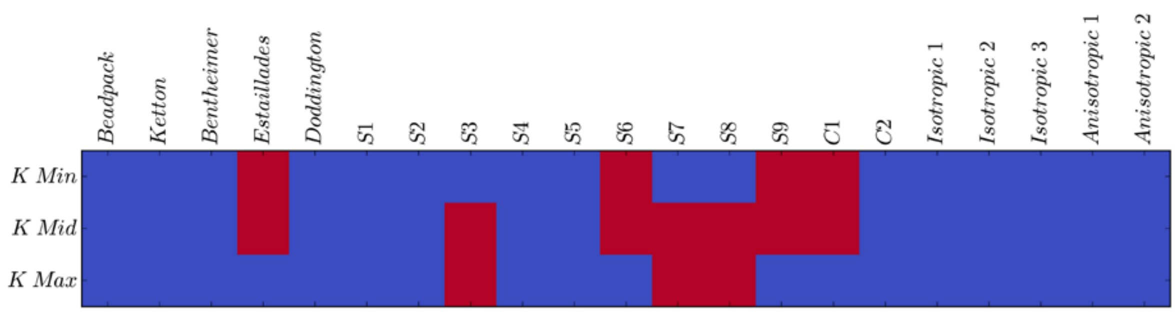

Figure 10 Qualitative comparison of the numerical permeability tensor and eigenvalues of the first Minkowski tensor. Blue shading indicates a qualitative correlation. Red shadings indicate deviation from the expected relationship.

For most of the analysed samples a good correlation between the estimated permeability and the Minkowski tensor can be observed. For all samples at least one direction, the minimum or maximum permeability is correctly predicted. The magnitude of the anisotropy index $\beta_1^{0,2}$can give an indication of the ratio of minimum and maximum directional permeability (Figure 11 right). Three samples show near isotropic behaviour where the index $\beta_1^{0,2}$ predicts a greater anisotropy.

Following the theory of (Bear and Bachmat 1986) highlighted in the methodology section, the Minkowski tensor $W_1^{0,2}$ has been used to estimate the factor α (Equation 13) that accounts for orientation information of the pore grain interface. While we have shown that the tortuosity factor T_{ij}^* is related to the Minkowski tensor $W_1^{1,1}$ we were able to estimate the tortuosity $C_\alpha \tau^2$by comparing the numerical estimate of directional permeability with the analytical results (Equation 16).

The permeability predicted using equation 16 considerably overestimates the permeability which is reflected in the high tortuosity factors (Figure 11). While for porosities greater than 20% reasonable values for $C_\alpha \tau^2$ are obtained (Mostaghimi, Blunt, and Bijeljic 2013), low porosity samples show exceedingly high tortuosity factors.

Discussion

Knowledge of an existing anisotropy in sedimentary structures can have significant impact on optimal recovery strategies for oil and gas reservoirs or the application of enhanced recovery methods. We have evaluated two methods to analyse the pore scale morphology and identify anisotropic characteristics in Micro-CT images of siliciclastic and carbonate samples.

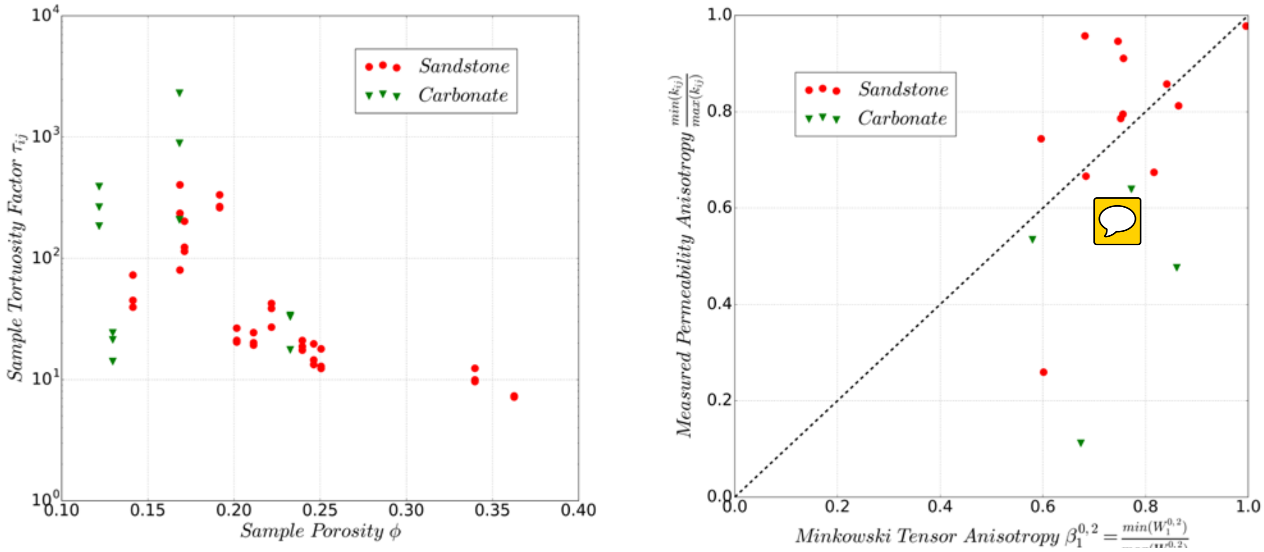

Figure 11: Left: Estimates of the tortuosity of the Micro-CT images derived from comparison of the analytical method of Bear and Bachmat with numerical estimates of the permeability tensor. Right: Comparison of the Minkowski Tensor anisotropy index and the anisotropy of the numerically estimated permeability tensor.

Evaluating the directional covariance allows qualitative evaluation of the pore space morphology (Figure 9). Local differences in pore structures can be observed where sedimentary or chemical processes have altered the pore and grain structure. This can be observed in the Ketton sample (Figure 6, 7, 8) where evidence was found of significant differences in the pore structure between horizontal and vertical directions. This is evident from the reduced characteristic pore size (Figure 6), the Minkowski tensor $W_1^{0,2}$having its largest eigenvalue in the vertical direction (Figure 7, Table 3) where the lowest value of permeability can be found. While it is not possible to attribute this directional change solely to one mechanism without further investigation, chemical processes leading to preferential cementation of the oolite grains presents a possible explanation.

More importantly the evaluation of the covariance and tensorial Minkowski measures shows that their use is effective when both methods are applied complimentary. For the majority of the samples analysed both the covariance and Minkowski tensor indicate the presence of anisotropy in the pore-grain interface (Figure 9, 10).The definition of a representative elementary volume from the covariance can be challenging and in many cases ambiguous. Stabilization of the covariance is difficult to determine and varies in different directions indicating the need to define directional REVs. Using the Minkowski tensor to determine an REV size based on intrinsic material anisotropy (Figure 7) and stabilization in the orientation distribution (Figure 8) is intuitive and considered an advantage of tensorial Minkowski measures compared to the covariance.

We have found no evidence that the magnitude of the anisotropy can be linked directly to anisotropy of the permeability tensor (Figure 11 right). We have shown that Minkowski tensors have a physical interpretation in the context of macroscopic momentum balance theory of Bear and Bachmat (1986). This allows empirical tortuosity factors for each spatial direction to be determined where numerical estimates of permeability are available. To reduce uncertainty on these results a detailed analysis incorporating theoretical results on upper and lower bounds of permeability should be performed. Incorporation of the translation covariant Minkowski Tensor $W_1^{1,1}$could lead to better estimates of the permeability from spatial statistics of the pore-grain interface and will be considered as future work.

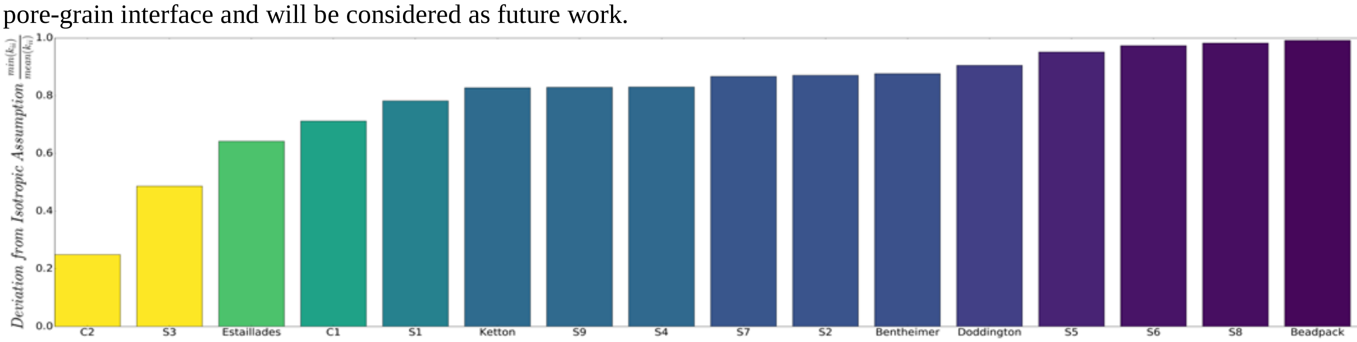

Figure 12 Comparison of the anisotropy of the permeability tensor for the evaluated sedimentary samples considered in this study. Most samples show a difference of 20% and between the smallest and largest values of permeability.

Finally, our analysis has shown that most samples of sedimentary rock show an intrinsic anisotropy of the permeability tensor (Figure 12). The impact of this anisotropy of the permeability at the pore scale must be evaluated on a case by case basis for the applications considered. Our results challenge the assumption that granular sedimentary rock e.g. ´Ketton, Doddington or Bentheimer (Appendix 6) can be considered isotropic at the pore scale and directional measures such as Minkowski measures provide effective tools to determine the presence and nature of directional variation in pore space morphology.

Conclusions

Micro-CT images of artificial and sedimentary rock have been evaluated in terms of their static and dynamic properties as a function of the direction of measurement. By applying the classic covariance or two-point probability function in three orthogonal directions we were able to identify directional differences in pore space morphology. We have applied a novel extension of scalar minkowski functionals to tensorial measures first introduced by Schröder-Turk et al. (2013). These tensors can be used to characterize the anisotropy of the pore-grain interface. By numerically estimating the anisotropy of the Minkowski tensor characterizing the orientation of the boundary surface as a function of image size we were able to determine REV length scales based on measures of surface anisotropy and preferential orientation.

By numerically estimating the permeability of the studied samples we were able to relate pore-grain interface anisotropy to single-phase directional permeability. Our results show that Minkowski measures allow a qualitative estimation of the principal directions of flow. While the covariance cannot provide an effective measure of directional permeability, characteristic pore sizes derived from directional estimates of the covariance provide a good qualitative correlation with the single-phase permeability tensor. We therefore conclude that both the covariance and Minkowski tensors are complimentary measures for the primary directions of flow and can be used to evaluate the existence of anisotropy without the need to perform computationally expensive measurements of the permeability tensor.

By showing the relationship of Minkowski tensors to the macroscopic momentum balance approach of Bear and Bachmat (1986) we highlight the physical interpretation and importance of this new class of integral geometric relations. Comparison of the estimated permeability with finite-difference measurements of permeability show that it is not sufficient to include surface orientation effects alone but characterization of the tortuosity is necessary and considered as future work.

As Mecke and Arns (2005) have shown, the application of Minkowski functionals to the field of fluids in porous media is rich for the case of scalar measures. Future work will focus on extending these approaches to incorporate directional information in the form of measured Minkowski tensors in new material models. Characterisation of foams for enhanced oil recovery methods or changes in the grain sizes and shapes due to chemical dissolution processes could be quantified using Minkowski vectors and tensors. Empirical measurements of these integral geometric properties could provide effective new constraints for image reconstruction and modeling of the pore-space morphology found in Micro-CT images of sedimentary rock.

Nomenclature

$\boldsymbol{r}$………………..Radial position vector
$P(\cdot)$…………..Probability function
Ξ………………..Pore-phase
o………………..Origin of coordinate system
$\mathbb{R}^d$……………..Set of real valued numbers of dimension-d
$C(r)$………...…Covariance
$C(r,\theta,\phi)$ …...…Directional covariance
$G(r,\theta',\phi')$……Surface orientation function (Gokhale, Tewari, and Garmestani 2005)
$|\cdot|$……………..Absolute value
S_v……………….Specific surface area
$\bar{\boldsymbol{r}}_c$. …………….. Characteristic pore size
K………………..Geometric body
∂K…………..…Boundary/surface of body K
$W_v^{r,s}(K)$………Minkowski functional (r,s) of order ν
G_v…………..........v=1,2: $G_v = 1$, v=3: $G_v = mean\ curvature$
$W_1^{0,0}(K)$ ………Surface Area of Body K
$W_1^{0,2}(K)$………First translation invariant tensorial Minkowski functional
$\bar{W}_1^{0,2}(K)$………Normalized first translation invariant tensorial Minkowski functional
$\beta_1^{0,2}$……………Normalized first translation invariant tensorial Minkowski functional
$\#(\cdot)$ …………Count function, number of elements in set
k_{eff}…………....Effective permeability
k_{ij}……………...Permeability tensor
α_{ij}……………...Surface orientation tensor
δ_{ij}……………...Dirac delta function
$S_{\alpha\beta}$……………Pore-grain boundary surface
ϕ……………….Porosity
C_α……………..Kozeny-Carman geometric factor
T_{ij}^*……………...Tortuosity factor
$\boldsymbol{x}$………………..Position vector
$W_1^{1,1}(K)$………Translation covariant tensorial Minkowski functional
τ………………..Tortuosity

References

Bear, J, and Y Bachmat. 1986. “Macroscopic Modelling of Transport Phenomena in Porous Media. 2: Applications to Mass, Momentum and Energy Transport.” *Transport in Porous Media* 1: 241–69. doi:10.1007/BF00238182.

Bear, Jacob, and Y. Bachmat. 1990. *Introduction to Modeling of Transport Phenomena in Porous Media*. Springer Netherlands. doi:10.1007/978-94-009-1926-6.

Berryman, James G. 1987. “Relationship between Specific Surface Area and Spatial Correlation Functions for Anisotropic Porous Media.” *Journal of Mathematical Physics* 28 (1): 244. doi:10.1063/1.527804.

Bijeljic, Branko. 2015. “Imperial College Micro-CT Database.” https://www.imperial.ac.uk/engineering/departments/earth-science/research/research-groups/perm/research/pore-scale-modelling/micro-ct-images-and-networks/.

Carman, P C. 1937. “Fluid Flow through Granular Beds.” *Transactions-Institution of Chemical Engineeres* 15. Institution of Chemical Engineers: 150–66. doi:Doi 10.1016/S0263-8762(97)80003-2.

Carman, P. C. 1939. “Permeability of Saturated Sands, Soils and Clays.” *The Journal of Agricultural Science* 29: 262. doi:10.1017/S0021859600051789.

Chapuis, Robert P., and Michel. Aubertin. 2003. “Predicting the Coefficient Permeability of Soils Using the Kozeny-Carman Équation.” *École Polytechnique de Montréal*, no. January: 1–31.

Childress, Stephen. 1972. “Viscous Flow Past a Random Array of Spheres.” *The Journal of Chemical Physics* 56 (6): 2527. doi:10.1063/1.1677576.

Chiu, Sung Nok, Dietrich Stoyan, Wilfrid S Kendall, and Joseph Mecke. 2013. *Stochastic Geometry and Its Applications*. John Wiley & Sons.

Clausius, R. 1858. “Über Die Bewegende Kraft Der Wärme, Teil I, Teil II.”

D’Arcy, H. P. G. 1856. “Les Fontaines Publiques de Ill. Ville de Dijon.” *Victor Dalmont*.

Debye, P., H. R. Anderson, and H. Brumberger. 1957. “Scattering by an Inhomogeneous Solid. II. the Correlation Function and Its Application.” *Journal of Applied Physics* 28 (6): 679–83. doi:10.1063/1.1722830.

Dong, Hu, and Martin J. Blunt. 2009. “Pore-Network Extraction from Micro-Computerized-Tomography Images.” *Physical Review E - Statistical, Nonlinear, and Soft Matter Physics* 80 (3): 1–11. doi:10.1103/PhysRevE.80.036307.

Gokhale, A. M., A. Tewari, and H. Garmestani. 2005. “Constraints on Microstructural Two-Point Correlation Functions.” *Scripta Materialia* 53 (8): 989–93. doi:10.1016/j.scriptamat.2005.06.013.

Guimer, A. N. D. R. E., Gérard Fournet. 1955. “Small Angle Scattering of X-Rays.” *J. Wiley & Sons, New York*.

Guo, Peijun. 2012. “Dependency of Tortuosity and Permeability of Porous Media on Directional Distribution of Pore Voids.” *Transport in Porous Media* 95 (2): 285–303. doi:10.1007/s11242-012-0043-8.

———. 2015. “Lower and Upper Bounds for Hydraulic Tortuosity of Porous Materials.” *Transport in Porous Media* 109 (3). Springer Netherlands: 659–71. doi:10.1007/s11242-015-0541-6.

Hadwiger, H. 1957. “Vorlesungen Über Inhalt, Oberfläche Und Isoperimetrie.” *Springer*.

Hörrmann, Julia, Daniel Hug, Michael Andreas Klatt, and Klaus Mecke. 2014. “Minkowski Tensor Density Formulas for Boolean Models.” *Advances in Applied Mathematics* 55 (1): 48–85. doi:10.1016/j.aam.2014.01.001.

Hörrmann, Julia, and Wolfgang Weil. 2015. “Valuations and Boolean Models,” 1–34. http://arxiv.org/abs/1510.07910.

Howells, I.D. 1974. “Drag due to the Motion of a Newtonian Fluid through a Sparse Random Array of Small Fixed Rigid Objects.” *J. Fluid Mech.* 64: 449–75.

Jacod, J., and P. Joathon. 1972. “Conditional Simulation of Sedimentary Cycles in Three Dimensions.” In *Mathematical Models of Sedimentary Processes*, pp 139–65. doi:10.1007/978-1-4684-1995-5_7.

Jin, C., P. A. Langston, G. E. Pavlovskaya, M. R. Hall, and S. P. Rigby. 2016. “Statistics of Highly Heterogeneous Flow Fields Confined to Three-Dimensional Random Porous Media.” *Physical Review E - Statistical, Nonlinear, and Soft Matter Physics* 93 (1). doi:10.1103/PhysRevE.93.013122.

Kozeny, Josef. 1927. “Über Kapillare Leitung Des Wassers Im Boden.” *Akad. Wiss.Wien* 136: 271–306.

Kuhn, Matthew R., Wai Ching Sun, and Qi Wang. 2015. “Stress-Induced Anisotropy in Granular Materials: Fabric, Stiffness, and Permeability.” *Acta Geotechnica* 10 (4). Springer Berlin Heidelberg: 399–419. doi:10.1007/s11440-015-0397-5.

Matheron, George. 1967. “Éléments Pour Une Théorie Des Milieux Poreux.”

———. 1975. *Random Sets and Integral Geometry. Wiley Series in Probability and Mathematical Statistics: Probability and Mathematical Statistics*.

Mecke, K R, T Buchert, and H Wagner. 1994. “Robust Morphological Measures for Large-Scale Structure in the Universe.” *Astronomy and Astrophysics 288* 288: 697–704. doi:10.1017/CBO9781107415324.004.

Mecke, Klaus, and C H Arns. 2005. “Fluids in Porous Media: A Morphometric Approach.” *Journal of Physics: Condensed Matter* 17 (9): S503–34. doi:10.1088/0953-8984/17/9/014.

Mostaghimi, Peyman, Martin J. Blunt, and Branko Bijeljic. 2013. “Computations of Absolute Permeability on Micro-CT Images.” *Mathematical Geosciences* 45 (1): 103–25. doi:10.1007/s11004-012-9431-4.

Pan, C X, M Hilpert, and C T Miller. 2004. “Lattice-{B}oltzmann Simulation of Two-Phase Flow in Porous Media.” *Water Resources Research* 40 (2): W01501. doi:10.1029/2003WR002120.

Pan, Chongxun, Markus Hilpert, and Cass Miller. 2001. “Pore-Scale Modeling of Saturated Permeabilities in Random Sphere Packings.” *Phys. Rev. E* 64 (6): 1–9. doi:10.1103/PhysRevE.64.066702.

Pant, Lalit. 2016. “Stochastic Characterization and Reconstruction of Porous Media.” http://www.esdlab.mece.ualberta.ca/pdfs/Lalit_phdthesis.pdf.

Pietruszczak, S., and S. Krucinski. 1989. “Description of Anisotropic Response of Clays Using a Tensorial Measure of Structural Disorder.” *Mechanics of Materials .2-3 (* 8: 237–49.

Prager, Stephen. 1961. “Viscous Flow through Porous Media.” *Physics of Fluids* 4 (12): 1477. doi:10.1063/1.1706246.

Rubinstein, Jacob, and S. Torquato. 1989. “Flow in Random Porous Media: Mathematical Formulation, Variational Principles, and Rigorous Bounds.” *Journal of Fluid Mechanics* 206 (1889): 25. doi:10.1017/S0022112089002211.

Saadatfar, M., M. Mukherjee, M. Madadi, G. E. Schr??der-Turk, F. Garcia-Moreno, F. M. Schaller, S. Hutzler, A. P. Sheppard, J. Banhart, and U. Ramamurty. 2012. "Structure and Deformation Correlation of Closed-Cell Aluminium Foam Subject to Uniaxial Compression." *Acta Materialia* 60 (8): 3604–15. doi:10.1016/j.actamat.2012.02.029.

Schröder-Turk, G. E., S. Kapfer, B. Breidenbach, C. Beisbart, and K. Mecke. 2010. "Tensorial Minkowski Functionals and Anisotropy Measures for Planar Patterns." *Journal of Microscopy* 238 (1): 57–74. doi:10.1111/j.1365-2818.2009.03331.x.

Schröder-Turk, G. E., W. Mickel, S. C. Kapfer, F. M. Schaller, B. Breidenbach, D. Hug, and K. Mecke. 2013. "Minkowski Tensors of Anisotropic Spatial Structure." *New Journal of Physics* 15. doi:10.1088/1367-2630/15/8/083028.

Serra, J. 1982. *Image Analysis and Mathematical Morphology*. Academic Press, London.

———. 1987. "Boolean Random Functions." *Acta Stereol.* 6: 325–30.

Smith, P., and S. Torquato. 1988. "Computer Simulation Results for the Two-Point Probability Function of Composite Media." *Journal of Computational Physics* 76 (1): 176–91. doi:10.1016/0021-9991(88)90136-2.

Stoyan, S., Kendall, W. S., Mecke, J. 1995. *Stochastic Geometry and Its Applications*. doi:10.1002/bimj.4710390510.

Torquato, S. 1997. "Exact Expression for the Effective Elastic Tensor of Disordered Composites." *Physical Review Letters* 79 (4): 681–84. doi:10.1103/PhysRevLett.79.681.

Torquato, S. 2002. "Random Heterogeneous Materials." *Springer Verlag-New York*. doi:10.1007/978-1-4757-6355-3.

Torquato, Salvatore, and G Stell. 1985. "Microstucture of Two-Pahse Random Media." *J. Chem. Phys* 82 (2).

Wetzel, E. D., and C. L. Tucker. 1999. "Area Tensors for Modeling Microstructure during Laminar Liquid-Liquid Mixing." *International Journal of Multiphase Flow* 25 (1): 35–61. doi:10.1016/S0301-9322(98)00013-5.

Appendices

Appendix 1A: Milestones

Journal/DOI	Year	Title	Authors	Contribution
	1856	Les Fontaines Publiques de Ill. Ville de Dijon.	H.P.G. D'Arcy	First experiments on the hydraulic conductivity of porous soils.
Akad. Wiss.Wien, 136	1927	Über kapillare Leitung des Wassers im Boden	J. Kozeny	Derived an analytical relationship for the permeability for spherical beadpacks
10.1016/S0263-8762(97)80003-2	1937	Fluid flow through granular beds	Carman	Extensive compendium of experimental and theoretical work to estimate permeability from material properties.
10.1063/1.1722830	1957	Scattering by an inhomogeneous solid. II. the correlation function and its application	Debye	Theoretical and analytical relationship between two-point probability functions and effective material properties.
Springer Berlin	1957	Vorlesungen über Inhalt, Oberfläche und Isoperimetrie	H. Hadwiger	Formulated a (proven) theorem about the morphological requirements to describe geometrical bodies. Minkowski functionals are a direct result of this theorem.
10.1007/BF00238182	1986	Macroscopic modelling of transport phenomena in porous media. 2: Applications to mass, momentum and energy transport	J. Bear and Y. Bachmat	Derived an analytical equation for the permeability at the REV scale by applying a macroscopic momentum balance approach.
10.1063/1.527804	1987	Relationship between specific surface area and spatial correlation functions for anisotropic porous media	J.G. Berryman	Derived an equation for the surface area derived from the covariance of an anisotropic material. Allows effective permeability to be derived using the Kozeny-Carman equation.
10.1017/S0022112089002211	1989	Flow in random porous media: mathematical formulation, variational principles, and rigorous bounds	Rubinstein and Torquato	Derive analytical bounds for the effective permeability of a random porous medium. This relationship contains a characteristic length scale which can be estimated from an empirical correlation function.
10.1016/S0301-9322(98)00013-5	1999	Area tensors for modeling microstructure during laminar liquid-liquid mixing	Wetzel and Tucker	Analytical derivation of the equations governing the mixing of two fluids without interfacial tension. Define surface orientation tensor equivalent to the first translation invariant Minkowski tensor.
10.1103/PhysRevE.64.066702	2001	Pore-scale modeling of saturated permeabilities in random sphere packings	C. Pan, M. Hilpert, C. Miller	Describe a lattice Boltzmann method to compute the permeability of a material from Micro-CT images.
10.1007/978-1-4757-6355-3	2002	Random Heterogeneous Materials	S. Torquato	Collection of theoretical approaches to model random materials by statistical or empirical methods. Provides classification framework for problems in random materials. Solutions and theoretical bounds for numerous applications.
10.1088/0953-8984/17/9/014	2005	Fluids in porous media: a morphometric approach	K. Mecke and C.H. Arns	Introduced concept of scalar Minkowski functionals in the context of fluids in porous media. Comparison of various modeling approaches and incorporation of Minkowski functionals in physical constitutive laws.
10.1088/1367-2630/15/8/083028	2013	Minkowski tensors of anisotropic spatial structure	Schröder-Turk, G. E.Mickel, W. Kapfer, S. C.et al.	Extended the theory on scalar Minkowski functionals to vectorial and tensorial measures derived from Hadwigers theorem. Provide numerical algorithms to compute Minkowski tensors on arbitrary surfaces and provide numerous applications
10.1007/s11004-012-9431-4	2013	Computations of Absolute Permeability on Micro-CT Images Peyman	P. Mostaghimi, M.J. Blunt, B. Bijeljic	Developed finite-difference implementation of Stokes equations with accurate boundary conditions for permeability estimation of binary Micro-CT images. Evaluated validity of Kozeny Carman equation at the pore scale and length scales for REVs.

Appendix 1B: Summaries of key milestone publications

Akad. Wiss.Wien 136: 271–306
Year: 1927

Title: Über Kapillare Leitung Des Wassers Im Boden

Author(s): Kozeny, Josef

Contribution:
Established the first mathematical description relating an applied pressure gradient to observed flow rates.
Derived an equation for the permeability of a bundle of tubes with equal diameter under steady laminar flow conditions. This equation relates the specific surface area of a material and its porosity to the observed permeability. Many of the later contributions to estimate permeability from material properties are based on the work of Kozeny and later Carman who evaluated the validity of Kozenys method with new experimental data. In its original form Kozeny gives a relation for the permeability of a spherical beadpack as:

$$k = c\frac{l_s}{l_w}\frac{\phi^3}{36(1-\phi)^2}d_w^2$$

Here the factor $\frac{l_s}{l_w}$ describes the tortuosity of the pore space.

Methodology:
Based on previous experiments evaluating the relationship between applied pressure gradients, observed flow rates, grain size and sorting in each material a simple relationship to estimate the single-phase permeability of materials under steady laminar flow is established. Kozeny derived analytical relationships for special cases such as spherical beadpacks and compared the validity of his theory by comparison with published data.

Conclusion:
The work of Kozeny is considered as one of the earliest milestones in the theory of flow in porous media. His analytical model to compute permeability based on intrinsic material properties has influenced many later works trying to improve or disprove the validity of the Kozeny-(Carman) equation for various flow regimes and materials. His mathematical derivations and analytical approach introduced new concepts such as the tortuosity derived from physical observations.

Comments:
The manuscript is in German and easy to follow along. Many experimental results are provided as well as references provided to a large number of resources from the time of Kozeny. His work gives insight into a rich community of theoretical and experimental work performed in the field of flow on porous media. An English translation of the manuscript is not available but would be a valuable contribution.

Journal of Applied Physics 28 (6): 679–83. doi:10.1063/1.1722830.
Year: 1957

Title: Scattering by an Inhomogeneous Solid. II. The Correlation Function and Its Application *

Author(s): Debye, P., H. R. Anderson, and H. Brumberger

Contribution:
The authors establish a theoretical relationship between the experimental results of small angle x-ray scattering of porous media and the theory of two-point probability functions also known as the covariance. They show that for porous media that have a random distribution of pore diameters the two-point probability function has an exponential form and can be observed experimentally in their results. Their analysis shows that it is possible to estimate the specific surface area from the initial slope of the covariance. Their contribution is based on earlier work by Debye and Bueche (1949) who first developed a method to analyse materials by small angle scattering of x-ray radiation.

Methodology

Based on classical theory on scattering they show that the two-point correlation function is related to the intensity of scattered radiation:

$$i = 4\pi \langle \eta \rangle_{av} V \int \gamma(r) r^2 \frac{\sin(ks\boldsymbol{r})}{ks\boldsymbol{r}} d\boldsymbol{r}$$

Where $\gamma(r)$ is the empirical covariance of an analysed sample. Following mathematical derivation showed that the specific surface area S_v is related to the covariance by:

$$S_v = \frac{S}{V} = -4\phi(1-\phi) \frac{d\gamma(r)}{dr}_{|r=0}$$

By comparing their theoretical with the experimental results they are able to evaluate material properties for a number of samples and show the validity of their work. They refer to the work of Guinier and Fournet (1955) as well as Porod (1952) who have derived the same analytical results using a different approach. The experimental study of (Van Nordstand and Johnson 1954) used a purely empirical approach to define a relation between the specific surface area and two-point probability functions.

Conclusion:
The theoretical work of Debye, Anderson and Brumberger is one of the first references that highlights the ability to derive material properties from two-point correlation functions. As such their work presents the basis for later analytical and experimental work in the field of random porous media and have influenced new interest in the field of spatial probability functions allowing for a full statistical model of random porous media in the context of n-point probability functions.

Comments:
A short and precise paper that gives most mathematical derivation steps as well as experimental results. Attributing Guinier et. Al. to have obtained similar results prior to Debye and nearly at the same time from a similar approach is humbling in the context of modern scientific literature. Unknowing at the time, their results are not only valid for isotropic media but also anisotropic as is later shown by Berryman (1987).

Journal of Mathematical Physics 28 (1): 244. doi:10.1063/1.527804.
Year: 1987

Title: Relationship between Specific Surface Area and Spatial Correlation Functions for Anisotropic Porous Media

Author(s): Berryman, James G.

Contribution:
In the context of anisotropic porous media, the work of Berryman provides a mathematical foundation to apply the covariance as a measure of the pore scale morphology and material properties. He showed that the specific surface area of an anisotropic random porous medium can be derived from a radially averaged covariance. Therefore, estimates of the specific surface area of an anisotropic porous medium can be derived from empirical covariance functions and used in conjunction with the Kozeny-Carman equation that relates the specific surface area of a porous medium to predict the effective average single-phase permeability.

Methodology
For anisotropic media Berryman recognized that the two-point probability function exhibits a translation invariance property i.e. the result is independent on the location of measurement. This allowed him to evaluate the two-point probability function for a binary porous medium solely as a function of orientation. The resulting expression for the specific surface area is equivalent to the result derived by Debye, Anderson, and Brumberger (1957).

Conclusion:
The results of Berrryman show that estimates of the specific surface area may be obtained from measurements of the covariance function for isotropic and anisotropic media. While one could assume that this is possible a mathematical proof for this is necessary. His work also highlights the versatility of the covariance function in the context of estimating material properties and its applicability to random materials.

Comments:
A short but valuable contribution towards characterizing anisotropic random media.

Mathematical Geosciences 45 (1): 103–25. doi:10.1007/s11004-012-9431-4.
Year: 2013

Title: Computations of Absolute Permeability on Micro-CT Images

Author(s): Mostaghimi, Peyman, Martin J. Blunt, Branko Bijeljic

Contribution:
The authors present a novel finite-difference implementation with exact no-flow boundary conditions at the pore-grain interface to solve the Stokes equation directly on binary segmented Micro-CT images. The proposed method has been validated against lattice Boltzmann methods. Permeability of sandpacks, sandstone and carbonate samples is computed with respect to three cartesian directions to analyse the anisotropy of permeability at the pore scale. Their results show that the REV at the pore scale may vary significantly compared to static properties such as porosity or the specific surface area as well as permeability. The authors show that the Kozeny-Carman equation significantly over predicts the permeability of sedimentary samples at the pore scale.

Methodology:
The authors develop a new finite-difference scheme to solve the Stokes equation on binary images. Their method decouples pressure and velocity in a Semi-Implicit formulation. By including a correction term for pressure and velocity they are able to establish convergence. Their convergence criterion evaluates the flux across voxelized elements. The sparse system of linear equations is solved iteratively using an algebraic multigrid solver. By applying a known pressure gradient and evaluating the flux they are able to numerically estimate the permeability of binary images.

Conclusion:
Using the method developed to compute numerical estimates of permeability on binary Micro-CT images, the authors show that the Kozeny-Carman equation fails to predict the permeability of many samples of natural sandstones and carbonates. Significant correction factors have to be introduced to account for the deviation from observed values of permeability. By evaluating the porosity, specific surface area across a range of sample sizes they are able to establish REV scales for a number of samples. Their results show that the REV scale varies significantly when derived from static or dynamic flow properties.

Comments:
Extraction of the largest connected pore space may not be representative of the permeability of a Micro-CT sample. A method to find all connected components should be applied to find all contributing sub volumes prior to solving the relevant equations.

New Journal of Physics 15. doi: 10.1088/1367-2630/15/8/083028
Year: 2010

Title: Minkowski Tensors of Anisotropic Spatial Structure

Author(s): Schröder-Turk, Gerd E, Walter Mickel, Sebastian C Kapfer, Fabian M Schaller, Boris Breidenbach, Daniel Hug, Klaus Mecke

Contribution:
The authors extend the classical framework of scalar Minkowski functionals, volume, surface area, integral of mean curvature and the euler characteristic to tensorial functionals. They provide a rigorous mathematical framework from which many integral geometric tensor properties can be derived. The developed theory of vectorial and tensorial Minkowski functionals is accompanied by discretized equations that allow the integrals to be solved for arbitrary surfaces. By providing a number of examples where Minkowski tensors have been applied to characterize anisotropy they highlight the potential of this method to characterize the structure of materials.

Methodology:
Based on the more general forms of Hadwiger (1957) they extend the framework of scalar Minkowski functionals to Minkowski vectors and tensors. By introducing a general notation valid for all Minkowski functionals. This notation stems for the general integral geometric relation from which all other Minkowski functionals can be derived:

$$W_v^{r,s}(K) = \frac{1}{3}\int_{\partial K} G_v x^r n^s dA\,, v\ =\ 1, 2, 3\ and\ (r, s)\ =\ (2, 0), (1, 1)\ or\ (0, 2)$$

The above relationship is valid only for the given set of exponents and is zero otherwise. The function G_v has following form:

$$G_v = \begin{cases} 1, & for\ v = 0 \\ 1, & for\ v = 1 \\ \dfrac{\kappa_1 + \kappa_2}{2}, & for\ v = 2 \end{cases}$$

These tensors can be categorized into two classes: translation covariant i.e. their measurement depends on a reference location (often an area or volume centroid is chosen) and translation invariant tensors. For closed surfaces or discrete bodies, the translation covariant tensors are well defined and may be used extract shape information.

Conclusion:
While Schröder et al have not discovered a whole new class of image morphological descriptors, they have provided a mathematical framework that links many integral geometric relationships that occur in physical processes. This allows these properties to be reevaluated and where 2D or 3D images of the structures are available to be used to characterize structural elements of materials and their distribution.

Comments:
The theory surrounding Minkowski tensors is rich and there are many applications that could be considered. Especially the large variety of translation covariant Minkowski tensors could be useful to describe physical or chemical processes in porous media where closed bodies occur e.g. the formation of droplets in capillary trapping or shapes of foams in enhanced oil recovery processes. Their integration into a new class of property models could allow incorporation of orientational information in improved material models.

Transactions-Institution of Chemical Engineeres 15. Institution of Chemical Engineers: 150–66. Doi: 10.1016/S0263-8762(97)80003-2.
Year: 1937

Title: Fluid Flow through Granular Beds

Author(s): Carman, P C.

Contribution:
Carmans publication presents the most detailed and complete resource of experimental and theoretical results for the estimation of permeability in granular media in his time. Starting with the initial experiments of D'Arcy he compiles an extensive set of data and conclusions from before and after Kozenys seminal work. Other approaches are highlighted where dimensionless groups provide good results in predicting the permeability of beds of spherical grains.

Methodology
This publication is an extensive comparative literature review encompassing a large variety of experimental and theoretical results on the estimation of permeability. Each approach is carefully examined and evaluated with respect to other published results highlighting the importance of each presented publication.

Conclusion:
An invaluable compendium of analytical and theoretical results on permeability estimation.

Comments:
Many of the results presented stem from publications written in English. While Kozenys publication is written in German there exists a large variety of results that have gone unnoticed in this context and are not mentioned in the work of Carman.

Journal of Physics: Condensed Matter 17 (9): S503–34. doi:10.1088/0953-8984/17/9/014.
Year: 2005

Title: Fluids in Porous Media: A Morphometric Approach

Author(s): Mecke, Klaus, and C H Arns

Contribution:
The authors present a morphological approach to characterize properties of porous media and their contained fluids. They first introduce the theory of scalar Minkowski functionals in the context of material properties. They highlight the important link between integral geometric relationships and the surface and volume integrals that occur in the mathematical description of processes in porous media.

Methodology
The authors first introduce the general concept of Minkowski functionals. The scalar Minkowski functionals in three dimensions are the volume, surface area, integral of mean curvature and euler characteristic. These are derived from Hadwigers Theorem which states that the global morphology of a binary material can be described by the set of scalar Minkowski measures. This allows the formulation of material models for effective or average properties using the set of scalar Minkowski functionals to be defined.
Modeling approaches such as the Boolean model are introduced and used to generate realizations of Micro-CT images based on measured scalar Minkowski functionals. By evaluating two-point probability functions for each model they estimate a goodness of fit for each of the proposed modeling approaches.

Conclusion:
The authors conclude that a combination of Minkowski measures and two-point probability functions allow for the most realistic visual reproduction of porous media but leave work on future hybrid models as an open problem. Their model for the shear modulus of vuggy carbonates is a promising result in the context of geological applications. Their derivation of capillary condensation is an inspiring approach to link morphological measures to physical processes and highlights their importance in the context of single and multi-phase flow in porous media.

Comments:
While Hadwigers theorem states that material morphology can be uniquely described on a global scale, this is not the case for the local scale as models that are conditioned with respect to the global scalar minkowski functionals often show very different morphology while having similar effective properties.

I believe this publication is underrated and maybe undiscovered in its importance. There are many valuable approaches defined here that deserve to be carefully reexamined in the context of modern geomodelling approaches and open problems in the multi-phase flow behavior in porous media and enhanced oil recovery methods.

Transport in Porous Media 1: 241–69. doi:10.1007/BF00238182.
Year: 1986

Title: Macroscopic Modelling of Transport Phenomena in Porous Media. 2: Applications to Mass, Momentum and Energy Transport.

Author(s): Bear, J, Y Bachmat.

Contribution:

In their first publication the authors describe a volume averaging approach to define the equations of flow and transport in porous media. This requires the definition of a so called representative elementary volume over which the equations can be solved. They provide a rigorous mathematical derivation of the equations governing the transport of mass, exchange of momentum and energy. This allows them in their second volume to apply their general theory to a set of relevant applications. These include heat conduction, thermo-elastic as well as diffusion problems. The authors derive a general equation for single phase flow in porous media that allows an estimate of the permeability tensor of a material to be obtained.

$$k_{ij} = \frac{\phi^3}{C_\alpha S_v^2} \alpha_{il}^{-1} T_{lj}^* = \frac{\phi^3}{C_\alpha S_v^2} \alpha_{ij}^{-1} \frac{1}{\tau^2}$$

Methodology:
By applying a macroscopic momentum balance to a representative elementary volume over which the equations governing single-phase flow are averaged, the authors derive a general expression of the permeability of a porous medium. This equation includes two factors that characterize the orientation and tortuosity of the pore space.

$$\alpha_{ij} = \delta_{ij} - \frac{1}{S_{\alpha\beta}} \int n_\alpha^i \, n_\alpha^j dA$$
$$T_{ij}^* = \frac{1}{\phi V} \int x^i n^j dA$$

As has been shown in the methodology section, these integral geometric measures are directly related to tensorial Minkowski functionals. For simplified cases of isotropic media these equations simplify to the well-known Kozeny-Carman equation.

Conclusion:
The authors presented a new analytical expression to predict the permeability from derived material properties. While their method contains two integral geometric expressions to characterize the pore-grain interface and the tortuosity at the REV scale the authors give no indication on how these properties could be measured. With the advent of modern Micro-CT methods measurement of these integral geometric relations for actual pore grain surfaces has become possible and is evaluated as part of this thesis.

Comments:
Mathematically complex and convoluted, could easily be split into multiple publications. Their general theory provides many relevant examples and approaches to solving complex physical processes in porous media.

Appendix 2: Workflow Description

The following section describes the general workflow used to generate parametric models, compute covariance and minkowski tensors from binary representations as well as the computation of directional permeability of the individual samples.

We can distinguish two sources of data in this thesis: parametric models and Micro-CT images of sedimentary or artificial rock. Parametric models were created using a NURBS (Non-Uniform-Rational-B-Spline) based modeling tool Rhino and a parametric modeling suite Grasshopper. The workflow used for parametric modeling can be found in appendix 3.

The VTK toolkit was used to extract triangulated surfaces from Micro-CT samples of sedimentary rock and to create binary representations of the parametric models. Triangulated surface representations were used as input for the Karambola software that allows computation of scalar, vectorial and tensorial Minkowski functionals and is presented by (Schröder-Turk et al. 2013) (Appendix 4). By using the virtualization toolkit Docker, numerous virtual machines were used to parallelize the computation of Minkowski valuations on a cluster of desktop pcs. The programming language python was used to compute covariance from binary representations (Pant 2016). An OpenFoam implementation of the algorithms described by (Mostaghimi, Blunt, and Bijeljic 2013) has been applied to compute numerical estimates of the permeability in three spatial directions. All data was analysed and graphs created using jupyter notebooks. All algorithms and datasets were made publicly available (Appendix 5).

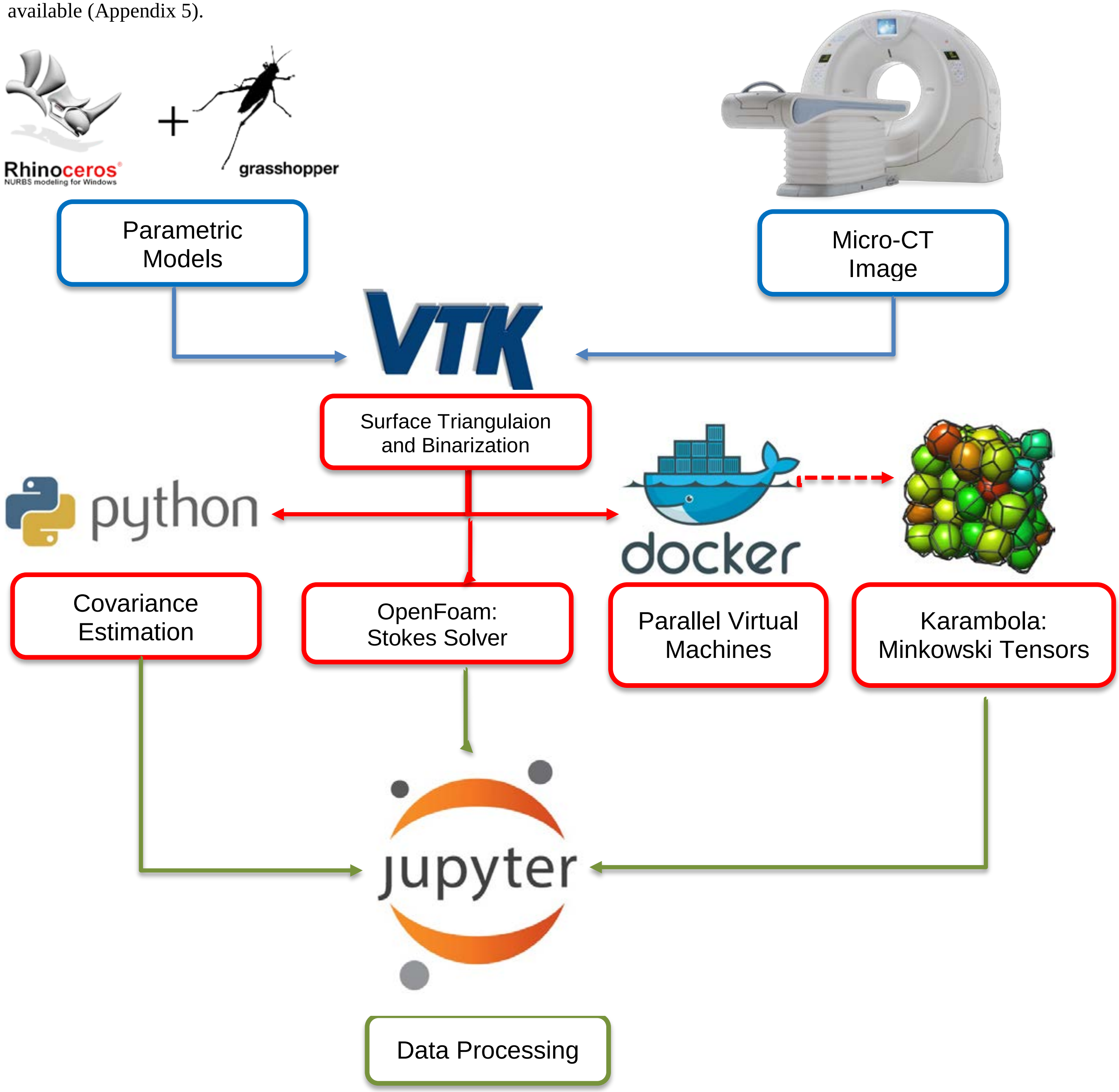

Appendix Figure 1: Data generation and processing workflow used to estimate covariance and Minkowski tensors from Micro-CT data.

Appendix 3: Parametric Pore Space Modeling

Analysing the behaviour of statistical and image morphological measures for various rock samples is a challenging task as the geometry of the existing pore space often arises from physical and chemical processes. These can often be related to stochastic processes such as the Boolean models (S. Torquato 2002). Due to the stochastic nature of the models, analysis of the statistical measures requires evaluation using an ensemble of realizations. While this approach gives a better understanding of the average behaviour of the evaluated measures, a deterministic modelling approach combined with evaluation on a known parameter space can give insight into fundamental behaviour of individual models.

Here we describe a set of parametric models based on a deterministic equally spaced soft sphere and later ellipsoidal grain model. The parametric modelling tool Grasshopper was used to create parametric models arising from a set of linked modules. This allows an intuitive and modular workflow for model generation and parametrization. All models were created using Rhino 5.0 and the Grasshopper module.

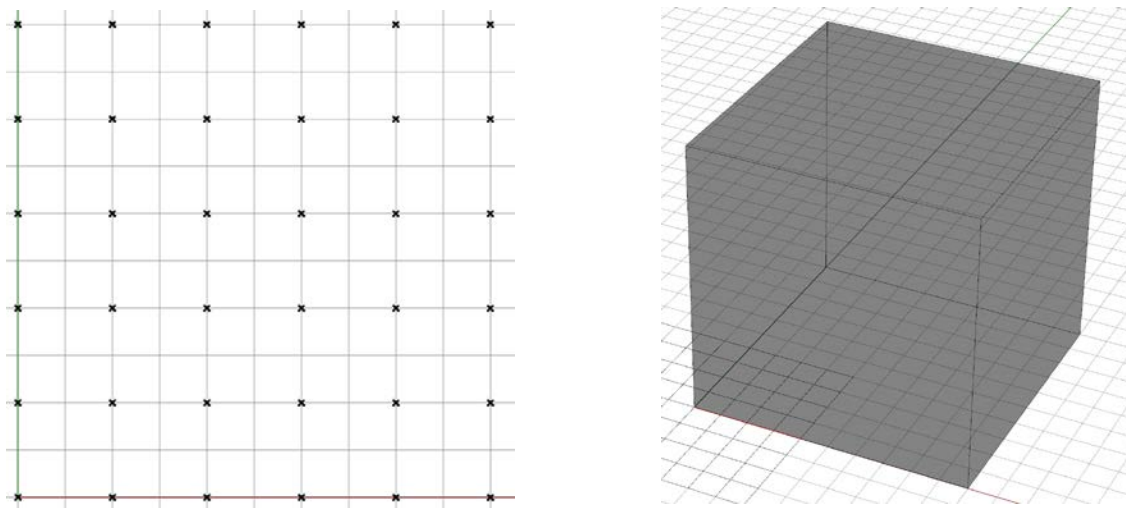

Appendix Figure 2: Left: Input grid of points representing the centroids of the ellipsoidal or spherical grains. Right: Box volume from which the pore spaced is extracted using Boolean operations.

Each model is comprised of a grid of points equally spaced on a 3D lattice. These equally spaced lattice points act as centers for spherical or ellipsoidal grains. Each grain is defined by a center vertex and a radius. Ellipsoidal grains are created by applying a uniaxial or biaxial scaling transformation. Each sphere is represented as a NURBS (Non-Uniform Rational B-Spline) object and represents a single grain. The number of grains in each direction can be varied independently. For this study an equal number of grains were placed to create a cubic grid of spheres with equal edge lengths. This allows a similar representation as the available images of sedimentary rock samples and eliminates the need to compensate for bias due to unequal grid sizes in each direction.

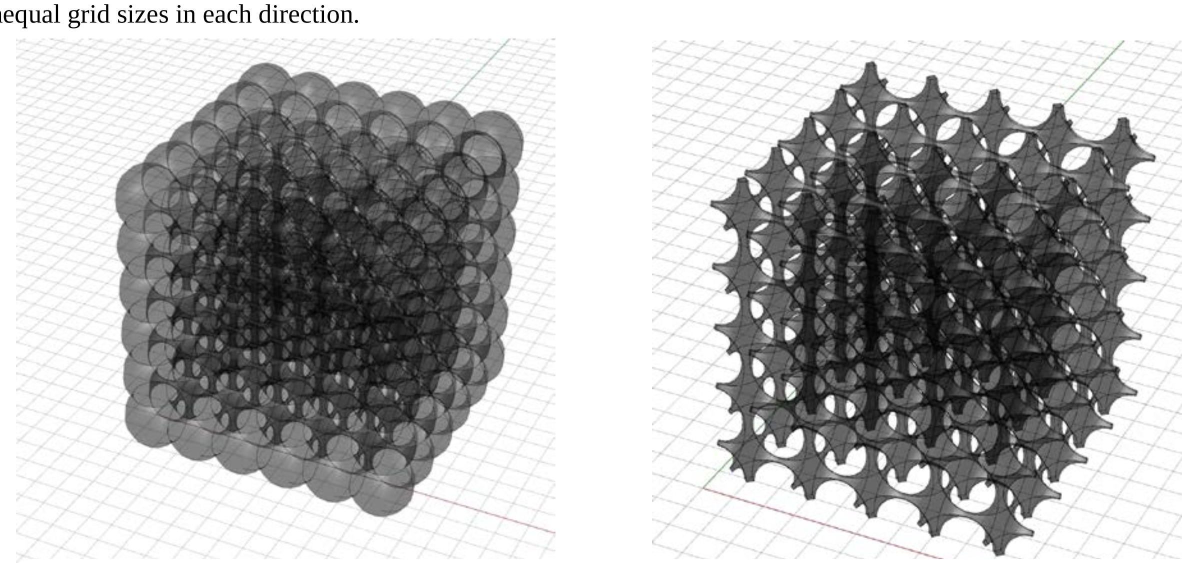

Appendix Figure 3: Left: Union of sphere srepresenting the grains of a parametric sample. Right: Pore grain interface after applying Boolean operations to extract the boundary surface.

To create a surface representation of the pore space, a number of a number of Boolean operations are applied. Due to overlap of the soft spheres a union of all grains allows the grain space to be represented. A surrounding box volume is introduced to represent the present void space. Boolean subtraction of the grains from the void space results in a representation of the intergranular void space. Finally, Boolean intersection of the void space and the bounding surfaces results in a surface representation of the boundary surfaces of the grain and void space. These surfaces are open and periodic in the Cartesian directions closely mimicking the behaviour of perfect isotropic arrangements of spherical grains. This parametric representation is similar to triply periodic media such as Schwartz's P surface.

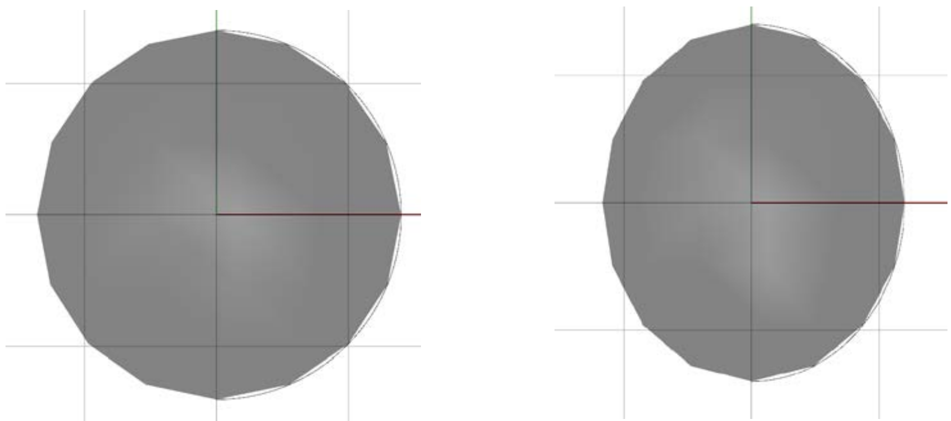

Appendix Figure 4: Left representative spheroid grain with radius 1.4 [m]. Right: Ellipsoidal grain with reduced radius of 1.2 in the x-y plane. (x-z plane shown)

A number of deterministic scenarios were created to evaluate statistical as well as image morphological characteristics and relate these to their respective flow properties. Isotropic models were created with radii ranging from 1.2 to 1.4 [m]. These lengths are later scaled to match the typical size of Micro-CT samples. To evaluate the effect of anisotropy two models have been created with ellipsoidal grains. The ellipsoidal grains have been stretched in two of three directions leading to anisotropic behaviour in z-direction, with the x-y plane showing equal behavior (Appendix 6).

Minkowski properties of these parametric models can be directly measured on the triangulated surface representation by export via a suitable file format. Models were first exported to STL mesh files and later converted to the POLY file format required by the Minkowski tensor library Karambola (Schröder-Turk et al. 2013). To evaluate the covariance of these parametric models an intermediate binarization step was required. To convert a surface representation to a binary voxel image the Visual Tool Kit was used. The VTK library consists of industry standard algorithms for computations on large image datasets and surface representations as they are commonly applied in environments where CT imaging is applied, such as bioengineering or medical applications.

To convert the STL surface representations the vtk algorithm vtkPolyDataToImageStencil and vtkImageStencil were applied. To convert open surfaces, it is necessary to first apply a hole closing on all open edges before converting to binary format. This removes introduced artifacts in the images and allows a highly resolved representation of the surfaces. To reintroduce periodic boundaries single voxel slices in each Cartesian direction were removed that have been added as a padding by the binarization algorithm. All images were specified to have 500 voxels in each direction matching the dimensions of the available image samples of sedimentary rock. All binary images were output as TIFF image stacks for later processing and evaluation. For computation of permeability each binary representation was converted to a raw 8-bit format with a voxel resolution of 2 μm. While this resolution has no physical context it is in the range of the resolution of typical Micro-CT images and allows for later comparison of permeability estimates in typical mD or Darcy units. A full analysis of covariance, Minkowski measures and permeability is presented in appendix 6.

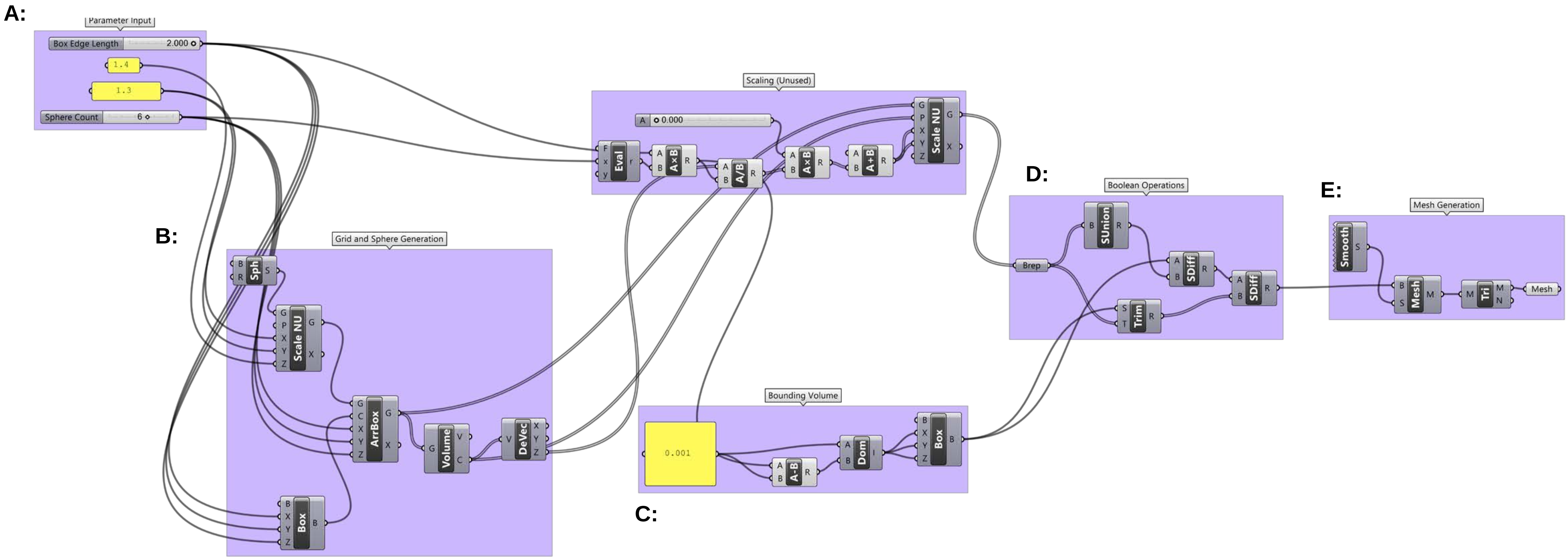

Appendix Figure 5: A: Input parameters used to construct the parametric model. Two radii can be input, here 1.4 denotes the radius in the z-direction and 1.3 the radius in the x-y plane. Sphere count determines how many spheres are placed in each direction to create the array of spheroids. B: Modules creating the grid of spheres from the input array. C: Box volume generation modules from which the pore-grain interface is extracted. D: Boolean operations acting on the box volume and set of spheres. E: Mesh triangulation of the pore-grain interface and output to file.

Appendix 4: Interface extraction from binary Micro-CT Images

While Minkowski Tensors are well defined on parametric surfaces where analytical results for scalar and tensorial Minkowski functionals exist (Schröder-Turk et al. 2013; Hörrmann and Weil 2015), approximations of the Minkowski tensors for arbitrary surfaces can be computed from discretized surface representations.

The surface integrals in the definition of the first and second translation invariant Minkowski tensor are discretized as a sum over finite surface elements (Equation 8). A triangulated surface representation is necessary as an input for the available implementation in the Minkowski functional software library Karambola (Schröder-Turk et al. 2013). The classical Marching Cubes algorithm was used to extract an explicit triangulated surface representation of the boundary between grain and void space. Two approaches to extract the boundary surfaces were evaluated:

The first approach assumes that the image has not been segmented using image segmentation methods and is available as a grayscale image. As no raw data was available in this study, a 3-dimensional Gaussian filter with a standard deviation of σ=1.0 was applied to the segmented images, before applying the Otsu thresholding method to convert the image to a binary representation. For this approach it is key that binary images are required to later compute statistical measures such as covariance as well as the permeability. Therefor the image after thresholding using Otsu's method should be used for all later computations. It is important to note that this would be the standard procedure in analysing Minkowski tensors or any statistical or numerical measure on the binary and surface representations.

The second approach assumes that the image has been filtered and segmented into binary form as has been the case for the available Micro-CT images. The boundary surface is extracted from the binary voxel representation using a discrete Marching Cubes algorithm. This approach allows an almost exact representation of the given binary surface. All results presented in this thesis apart from the following comparison have been computed using the discrete Marching Cubes method.

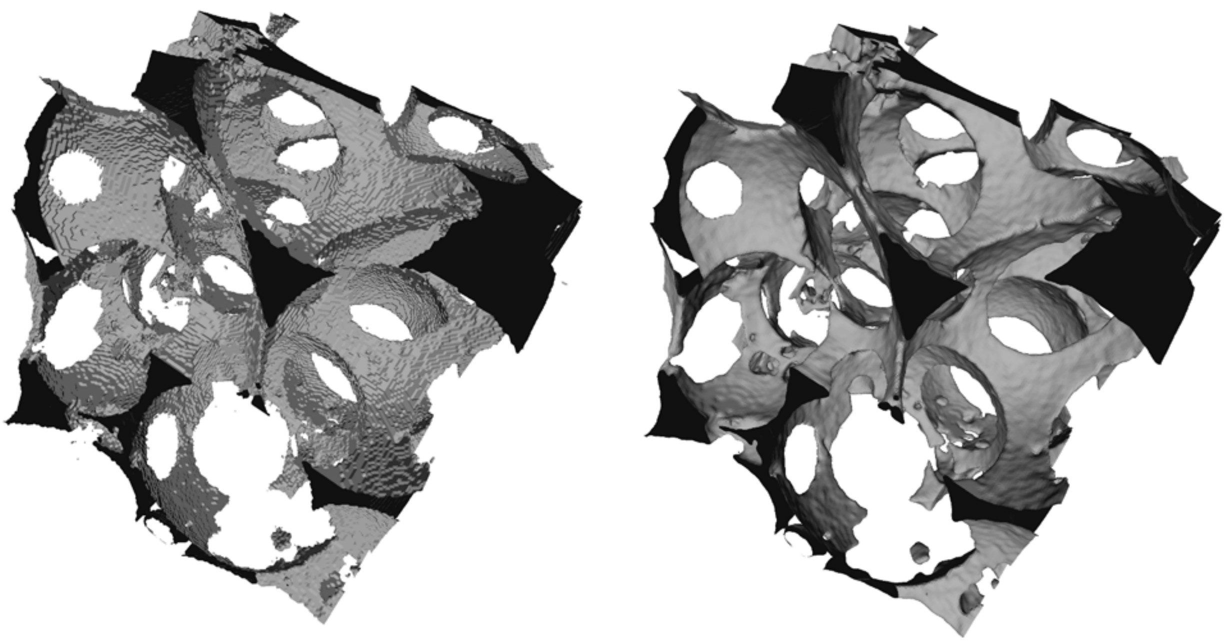

Appendix Figure 6: Comparison of two surface triangulations of the Ketton sample. Left: The surface has been directly extracted from the input dataset and shows a rough surface topology. Right: Smoothed sample after application of a Gaussian blur and thresholding using Otsu method.

A first general observation can be made on the smoothness of the resulting meshes (Appendix Figure 6). The surfaces extracted after applying Otsu's method are very smooth and have few edges. The discrete Marching Cubes algorithm leads to much rougher surfaces but a more exact representation compared to the binary image.

For the resulting anisotropy indices $\beta_1^{0,2}$ we can see for the Beadpack sample (Appendix Figure 7) both approaches lead to almost the same graph. For the second anisotropy index $\beta_2^{0,2}$we observe considerable mesh dependency. For smoothed meshes this measure may be used to gain insight on the curvature distribution of the pore-grain interface. For this study only the first anisotropy index was considered to have a consistent representation of the boundary across the workflow. The mesh dependency is expected as the application of the Gaussian filter changes the shape and therefore surface representation of the pore space. We therefore recommended to apply the Minkowski tensor analysis after segmentation of the binary image and if necessary evaluate the variability of the Minkowski measures as a function of smoothing applied to the resulting triangulated interface.

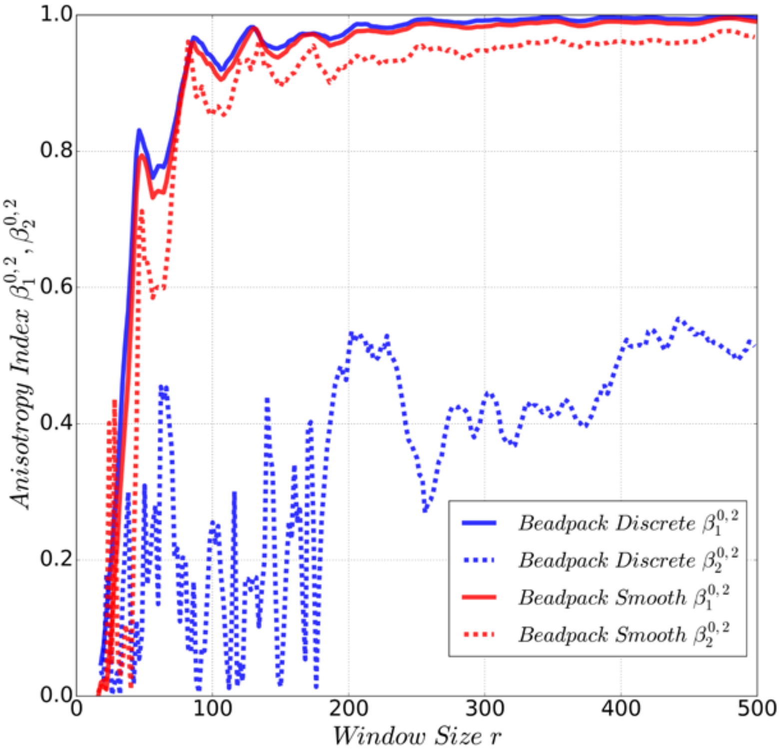

Appendix Figure 7: Comparison of the two anisotropy indices $\beta_1^{0,2}$ and $\beta_2^{0,2}$ for smooth and rough triangulations of the pore-grain interface. Considerable mesh dependency can be observed for the second anisotropy index.

Both methods, discrete and smooth, were implemented using the python wrapper library of the Visual Tool Kit VTK which provides industry standard algorithms for surface extraction from binary voxel images. Specifically, vtkDiscreteMarchingCubes and vtkMarchingCubes were used to compute the triangulated surfaces. An important issue when dealing with any discretized surface or volume representation such as triangular or tetrahedral meshes is mesh quality. The computation of Minkowski tensors on triangular meshes is not sensitive to the shape or of the triangular elements as opposed to e.g. finite element computations. Meshes that have non-mannifold vertices cannot be used for the computation of the Minkowski functionals. A comparison of various libraries showed that triangular meshes created with VTK consistently show no non-mannifold vertices. This was a critical step in this study due to the large number of meshes required (~250 per graph), any necessary manual corrections would have not made this possible.

An additional factor that has to be considered is the need for improved software allowing the computation of Minkowski tensors on very large meshes. Each mesh extracted at full image size requires 1.5 gigabyte of hard disk space. Evaluating the anisotropy indices for a range of values requires multiple hundred gigabyte of disk space which could be reduced considerably using modern storage and compression algorithms

Appendix 5: Reproducibility and Software Documentation

Reproducibility of results is an important aspect of the scientific process. Reproduction of critical results by third parties allows validation of proposed methods and workflows. Therefore, emphasis was placed on making the results and methods used in this thesis reproducible and publicly available. Due to restrictions on formatting, the thesis itself is not reproducible but all figures showing numerical results can be reproduced using the provided jupyter notebooks. All input data and computed results are freely available and may be used with proper citation of this publication. Software, results and figures have been added to the versioning system Github and are available under the following link: https://github.com/LukasMosser/MSc_Thesis

Appendix 6: Sample Results and Analysis

Sample 1: Beadpack

Orthogonal Image Projections:

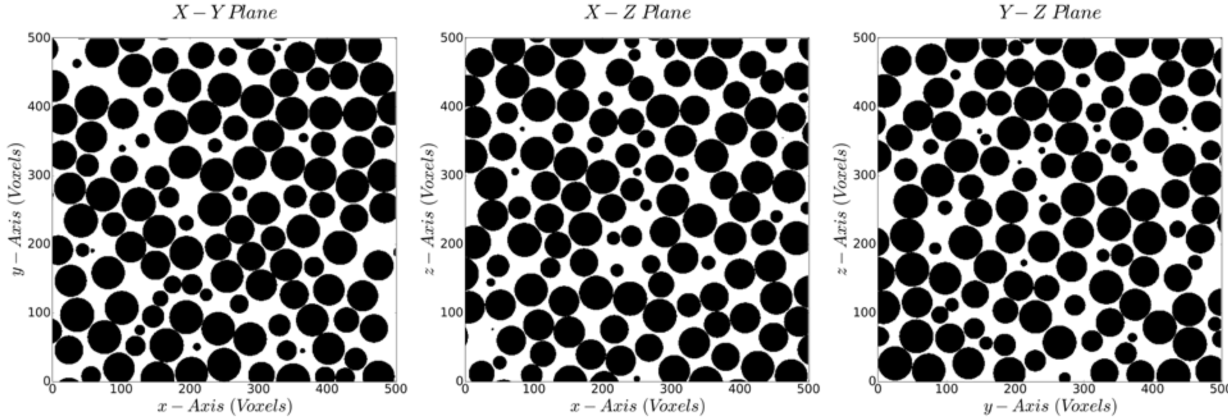

Appendix Figure 8 Orthogonal views of Beadpack Image. Views seen from front of sample.

Sample Description:

Aenean at tortor luctus purus euismod aliquet at eu metus. Pellentesque tempor ac libero laoreet ullamcorper. Suspendisse blandit ante id orci iaculis vestibulum id quis lorem. Morbi fermentum iaculis ipsum ut congue. Phasellus bibendum ornare diam, sed tempus lacus pharetra et. Aenean quis laoreet urna, interdum dictum tellus. Mauris congue suscipit tortor et commodo.

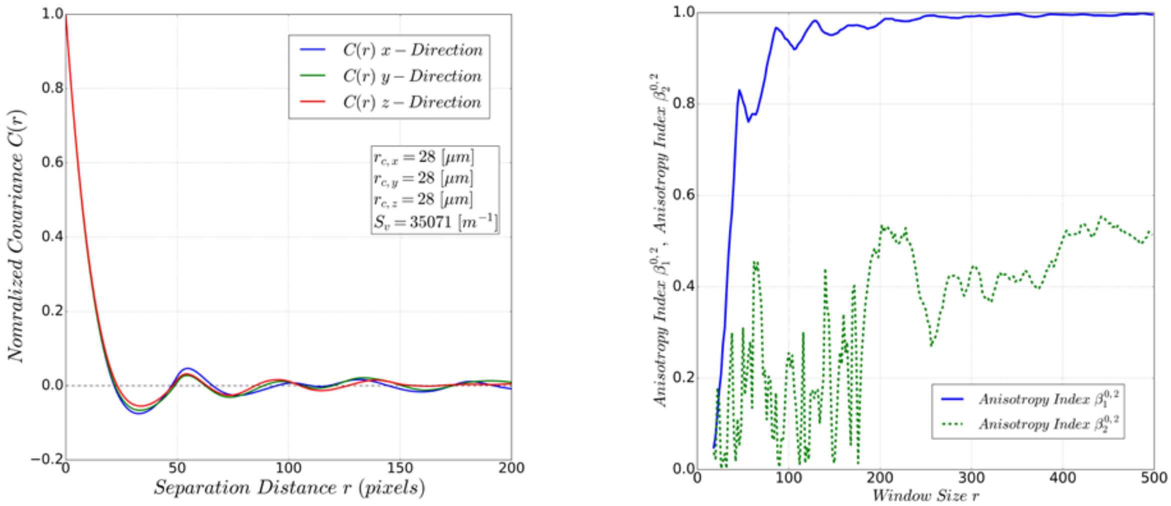

Appendix Figure 9:Left: Anisotropy indices derived from Minkowski tensor functionals. Right: Normalized directional Covariance of the Beadpack sample.

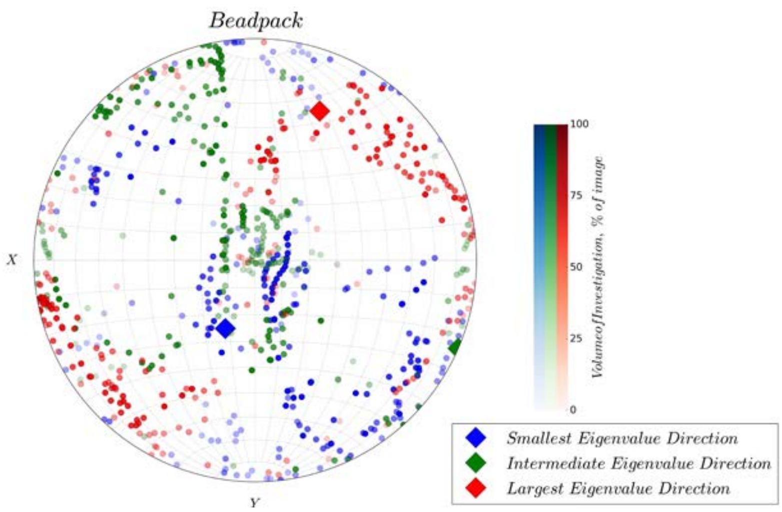

Appendix Figure 10: Stereonet projection of eigenvectors of Minkowski tensor $W_1^{0,2}$ of the Beadpack sample.

Results Summary		
Image Name	**Beadpack**	
Rock Type	**Artificial**	
Property	**Value**	**Unit**
Image Resolution	2.0	$[\boldsymbol{\mu m}]$
Image Dimensions	(500, 500, 500)	(Nx, Ny, Nz) [voxel]
Covariance Analysis Results		
Porosity	0.36	[-]
Directional Characterstic Pore Size $[\boldsymbol{r_{c,x}}, \boldsymbol{r_{c,y}}, \boldsymbol{r_{c,z}}]$	28,28,28	$[\boldsymbol{\mu m}]$
Average Characteristic Pore Size $\boldsymbol{\bar{r}_c}$	28	$[\boldsymbol{\mu m}]$
Specific Surface Area	35071	$[\boldsymbol{m^{-1}}]$
Minkowski Tensor Analysis		
Normalised Minkowski Functional $\boldsymbol{\widehat{W}_1^{0,2}}$	$\begin{bmatrix} \mathbf{0.333} & \mathbf{0} & \mathbf{0} \\ \mathbf{0} & \mathbf{0.334} & \mathbf{0} \\ \mathbf{0} & \mathbf{0} & \mathbf{0.332} \end{bmatrix}$	[-]
Normalised Minkowski Functional $\boldsymbol{\widehat{W}_2^{0,2}}$	$\begin{bmatrix} \mathbf{0.394} & \mathbf{-0.07} & \mathbf{0.02} \\ \mathbf{-0.07} & \mathbf{0.254} & \mathbf{0.009} \\ \mathbf{0.02} & \mathbf{0.009} & \mathbf{0.350} \end{bmatrix}$	[-]
Anisotropy Index $\boldsymbol{\beta_1^{0,2}}$	0.99	[-]
Anisotropy Index $\boldsymbol{\beta_2^{0,2}}$	0.51	[-]
Permeability Computation Results		
Effective Porosity	0.36	[-]
Directional Permeability	$\begin{bmatrix} \mathbf{6.184} & - & - \\ - & \mathbf{6.326} & - \\ - & - & \mathbf{6.197} \end{bmatrix}$	$[\boldsymbol{D}]$

Sample 2: Ketton

Orthogonal Image Projections:

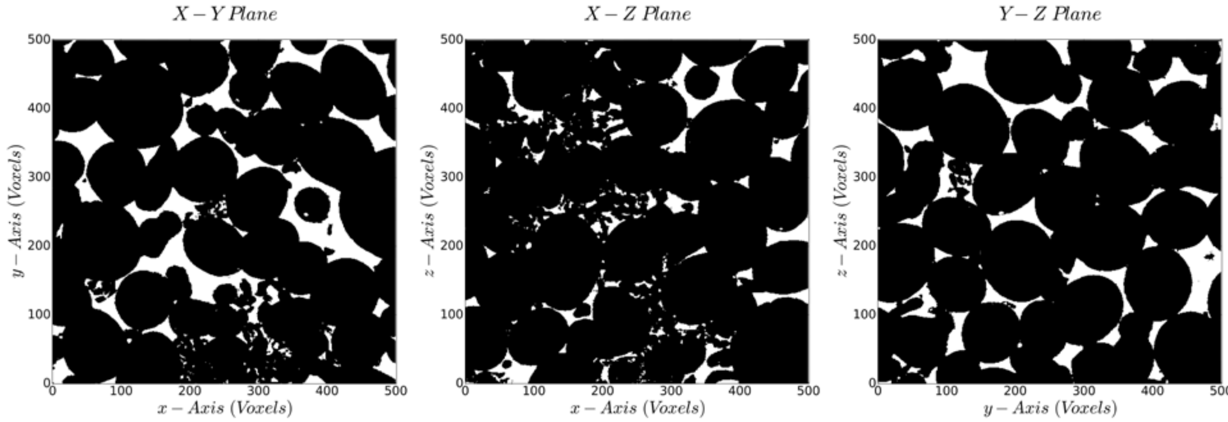

Appendix Figure 11 Orthogonal views of Ketton Image. Views seen from front of sample.

Sample Description:

Aenean at tortor luctus purus euismod aliquet at eu metus. Pellentesque tempor ac libero laoreet ullamcorper. Suspendisse blandit ante id orci iaculis vestibulum id quis lorem. Morbi fermentum iaculis ipsum ut congue. Phasellus bibendum ornare diam, sed tempus lacus pharetra et. Aenean quis laoreet urna, interdum dictum tellus. Mauris congue suscipit tortor et commodo.

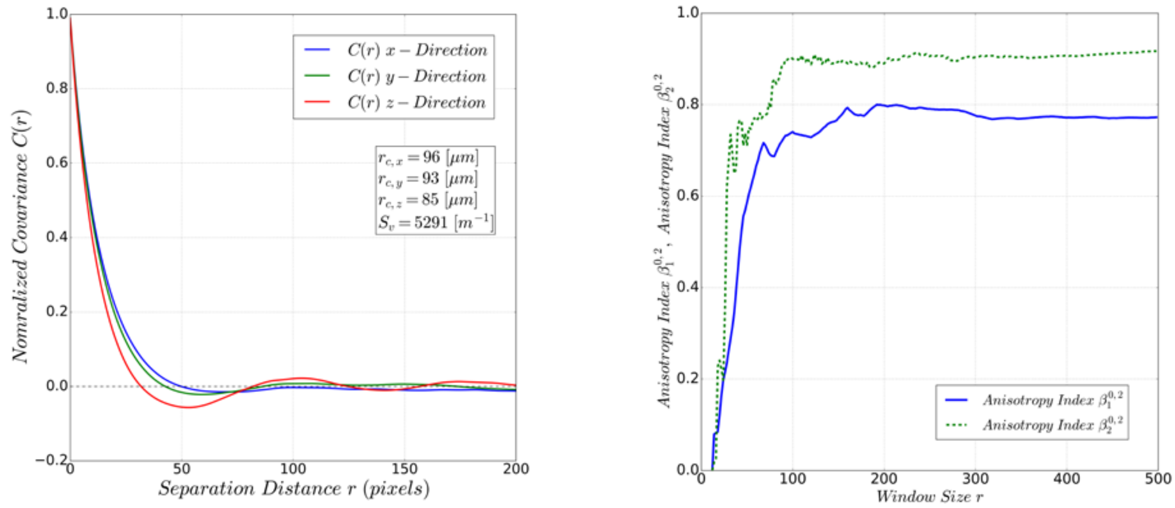

Appendix Figure 12:Left: Anisotropy indices derived from Minkowski tensor functionals. Right: Normalized directional Covariance of the Ketton sample.

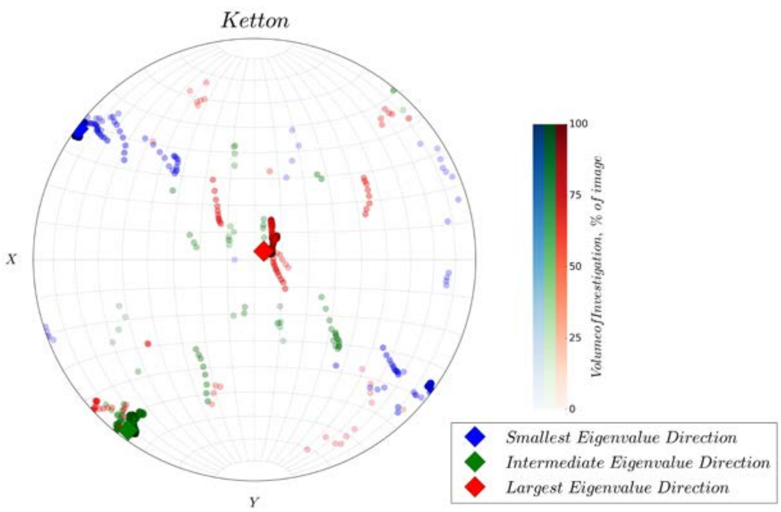

Appendix Figure 13: Stereonet projection of eigenvectors of Minkowski tensor $W_1^{0,2}$ of the Ketton sample.

Results Summary		
Image Name	**Ketton**	
Rock Type	**Carbonate**	
Property	**Value**	**Unit**
Image Resolution	6.00012	$[\boldsymbol{\mu m}]$
Image Dimensions	(500, 500, 500)	(Nx, Ny, Nz) [voxel]
Covariance Analysis Results		
Porosity	0.13	[-]
Directional Characterstic Pore Size $[\boldsymbol{r_{c,x}}, \boldsymbol{r_{c,y}}, \boldsymbol{r_{c,z}}]$	96,93,85	$[\boldsymbol{\mu m}]$
Average Characteristic Pore Size $\bar{\boldsymbol{r}}_{\boldsymbol{c}}$	85	$[\boldsymbol{\mu m}]$
Specific Surface Area	5291	$[\boldsymbol{m^{-1}}]$
Minkowski Tensor Analysis		
Normalised Minkowski Functional $\widehat{\boldsymbol{W}}_{\boldsymbol{1}}^{\boldsymbol{0,2}}$	$\begin{bmatrix} 0.306 & 0.025 & -0.003 \\ 0.025 & 0.334 & 0.004 \\ -0.003 & 0.004 & 0.331 \end{bmatrix}$	[-]
Normalised Minkowski Functional $\widehat{\boldsymbol{W}}_{\boldsymbol{2}}^{\boldsymbol{0,2}}$	$\begin{bmatrix} 0.322 & 0.005 & 0 \\ 0.005 & 0.330 & 0 \\ 0 & 0 & 0.348 \end{bmatrix}$	[-]
Anisotropy Index $\boldsymbol{\beta_1^{0,2}}$	0.77	[-]
Anisotropy Index $\boldsymbol{\beta_2^{0,2}}$	0.92	[-]
Permeability Computation Results		
Effective Porosity	0.13	[-]
Directional Permeability	$\begin{bmatrix} 5.103 & - & - \\ - & 3.456 & - \\ - & - & 3.261 \end{bmatrix}$	$[\boldsymbol{D}]$

Sample 3: Estaillades

Orthogonal Image Projections:

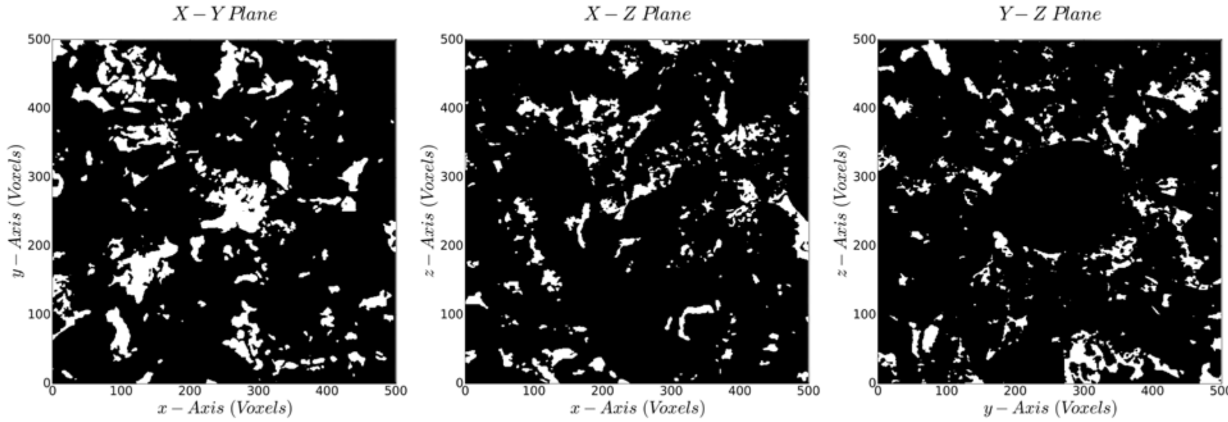

Appendix Figure 14 Orthogonal views of Estaillades Image. Views seen from front of sample.

Sample Description:
Aenean at tortor luctus purus euismod aliquet at eu metus. Pellentesque tempor ac libero laoreet ullamcorper. Suspendisse blandit ante id orci iaculis vestibulum id quis lorem. Morbi fermentum iaculis ipsum ut congue. Phasellus bibendum ornare diam, sed tempus lacus pharetra et. Aenean quis laoreet urna, interdum dictum tellus. Mauris congue suscipit tortor et commodo.

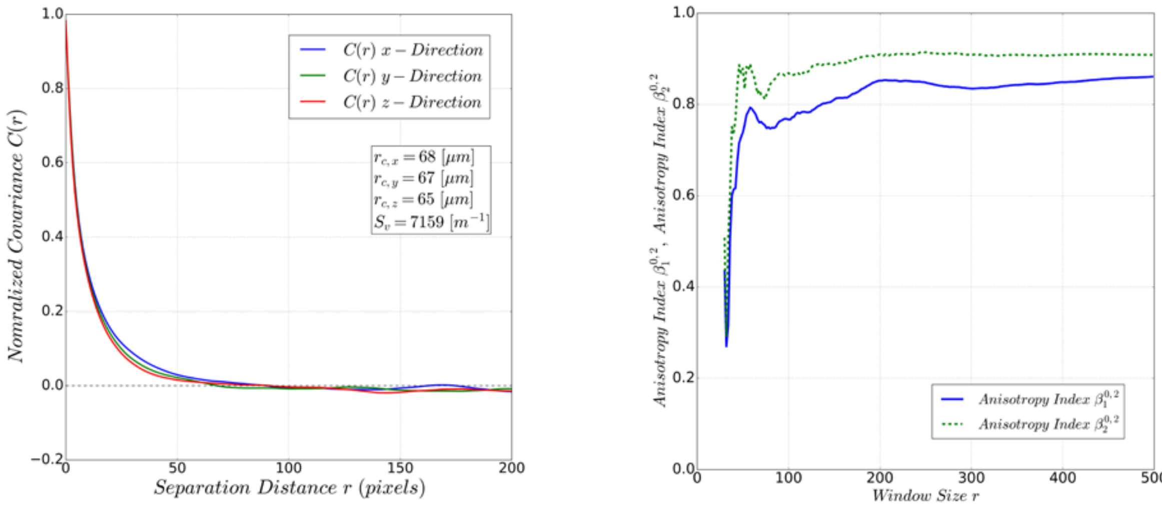

Appendix Figure 15:Left: Anisotropy indices derived from Minkowski tensor functionals. Right: Normalized directional Covariance of the Estaillades sample.

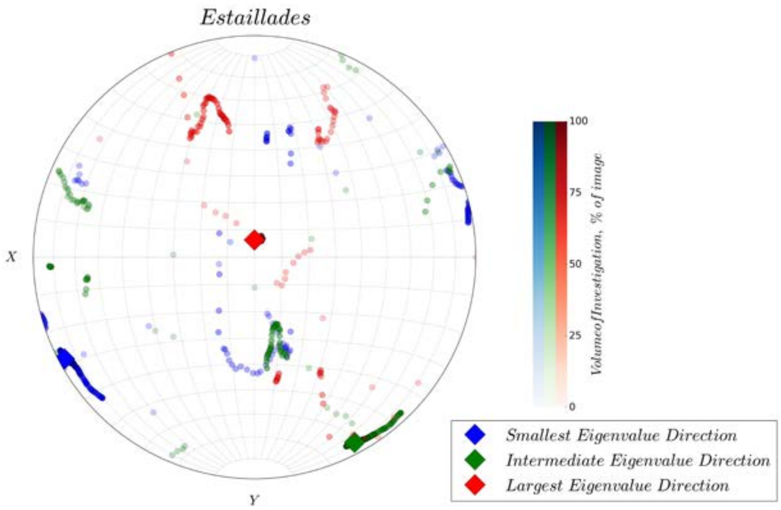

Appendix Figure 16: Stereonet projection of eigenvectors of Minkowski tensor $W_1^{0,2}$ of the Estaillades sample.

Results Summary		
Image Name	**Estaillades**	
Rock Type	**Carbonate**	
Property	**Value**	**Unit**
Image Resolution	6.62272	$[\mu m]$
Image Dimensions	(500, 500, 500)	(Nx, Ny, Nz) [voxel]
Covariance Analysis Results		
Porosity	0.12	[-]
Directional Characterstic Pore Size $[r_{c,x}, r_{c,y}, r_{c,z}]$	68,67,65	$[\mu m]$
Average Characteristic Pore Size $\bar{r_c}$	60	$[\mu m]$
Specific Surface Area	7159	$[m^{-1}]$
Minkowski Tensor Analysis		
Normalised Minkowski Functional $\widehat{W}_1^{0,2}$	$\begin{bmatrix} 0.315 & -0.004 & -0.002 \\ -0.004 & 0.320 & 0.004 \\ -0.002 & 0.004 & 0.364 \end{bmatrix}$	[-]
Normalised Minkowski Functional $\widehat{W}_2^{0,2}$	$\begin{bmatrix} 0.323 & -0.003 & -0.002 \\ -0.003 & 0.324 & 0.001 \\ -0.002 & 0.001 & 0.353 \end{bmatrix}$	[-]
Anisotropy Index $\beta_1^{0,2}$	0.86	[-]
Anisotropy Index $\beta_2^{0,2}$	0.91	[-]
Permeability Computation Results		
Effective Porosity	0.10	[-]
Directional Permeability	$\begin{bmatrix} 0.157 & - & - \\ - & 0.075 & - \\ - & - & 0.117 \end{bmatrix}$	$[D]$

Sample 4: Bentheimer

Orthogonal Image Projections:

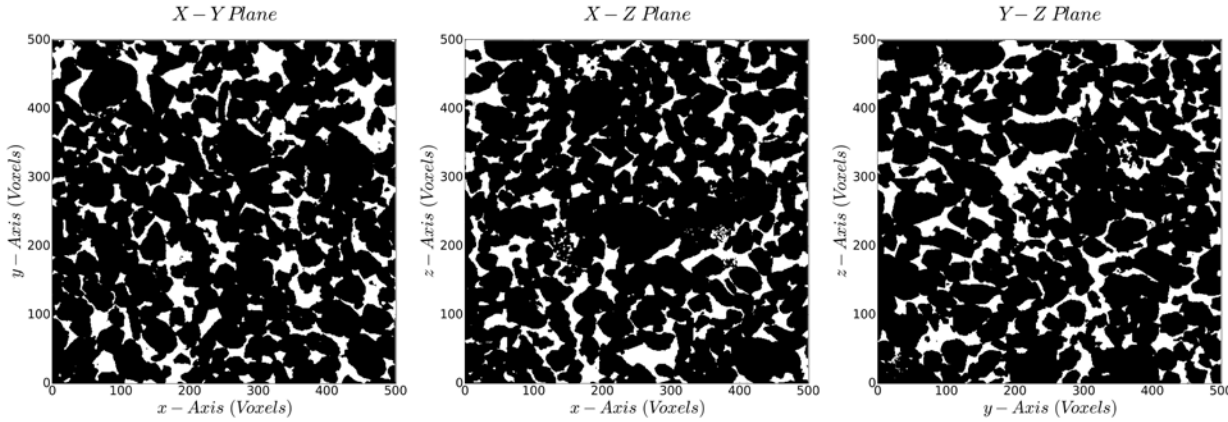

Appendix Figure 17 Orthogonal views of Bentheimer Image. Views seen from front of sample.

Sample Description:
Aenean at tortor luctus purus euismod aliquet at eu metus. Pellentesque tempor ac libero laoreet ullamcorper. Suspendisse blandit ante id orci iaculis vestibulum id quis lorem. Morbi fermentum iaculis ipsum ut congue. Phasellus bibendum ornare diam, sed tempus lacus pharetra et. Aenean quis laoreet urna, interdum dictum tellus. Mauris congue suscipit tortor et commodo.

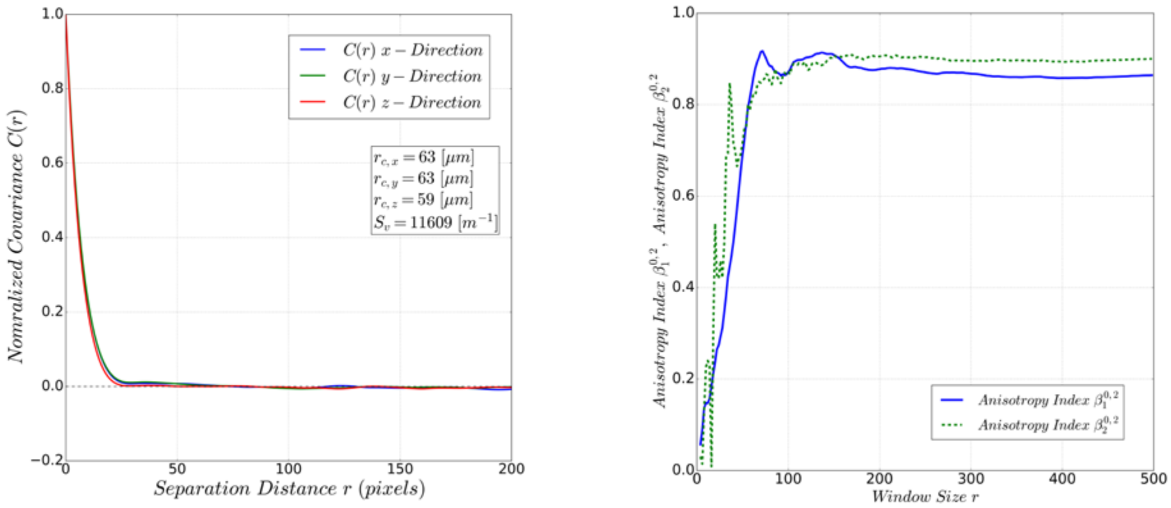

Appendix Figure 18:Left: Anisotropy indices derived from Minkowski tensor functionals. Right: Normalized directional Covariance of the Bentheimer sample.

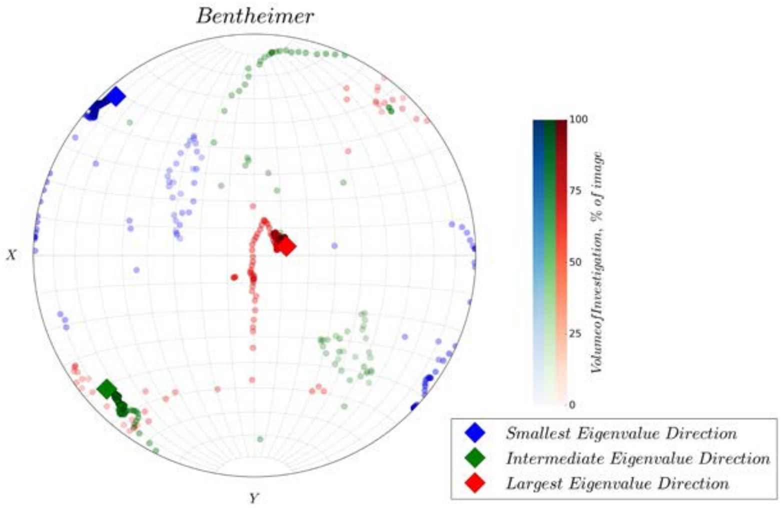

Appendix Figure 19: Stereonet projection of eigenvectors of Minkowski tensor $W_1^{0,2}$ of the Bentheimer sample.

Results Summary		
Image Name	**Bentheimer**	
Rock Type	**Sandstone**	
Property	**Value**	**Unit**
Image Resolution	6.007	$[\mu m]$
Image Dimensions	(500, 500, 500)	(Nx, Ny, Nz) [voxel]
Covariance Analysis Results		
Porosity	0.20	[-]
Directional Characterstic Pore Size $[r_{c,x}, r_{c,y}, r_{c,z}]$	63,63,59	$[\mu m]$
Average Characteristic Pore Size $\bar{r_c}$	55	$[\mu m]$
Specific Surface Area	11609	$[m^{-1}]$
Minkowski Tensor Analysis		
Normalised Minkowski Functional $\widehat{W}_1^{0,2}$	$\begin{bmatrix} 0.321 & 0.008 & -0.005 \\ 0.008 & 0.321 & 0.008 \\ -0.005 & 0.008 & 0.357 \end{bmatrix}$	[-]
Normalised Minkowski Functional $\widehat{W}_2^{0,2}$	$\begin{bmatrix} 0.324 & 0.004 & -0.002 \\ 0.004 & 0.334 & 0.006 \\ -0.002 & 0.006 & 0.331 \end{bmatrix}$	[-]
Anisotropy Index $\beta_1^{0,2}$	0.86	[-]
Anisotropy Index $\beta_2^{0,2}$	0.90	[-]
Permeability Computation Results		
Effective Porosity	0.20	[-]
Directional Permeability	$\begin{bmatrix} 2.779 & - & - \\ - & 2.867 & - \\ - & - & 2.329 \end{bmatrix}$	$[D]$

Sample 5: Doddington

Orthogonal Image Projections:

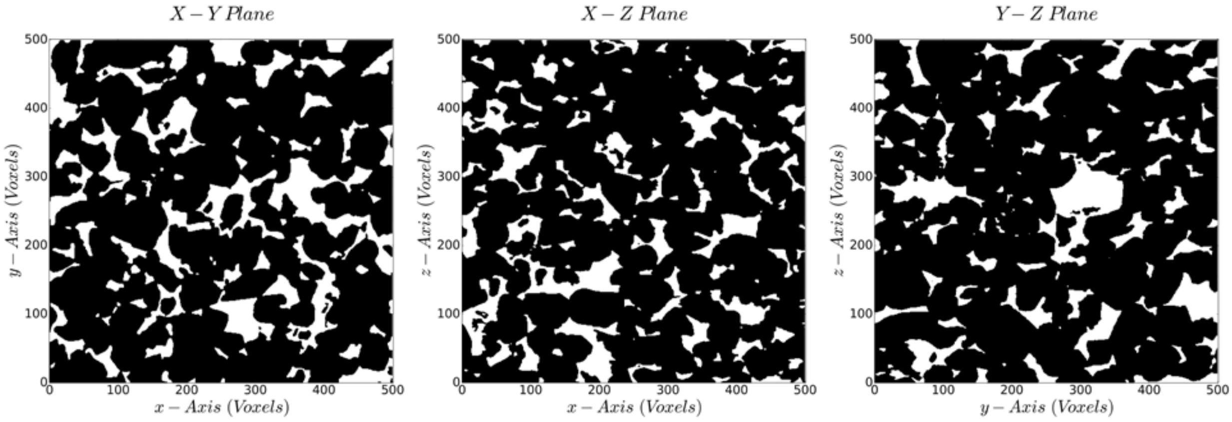

Appendix Figure 20 Orthogonal views of Doddington Image. Views seen from front of sample.

Sample Description:
Aenean at tortor luctus purus euismod aliquet at eu metus. Pellentesque tempor ac libero laoreet ullamcorper. Suspendisse blandit ante id orci iaculis vestibulum id quis lorem. Morbi fermentum iaculis ipsum ut congue. Phasellus bibendum ornare diam, sed tempus lacus pharetra et. Aenean quis laoreet urna, interdum dictum tellus. Mauris congue suscipit tortor et commodo.

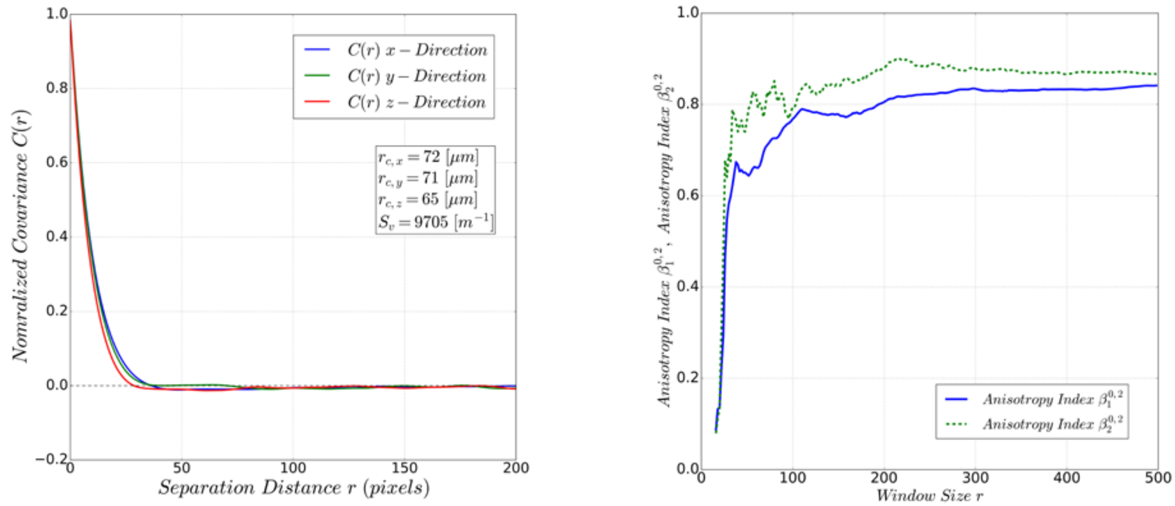

Appendix Figure 21:Left: Anisotropy indices derived from Minkowski tensor functionals. Right: Normalized directional Covariance of the Doddington sample.

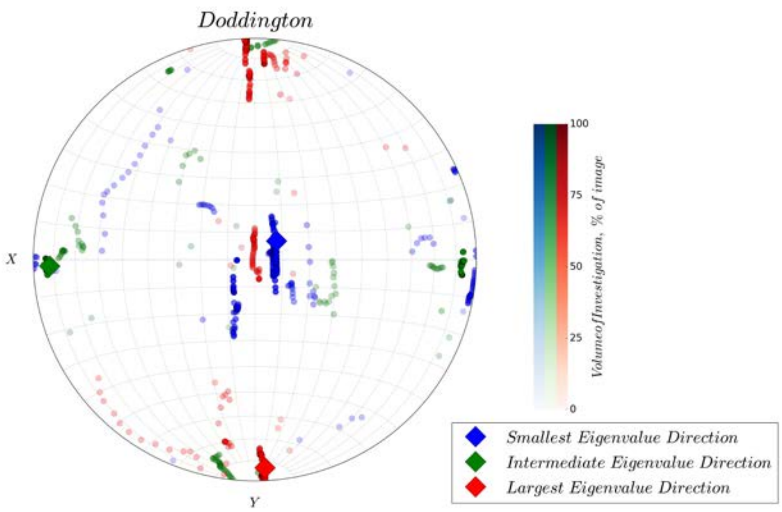

Appendix Figure 22: Stereonet projection of eigenvectors of Minkowski tensor $W_1^{0,2}$ of the Doddington sample.

Results Summary		
Image Name	**Doddington**	
Rock Type	**Sandstone**	
Property	**Value**	**Unit**
Image Resolution	5.3858	$[\mu m]$
Image Dimensions	(500, 500, 500)	(Nx, Ny, Nz) [voxel]
Covariance Analysis Results		
Porosity	0.19	[-]
Directional Characterstic Pore Size $[r_{c,x}, r_{c,y}, r_{c,z}]$	72,71,65	$[\mu m]$
Average Characteristic Pore Size $\bar{r_c}$	63	$[\mu m]$
Specific Surface Area	9705	$[m^{-1}]$
Minkowski Tensor Analysis		
Normalised Minkowski Functional $\widehat{W}_1^{0,2}$	$\begin{bmatrix} 0.313 & 0 & 0.003 \\ 0 & 0.316 & -0.008 \\ 0.003 & -0.008 & 0.371 \end{bmatrix}$	[-]
Normalised Minkowski Functional $\widehat{W}_2^{0,2}$	$\begin{bmatrix} 0.319 & -0.002 & 0 \\ -0.002 & 0.334 & -0.005 \\ 0 & -0.005 & 0.331 \end{bmatrix}$	[-]
Anisotropy Index $\beta_1^{0,2}$	0.84	[-]
Anisotropy Index $\beta_2^{0,2}$	0.87	[-]
Permeability Computation Results		
Effective Porosity	0.19	[-]
Directional Permeability	$\begin{bmatrix} 0.313 & - & - \\ - & 0.308 & - \\ - & - & 0.268 \end{bmatrix}$	$[D]$

Sample 6: Berea

Orthogonal Image Projections:

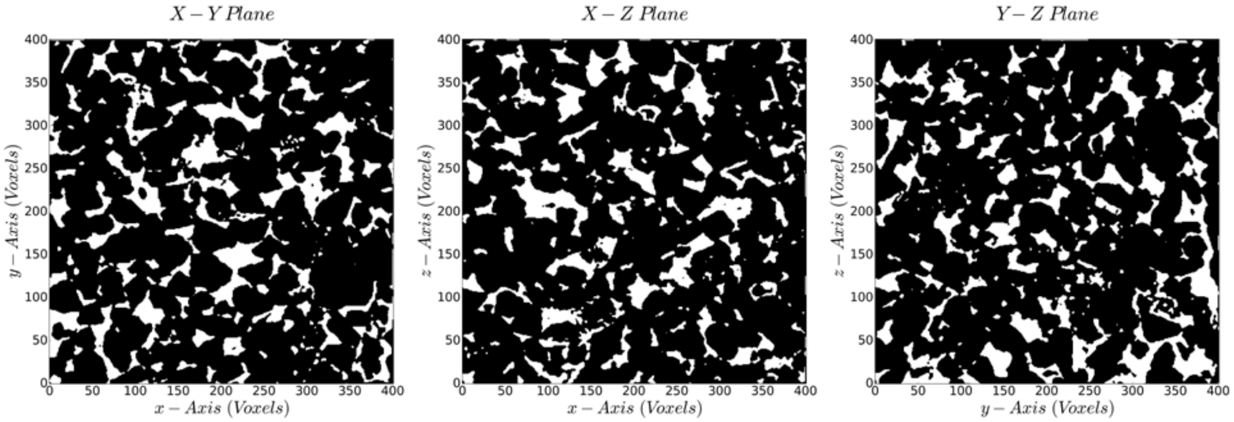

Appendix Figure 23 Orthogonal views of Berea Image. Views seen from front of sample.

Sample Description:
Aenean at tortor luctus purus euismod aliquet at eu metus. Pellentesque tempor ac libero laoreet ullamcorper. Suspendisse blandit ante id orci iaculis vestibulum id quis lorem. Morbi fermentum iaculis ipsum ut congue. Phasellus bibendum ornare diam, sed tempus lacus pharetra et. Aenean quis laoreet urna, interdum dictum tellus. Mauris congue suscipit tortor et commodo.

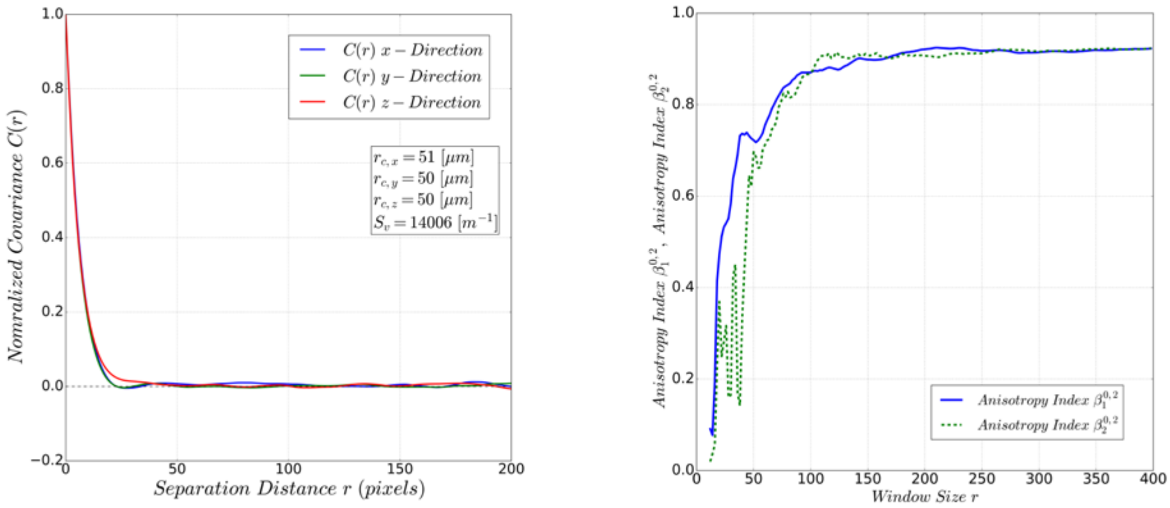

Appendix Figure 24:Left: Anisotropy indices derived from Minkowski tensor functionals. Right: Normalized directional Covariance of the Berea sample.

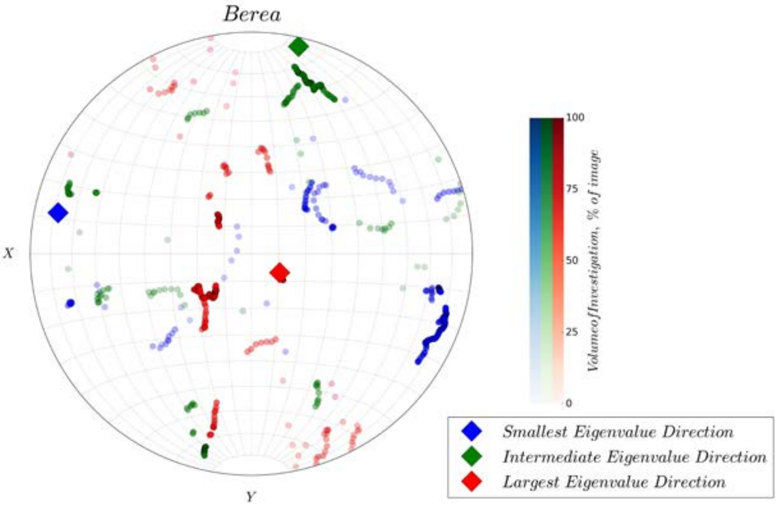

Appendix Figure 25: Stereonet projection of eigenvectors of Minkowski tensor $W_1^{0,2}$ of the Berea sample.

Results Summary		
Image Name	**Berea**	
Rock Type	**Sandstone**	
Property	**Value**	**Unit**
Image Resolution	5.345	$[\boldsymbol{\mu m}]$
Image Dimensions	(300, 300, 300)	(Nx, Ny, Nz) [voxel]
Covariance Analysis Results		
Porosity	0.20	[-]
Directional Characterstic Pore Size $[\boldsymbol{r_{c,x}}, \boldsymbol{r_{c,y}}, \boldsymbol{r_{c,z}}]$	51,50,50	$[\boldsymbol{\mu m}]$
Average Characteristic Pore Size $\bar{\boldsymbol{r}}_{\boldsymbol{c}}$	45	$[\boldsymbol{\mu m}]$
Specific Surface Area	14006	$[\boldsymbol{m^{-1}}]$
Minkowski Tensor Analysis		
Normalised Minkowski Functional $\widehat{\boldsymbol{W}}_{\boldsymbol{1}}^{\boldsymbol{0,2}}$	$\begin{bmatrix} \mathbf{0.321} & \mathbf{0.003} & \mathbf{0.005} \\ \mathbf{0.003} & \mathbf{0.335} & \mathbf{-0.002} \\ \mathbf{0.005} & \mathbf{-0.002} & \mathbf{0.344} \end{bmatrix}$	[-]
Normalised Minkowski Functional $\widehat{\boldsymbol{W}}_{\boldsymbol{2}}^{\boldsymbol{0,2}}$	$\begin{bmatrix} \mathbf{0.323} & \mathbf{0.001} & \mathbf{0.003} \\ \mathbf{0.001} & \mathbf{0.329} & \mathbf{-0.002} \\ \mathbf{0.003} & \mathbf{-0.002} & \mathbf{0.349} \end{bmatrix}$	[-]
Anisotropy Index $\boldsymbol{\beta}_{\boldsymbol{1}}^{\boldsymbol{0,2}}$	0.92	[-]
Anisotropy Index $\boldsymbol{\beta}_{\boldsymbol{2}}^{\boldsymbol{0,2}}$	0.92	[-]
Permeability Computation Results		
Effective Porosity		[-]
Directional Permeability	$\begin{bmatrix} \mathbf{1.378} & - & - \\ - & \mathbf{1.321} & - \\ - & - & \mathbf{1.208} \end{bmatrix}$	$[\boldsymbol{D}]$

Sample 7: S1

Orthogonal Image Projections:

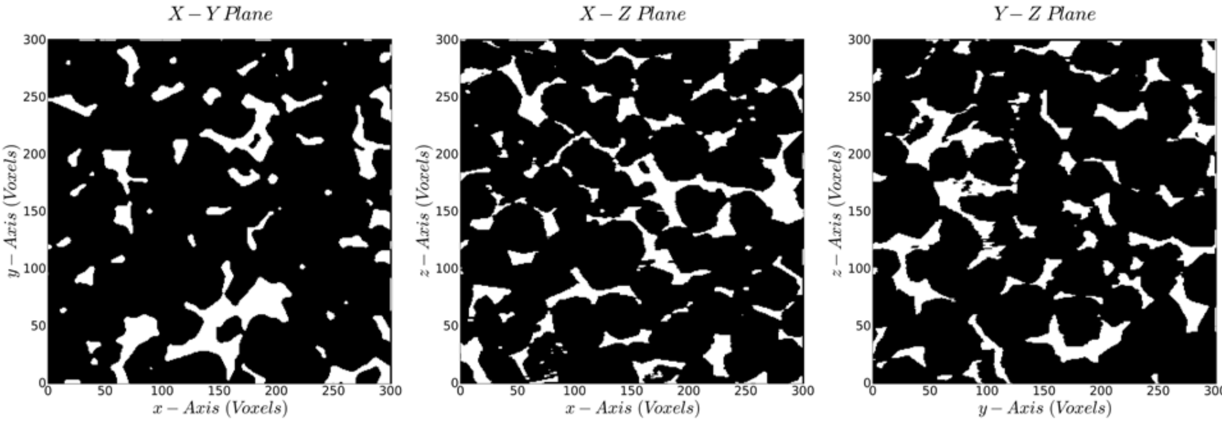

Appendix Figure 26 Orthogonal views of Image S1. Views seen from front of sample.

Sample Description:

Aenean at tortor luctus purus euismod aliquet at eu metus. Pellentesque tempor ac libero laoreet ullamcorper. Suspendisse blandit ante id orci iaculis vestibulum id quis lorem. Morbi fermentum iaculis ipsum ut congue. Phasellus bibendum ornare diam, sed tempus lacus pharetra et. Aenean quis laoreet urna, interdum dictum tellus. Mauris congue suscipit tortor et commodo.

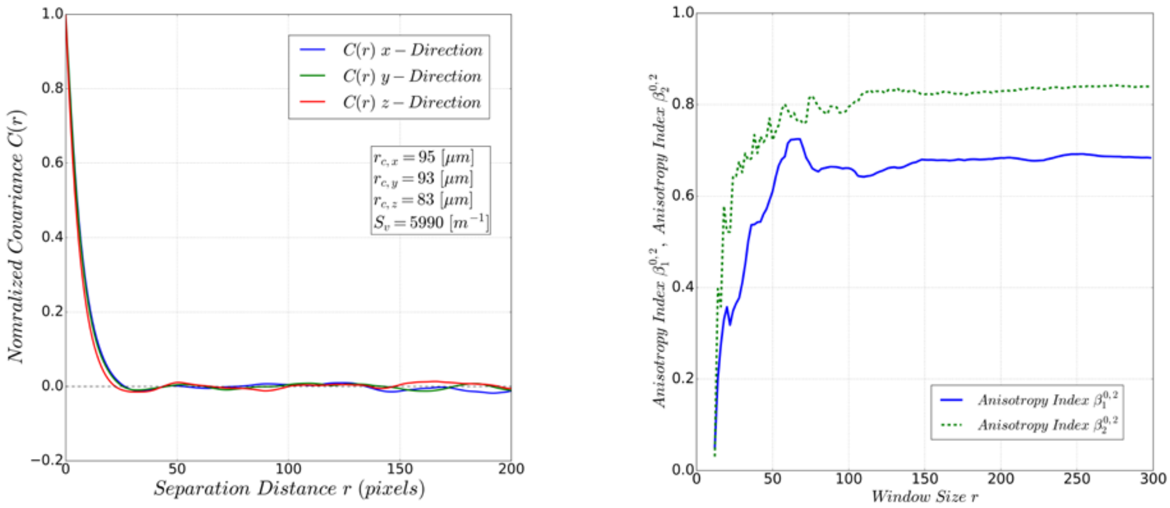

Appendix Figure 27:Left: Anisotropy indices derived from Minkowski tensor functionals. Right: Normalized directional Covariance of the S1 sample.

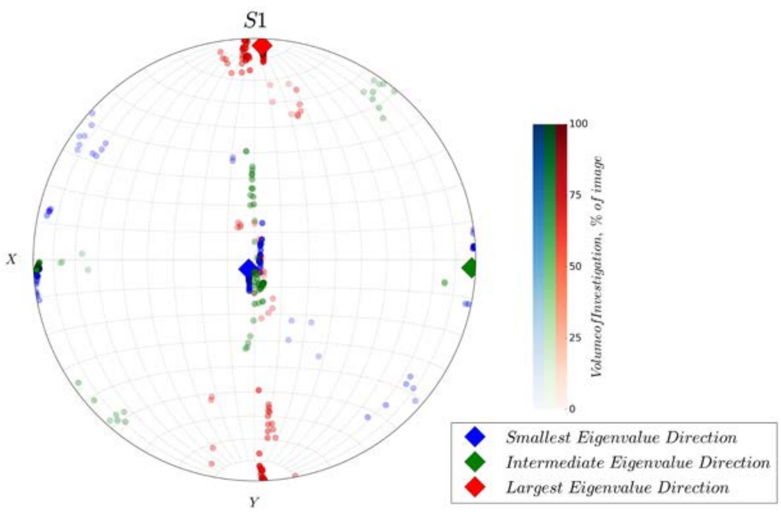

Appendix Figure 28: Stereonet projection of eigenvectors of Minkowski tensor $W_1^{0,2}$ of the S1sample.

Results Summary		
Image Name	**S1**	
Rock Type	**Sandstone**	
Property	**Value**	**Unit**
Image Resolution	8.683	$[\mu m]$
Image Dimensions	(300, 300, 300)	(Nx, Ny, Nz) [voxel]
Covariance Analysis Results		
Porosity	0.14	[-]
Directional Characterstic Pore Size $[r_{c,x}, r_{c,y}, r_{c,z}]$	95,93,83	$[\mu m]$
Average Characteristic Pore Size $\bar{r_c}$	81	$[\mu m]$
Specific Surface Area	5990	$[m^{-1}]$
Minkowski Tensor Analysis		
Normalised Minkowski Functional $\widehat{W}_1^{0,2}$	$\begin{bmatrix} 0.287 & 0 & 0 \\ 0 & 0.295 & 0 \\ 0 & 0 & 0.419 \end{bmatrix}$	[-]
Normalised Minkowski Functional $\widehat{W}_2^{0,2}$	$\begin{bmatrix} 0.313 & 0 & 0 \\ 0 & 0.315 & -0.002 \\ 0 & -0.002 & 0.372 \end{bmatrix}$	[-]
Anisotropy Index $\beta_1^{0,2}$	0.68	[-]
Anisotropy Index $\beta_2^{0,2}$	0.84	[-]
Permeability Computation Results		
Effective Porosity	0.13	[-]
Directional Permeability	$\begin{bmatrix} 1.995 & - & - \\ - & 1.775 & - \\ - & - & 1.329 \end{bmatrix}$	$[D]$

Sample 8: S2

Orthogonal Image Projections:

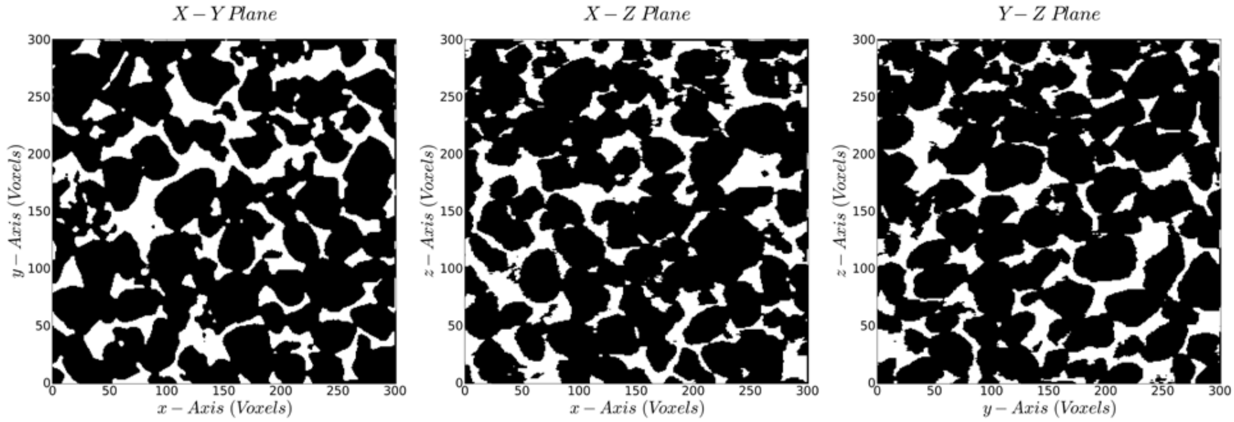

Appendix Figure 29 Orthogonal views of Image S2. Views seen from front of sample.

Sample Description:
Aenean at tortor luctus purus euismod aliquet at eu metus. Pellentesque tempor ac libero laoreet ullamcorper. Suspendisse blandit ante id orci iaculis vestibulum id quis lorem. Morbi fermentum iaculis ipsum ut congue. Phasellus bibendum ornare diam, sed tempus lacus pharetra et. Aenean quis laoreet urna, interdum dictum tellus. Mauris congue suscipit tortor et commodo.

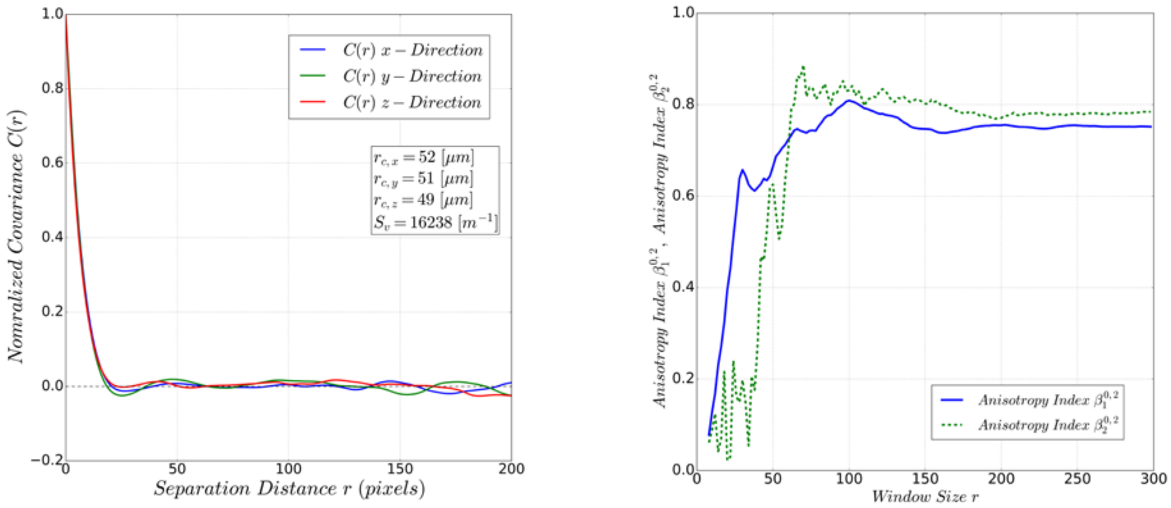

Appendix Figure 30:Left: Anisotropy indices derived from Minkowski tensor functionals. Right: Normalized directional Covariance of the S2sample.

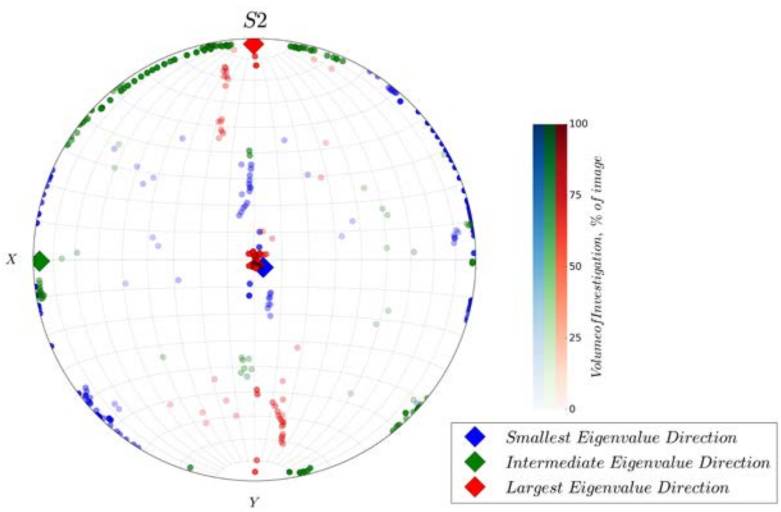

Appendix Figure 31: Stereonet projection of eigenvectors of Minkowski tensor $W_1^{0,2}$ of the S2sample.

Results Summary		
Image Name	**S2**	
Rock Type	**Sandstone**	
Property	**Value**	**Unit**
Image Resolution	4.956	$[\mu m]$
Image Dimensions	(300, 300, 300)	(Nx, Ny, Nz) [voxel]
Covariance Analysis Results		
Porosity	0.25	[-]
Directional Characterstic Pore Size $[r_{c,x}, r_{c,y}, r_{c,z}]$	52,51,49	$[\mu m]$
Average Characteristic Pore Size $\bar{r_c}$	45	$[\mu m]$
Specific Surface Area	16238	$[m^{-1}]$
Minkowski Tensor Analysis		
Normalised Minkowski Functional $\widehat{W}_1^{0,2}$	$\begin{bmatrix} 0.300 & 0 & 0 \\ 0 & 0.303 & 0 \\ 0 & 0 & 0.398 \end{bmatrix}$	[-]
Normalised Minkowski Functional $\widehat{W}_2^{0,2}$	$\begin{bmatrix} 0.315 & 0.01 & 0.002 \\ 0.01 & 0.306 & -0.008 \\ 0.002 & -0.008 & 0.379 \end{bmatrix}$	[-]
Anisotropy Index $\beta_1^{0,2}$	0.75	[-]
Anisotropy Index $\beta_2^{0,2}$	0.78	[-]
Permeability Computation Results		
Effective Porosity	0.25	[-]
Directional Permeability	$\begin{bmatrix} 4.375 & - & - \\ - & 4.035 & - \\ - & - & 3.439 \end{bmatrix}$	$[D]$

Sample 9: S3

Orthogonal Image Projections:

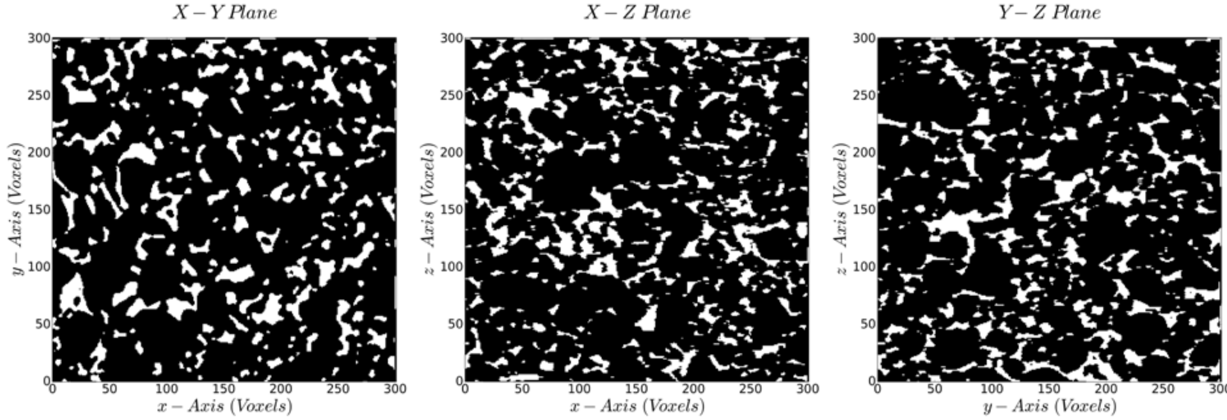

Appendix Figure 32 Orthogonal views of S3 Image. Views seen from front of sample.

Sample Description:

Aenean at tortor luctus purus euismod aliquet at eu metus. Pellentesque tempor ac libero laoreet ullamcorper. Suspendisse blandit ante id orci iaculis vestibulum id quis lorem. Morbi fermentum iaculis ipsum ut congue. Phasellus bibendum ornare diam, sed tempus lacus pharetra et. Aenean quis laoreet urna, interdum dictum tellus. Mauris congue suscipit tortor et commodo.

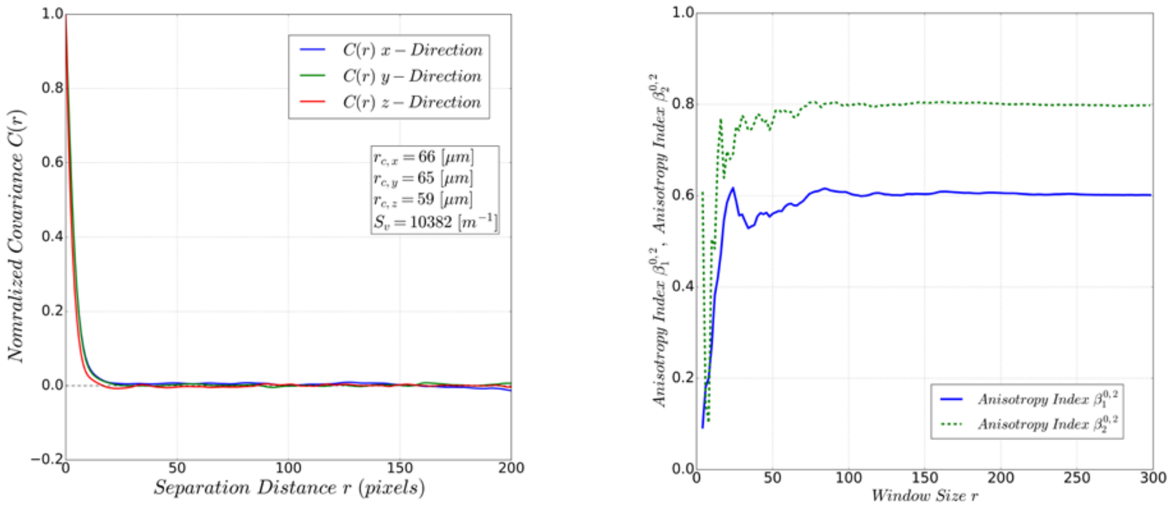

Appendix Figure 33:Left: Anisotropy indices derived from Minkowski tensor functionals. Right: Normalized directional Covariance of the S3 sample.

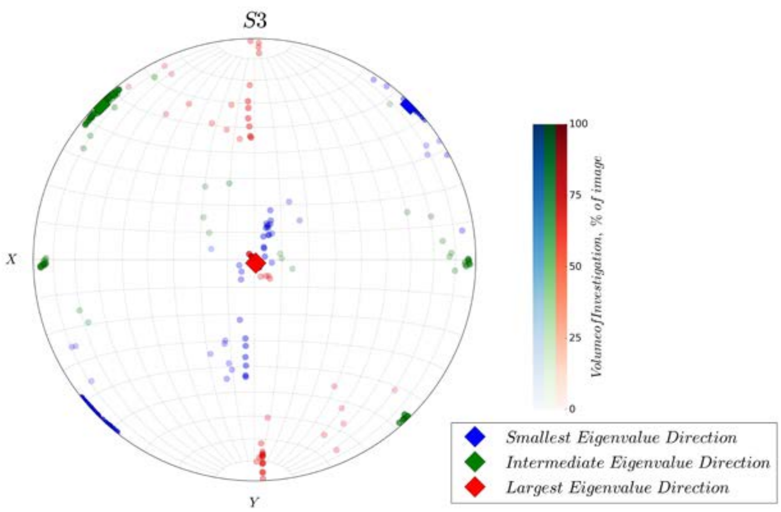

Appendix Figure 34: Stereonet projection of eigenvectors of Minkowski tensor $W_1^{0,2}$ of the S3 sample.

Results Summary		
Image Name	**S3**	
Rock Type	**Sandstone**	
Property	**Value**	**Unit**
Image Resolution	9.1	$[\mu m]$
Image Dimensions	(300, 300, 300)	(Nx, Ny, Nz) [voxel]
Covariance Analysis Results		
Porosity	0.17	[-]
Directional Characterstic Pore Size $[r_{c,x}, r_{c,y}, r_{c,z}]$	66,65,59	$[\mu m]$
Average Characteristic Pore Size $\bar{r_c}$	54	$[\mu m]$
Specific Surface Area	10382	$[m^{-1}]$
Minkowski Tensor Analysis		
Normalised Minkowski Functional $\widehat{W}_1^{0,2}$	$\begin{bmatrix} 0.276 & -0.007 & 0.002 \\ -0.007 & 0.276 & -0.004 \\ 0.002 & -0.004 & 0.447 \end{bmatrix}$	[-]
Normalised Minkowski Functional $\widehat{W}_2^{0,2}$	$\begin{bmatrix} 0.309 & 0 & 0 \\ 0 & 0.307 & 0 \\ 0 & 0 & 0.383 \end{bmatrix}$	[-]
Anisotropy Index $\beta_1^{0,2}$	0.60	[-]
Anisotropy Index $\beta_2^{0,2}$	0.79	[-]
Permeability Computation Results		
Effective Porosity	0.17	[-]
Directional Permeability	$\begin{bmatrix} 0.145 & - & - \\ - & 0.425 & - \\ - & - & 0.110 \end{bmatrix}$	$[D]$

Sample 10: S4

Orthogonal Image Projections:

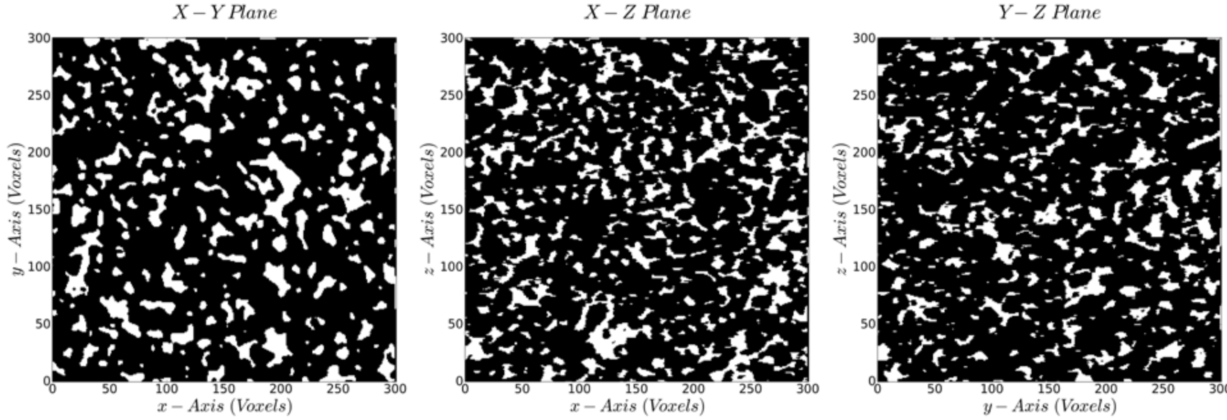

Appendix Figure 35 Orthogonal views of image S4. Views seen from front of sample.

Sample Description:
Aenean at tortor luctus purus euismod aliquet at eu metus. Pellentesque tempor ac libero laoreet ullamcorper. Suspendisse blandit ante id orci iaculis vestibulum id quis lorem. Morbi fermentum iaculis ipsum ut congue. Phasellus bibendum ornare diam, sed tempus lacus pharetra et. Aenean quis laoreet urna, interdum dictum tellus. Mauris congue suscipit tortor et commodo.

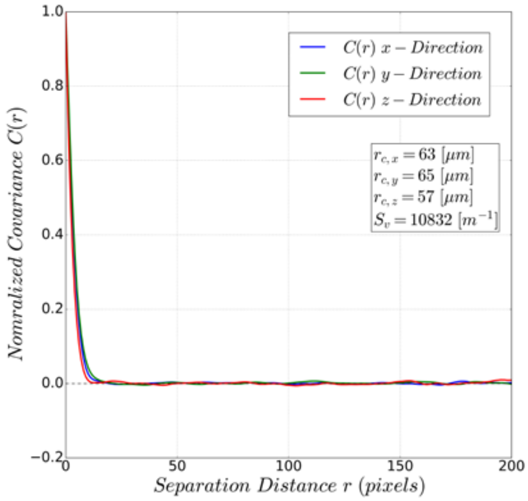

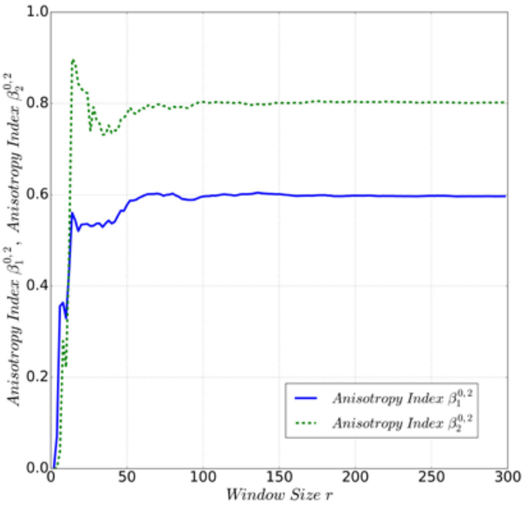

Appendix Figure 36:Left: Anisotropy indices derived from Minkowski tensor functionals. Right: Normalized directional Covariance of the S4 sample.

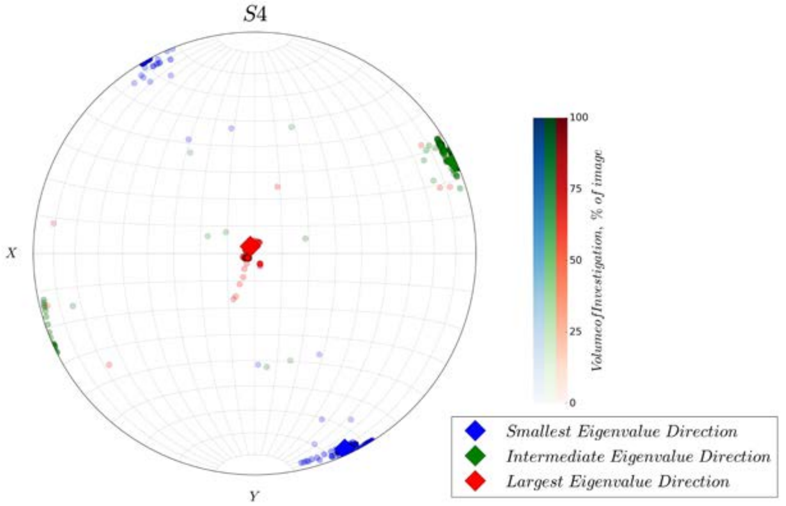

Appendix Figure 37: Stereonet projection of eigenvectors of Minkowski tensor $W_1^{0,2}$ of the S4 sample.

Results Summary		
Image Name	**S4**	
Rock Type	**Sandstone**	
Property	**Value**	**Unit**
Image Resolution	8.96	$[\boldsymbol{\mu m}]$
Image Dimensions	(300, 300, 300)	(Nx, Ny, Nz) [voxel]
Covariance Analysis Results		
Porosity	0.17	[-]
Directional Characterstic Pore Size $[\boldsymbol{r_{c,x}}, \boldsymbol{r_{c,y}}, \boldsymbol{r_{c,z}}]$	63,65,57	$[\boldsymbol{\mu m}]$
Average Characteristic Pore Size $\bar{\boldsymbol{r_c}}$	52	$[\boldsymbol{\mu m}]$
Specific Surface Area	10832	$[\boldsymbol{m^{-1}}]$
Minkowski Tensor Analysis		
Normalised Minkowski Functional $\widehat{\boldsymbol{W}}_1^{0,2}$	$\begin{bmatrix} 0.282 & 0.008 & 0 \\ 0.008 & 0.270 & -0.009 \\ 0 & -0.009 & 0.445 \end{bmatrix}$	[-]
Normalised Minkowski Functional $\widehat{\boldsymbol{W}}_2^{0,2}$	$\begin{bmatrix} 0.314 & 0 & 0 \\ 0 & 0.307 & 0 \\ 0 & 0 & 0.379 \end{bmatrix}$	[-]
Anisotropy Index $\boldsymbol{\beta}_1^{0,2}$	0.59	[-]
Anisotropy Index $\boldsymbol{\beta}_2^{0,2}$	0.80	[-]
Permeability Computation Results		
Effective Porosity	0.17	[-]
Directional Permeability	$\begin{bmatrix} 0.276 & - & - \\ - & 0.292 & - \\ - & - & 0.218 \end{bmatrix}$	$[\boldsymbol{mD}]$

Sample 11: S5

Orthogonal Image Projections:

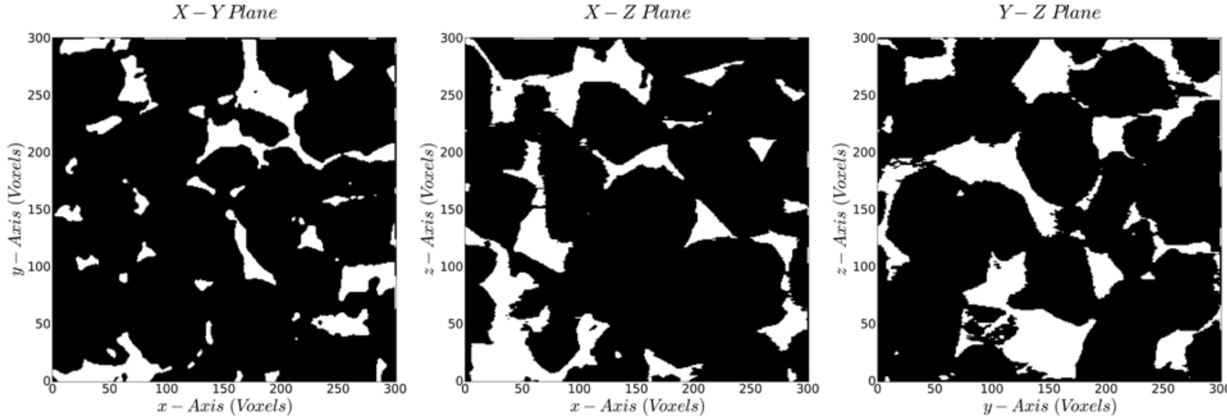

Appendix Figure 38 Orthogonal views of image S5. Views seen from front of sample.

Sample Description:

Aenean at tortor luctus purus euismod aliquet at eu metus. Pellentesque tempor ac libero laoreet ullamcorper. Suspendisse blandit ante id orci iaculis vestibulum id quis lorem. Morbi fermentum iaculis ipsum ut congue. Phasellus bibendum ornare diam, sed tempus lacus pharetra et. Aenean quis laoreet urna, interdum dictum tellus. Mauris congue suscipit tortor et commodo.

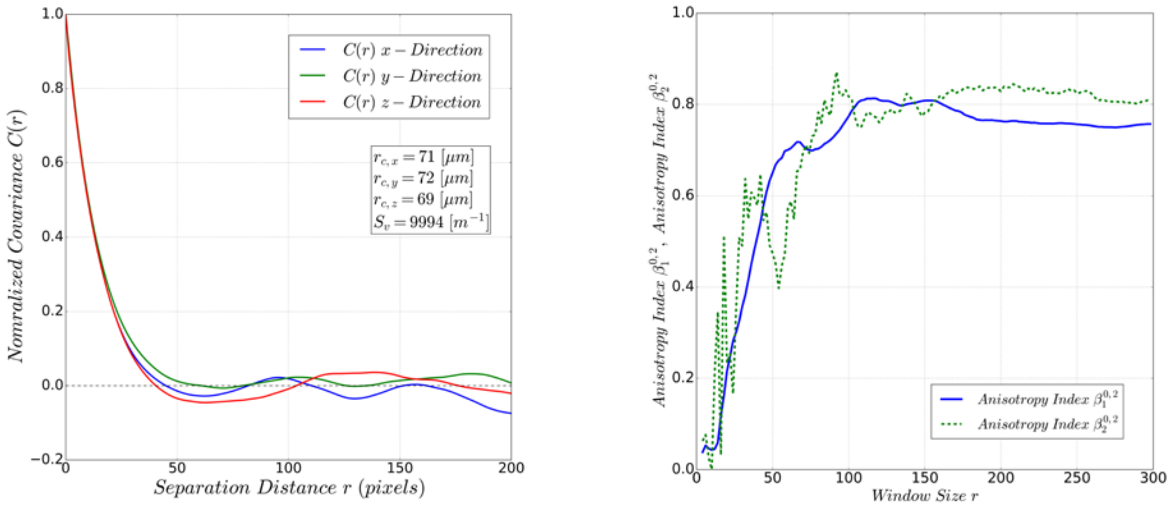

Appendix Figure 39:Left: Anisotropy indices derived from Minkowski tensor functionals. Right: Normalized directional Covariance of the S5 sample.

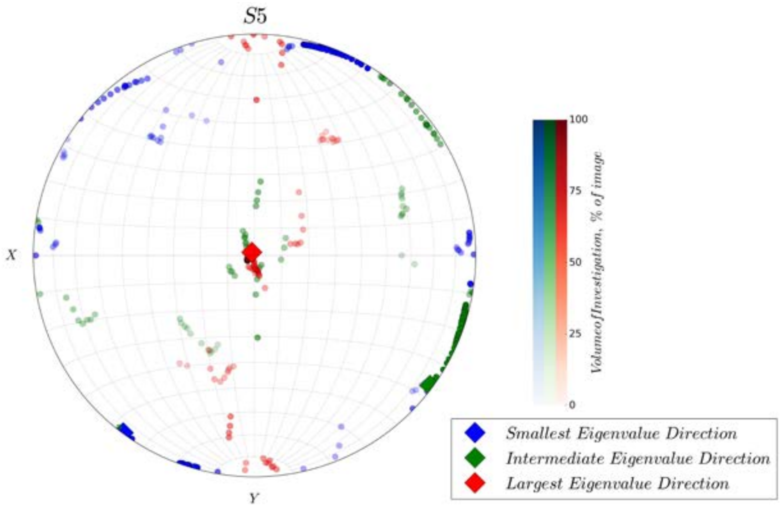

Appendix Figure 40: Stereonet projection of eigenvectors of Minkowski tensor $W_1^{0,2}$ of the S5 sample.

Results Summary		
Image Name	**S5**	
Rock Type	**Sandstone**	
Property	**Value**	**Unit**
Image Resolution	3.997	$[\mu m]$
Image Dimensions	(300, 300, 300)	(Nx, Ny, Nz) [voxel]
Covariance Analysis Results		
Porosity	0.21	[-]
Directional Characterstic Pore Size $[r_{c,x}, r_{c,y}, r_{c,z}]$	71,72,69	$[\mu m]$
Average Characteristic Pore Size $\bar{r_c}$	67	$[\mu m]$
Specific Surface Area	9994	$[m^{-1}]$
Minkowski Tensor Analysis		
Normalised Minkowski Functional $\widehat{W}_1^{0,2}$	$\begin{bmatrix} 0.304 & -0.004 & 0 \\ -0.004 & 0.301 & 0.002 \\ 0 & 0.002 & 0.394 \end{bmatrix}$	[-]
Normalised Minkowski Functional $\widehat{W}_2^{0,2}$	$\begin{bmatrix} 0.310 & 0.008 & -0.004 \\ 0.008 & 0.315 & 0.003 \\ -0.004 & 0.003 & 0.374 \end{bmatrix}$	[-]
Anisotropy Index $\beta_1^{0,2}$	0.76	[-]
Anisotropy Index $\beta_2^{0,2}$	0.81	[-]
Permeability Computation Results		
Effective Porosity	0.21	[-]
Directional Permeability	$\begin{bmatrix} 4.745 & - & - \\ - & 4.938 & - \\ - & - & 4.498 \end{bmatrix}$	$[D]$

Sample 12: S6

Orthogonal Image Projections:

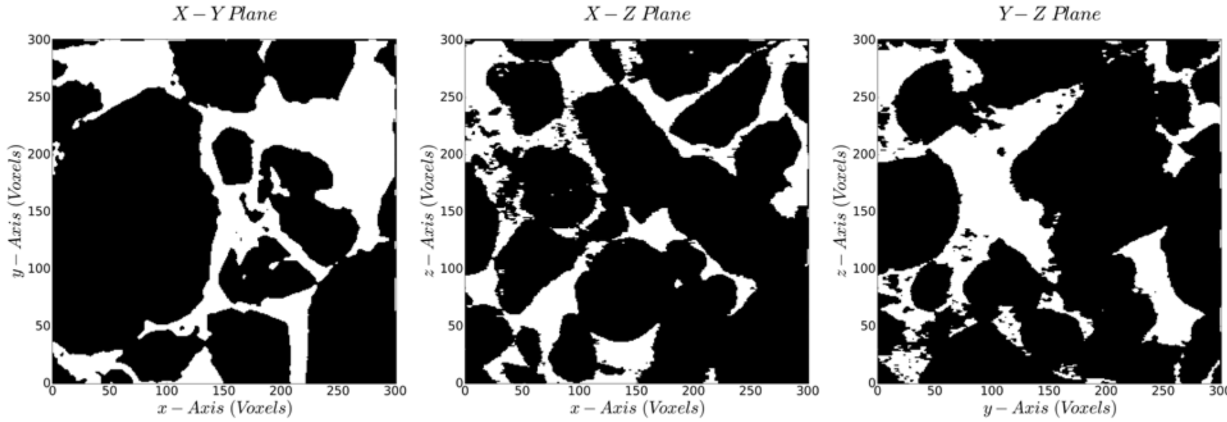

Appendix Figure 41 Orthogonal views of S6 Image. Views seen from front of sample.

Sample Description:
Aenean at tortor luctus purus euismod aliquet at eu metus. Pellentesque tempor ac libero laoreet ullamcorper. Suspendisse blandit ante id orci iaculis vestibulum id quis lorem. Morbi fermentum iaculis ipsum ut congue. Phasellus bibendum ornare diam, sed tempus lacus pharetra et. Aenean quis laoreet urna, interdum dictum tellus. Mauris congue suscipit tortor et commodo.

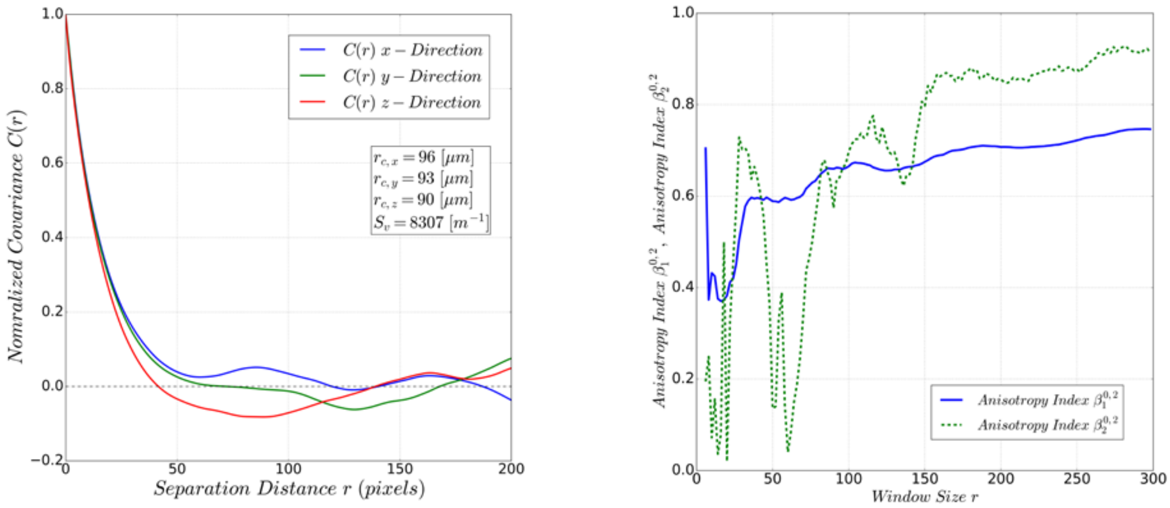

Appendix Figure 42:Left: Anisotropy indices derived from Minkowski tensor functionals. Right: Normalized directional Covariance of the S6 sample.

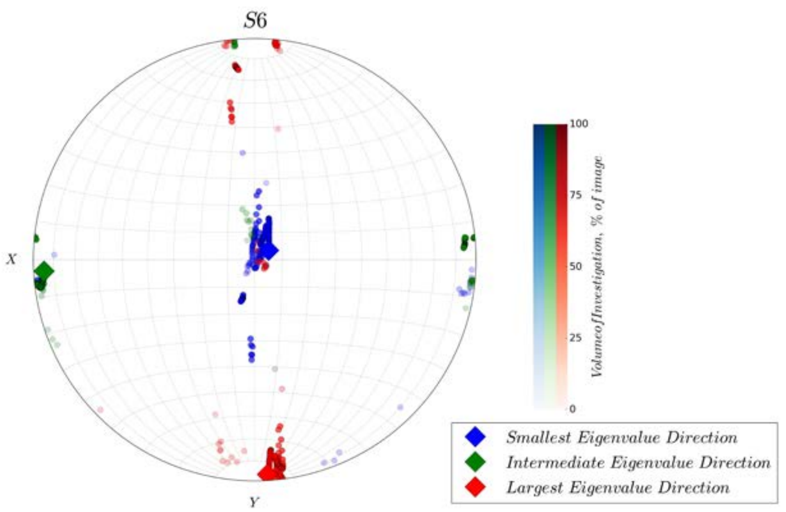

Appendix Figure 43: Stereonet projection of eigenvectors of Minkowski tensor $W_1^{0,2}$ of the S6 sample.

Results Summary		
Image Name	**S6**	
Rock Type	**Sandstone**	
Property	**Value**	**Unit**
Image Resolution	5.1	$[\mu m]$
Image Dimensions	(300, 300, 300)	(Nx, Ny, Nz) [voxel]
Covariance Analysis Results		
Porosity	0.24	[-]
Directional Characterstic Pore Size $[r_{c,x}, r_{c,y}, r_{c,z}]$	96,93,90	$[\mu m]$
Average Characteristic Pore Size $\bar{r_c}$	88	$[\mu m]$
Specific Surface Area	8307	$[m^{-1}]$
Minkowski Tensor Analysis		
Normalised Minkowski Functional $\widehat{W}_1^{0,2}$	$\begin{bmatrix} 0.335 & -0.001 & 0.006 \\ -0.001 & 0.307 & -0.008 \\ 0.006 & -0.008 & 0.396 \end{bmatrix}$	[-]
Normalised Minkowski Functional $\widehat{W}_2^{0,2}$	$\begin{bmatrix} 0.324 & 0.003 & 0.007 \\ 0.003 & 0.328 & 0.005 \\ 0.007 & 0.005 & 0.348 \end{bmatrix}$	[-]
Anisotropy Index $\beta_1^{0,2}$	0.75	[-]
Anisotropy Index $\beta_2^{0,2}$	0.91	[-]
Permeability Computation Results		
Effective Porosity	0.24	[-]
Directional Permeability	$\begin{bmatrix} 11.43 & - & - \\ - & 10.82 & - \\ - & - & 11.09 \end{bmatrix}$	$[D]$

Sample 13: S7

Orthogonal Image Projections:

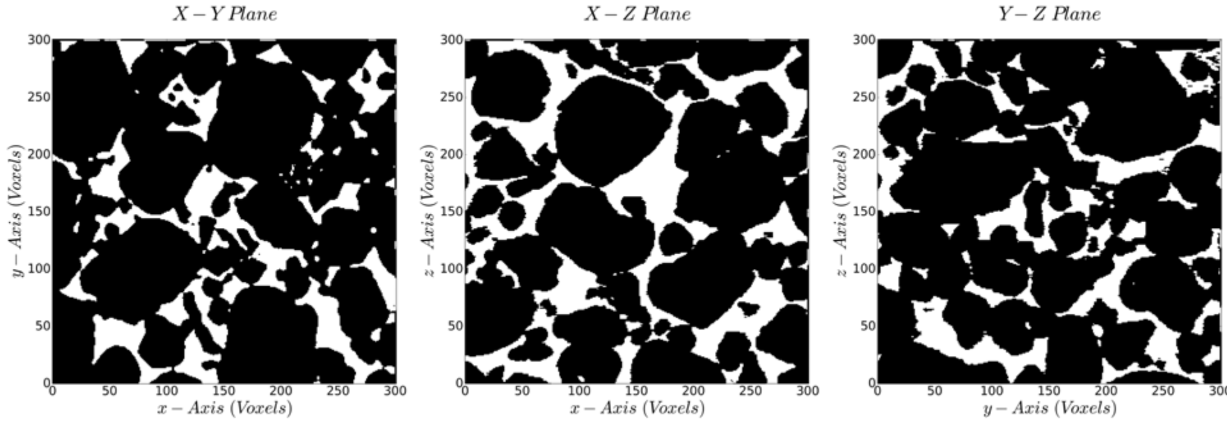

Appendix Figure 44 Orthogonal views of image S7. Views seen from front of sample.

Sample Description:

Aenean at tortor luctus purus euismod aliquet at eu metus. Pellentesque tempor ac libero laoreet ullamcorper. Suspendisse blandit ante id orci iaculis vestibulum id quis lorem. Morbi fermentum iaculis ipsum ut congue. Phasellus bibendum ornare diam, sed tempus lacus pharetra et. Aenean quis laoreet urna, interdum dictum tellus. Mauris congue suscipit tortor et commodo.

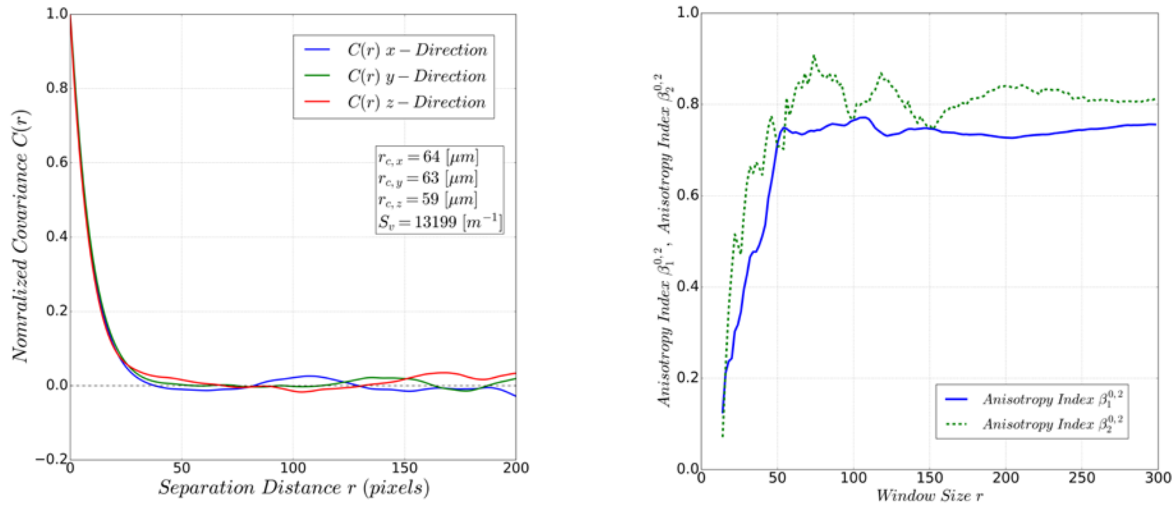

Appendix Figure 45:Left: Anisotropy indices derived from Minkowski tensor functionals. Right: Normalized directional Covariance of the S7 sample.

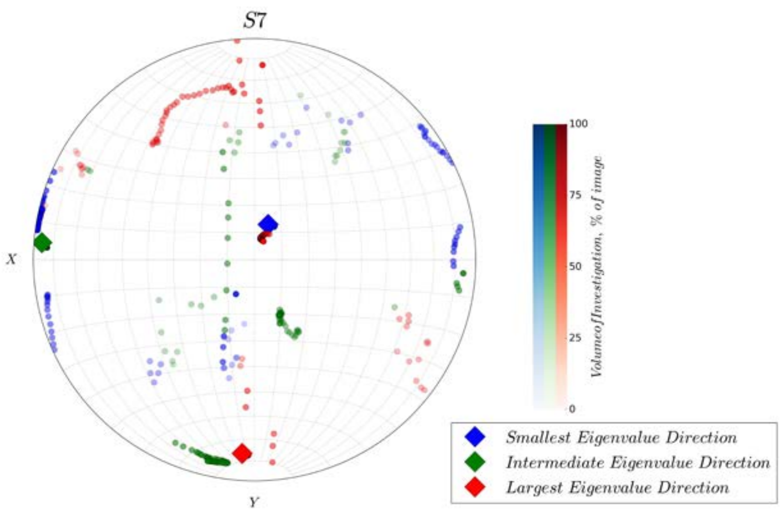

Appendix Figure 46: Stereonet projection of eigenvectors of Minkowski tensor $W_1^{0,2}$ of the S7 sample.

Results Summary		
Image Name	**S7**	
Rock Type	**Sandstone**	
Property	**Value**	**Unit**
Image Resolution	4.803	$[\boldsymbol{\mu m}]$
Image Dimensions	(300, 300, 300)	(Nx, Ny, Nz) [voxel]
Covariance Analysis Results		
Porosity	0.25	[-]
Directional Characterstic Pore Size $[\boldsymbol{r_{c,x}}, \boldsymbol{r_{c,y}}, \boldsymbol{r_{c,z}}]$	64,63,59	$[\boldsymbol{\mu m}]$
Average Characteristic Pore Size $\bar{\boldsymbol{r}}_{\boldsymbol{c}}$	57	$[\boldsymbol{\mu m}]$
Specific Surface Area	13199	$[\boldsymbol{m^{-1}}]$
Minkowski Tensor Analysis		
Normalised Minkowski Functional $\widehat{\boldsymbol{W}}_{\boldsymbol{1}}^{\boldsymbol{0,2}}$	$\begin{bmatrix} 0.301 & 0 & 0 \\ 0 & 0.303 & 0 \\ 0 & 0 & 0.396 \end{bmatrix}$	[-]
Normalised Minkowski Functional $\widehat{\boldsymbol{W}}_{\boldsymbol{2}}^{\boldsymbol{0,2}}$	$\begin{bmatrix} 0.304 & -0.003 & -0.004 \\ -0.004 & 0.323 & 0.003 \\ -0.004 & 0.003 & 0.373 \end{bmatrix}$	[-]
Anisotropy Index $\boldsymbol{\beta_1^{0,2}}$	0.76	[-]
Anisotropy Index $\boldsymbol{\beta_2^{0,2}}$	0.81	[-]
Permeability Computation Results		
Effective Porosity	0.25	[-]
Directional Permeability	$\begin{bmatrix} 7.364 & - & - \\ - & 7.694 & - \\ - & - & 6.117 \end{bmatrix}$	$[\boldsymbol{D}]$

Sample 14: S8

Orthogonal Image Projections:

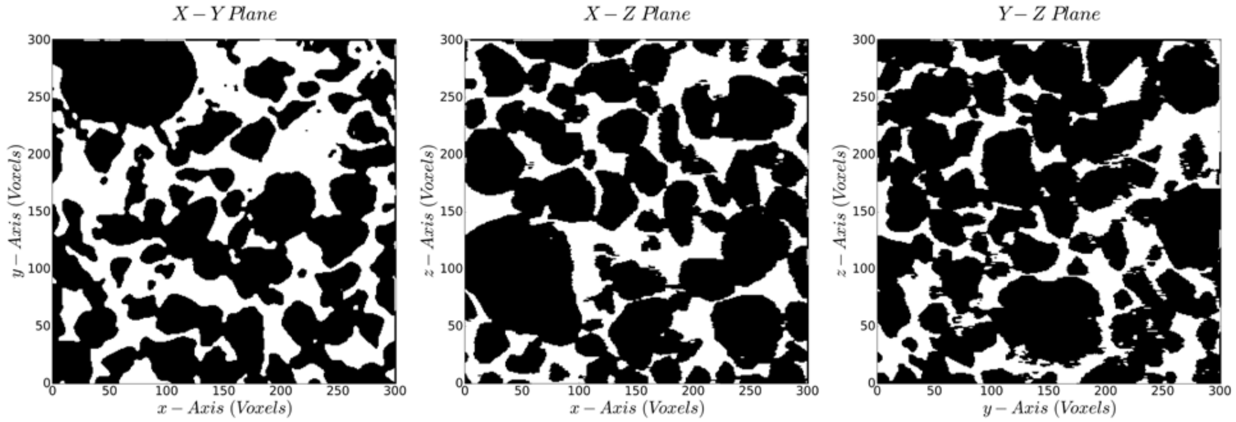

Appendix Figure 47 Orthogonal views of image S8. Views seen from front of sample.

Sample Description:

Aenean at tortor luctus purus euismod aliquet at eu metus. Pellentesque tempor ac libero laoreet ullamcorper. Suspendisse blandit ante id orci iaculis vestibulum id quis lorem. Morbi fermentum iaculis ipsum ut congue. Phasellus bibendum ornare diam, sed tempus lacus pharetra et. Aenean quis laoreet urna, interdum dictum tellus. Mauris congue suscipit tortor et commodo.

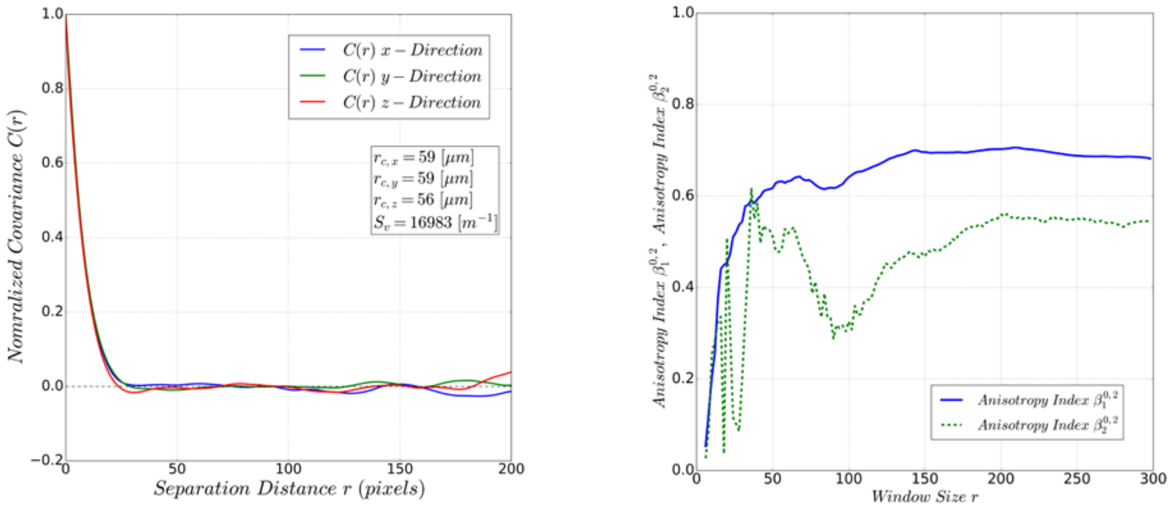

Appendix Figure 48:Left: Anisotropy indices derived from Minkowski tensor functionals. Right: Normalized directional Covariance of the S8 sample.

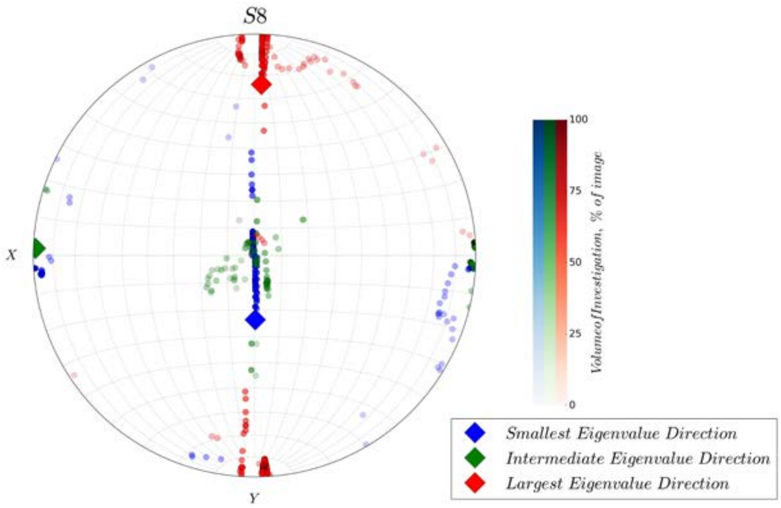

Appendix Figure 49: Stereonet projection of eigenvectors of Minkowski tensor $W_1^{0,2}$ of the S8 sample.

Results Summary		
Image Name	**S8**	
Rock Type	**Sandstone**	
Property	**Value**	**Unit**
Image Resolution	4.892	$[\mu m]$
Image Dimensions	(300, 300, 300)	(Nx, Ny, Nz) [voxel]
Covariance Analysis Results		
Porosity	0.34	[-]
Directional Characterstic Pore Size $[r_{c,x}, r_{c,y}, r_{c,z}]$	59,59,56	$[\mu m]$
Average Characteristic Pore Size $\bar{r_c}$	53	$[\mu m]$
Specific Surface Area	16983	$[m^{-1}]$
Minkowski Tensor Analysis		
Normalised Minkowski Functional $\widehat{W}_1^{0,2}$	$\begin{bmatrix} 0.288 & 0 & 0.005 \\ 0 & 0.289 & 0 \\ 0.005 & 0 & 0.422 \end{bmatrix}$	[-]
Normalised Minkowski Functional $\widehat{W}_2^{0,2}$	$\begin{bmatrix} 0.258 & -0.021 & 0.003 \\ -0.021 & 0.289 & 0.002 \\ 0.003 & 0.002 & 0.452 \end{bmatrix}$	[-]
Anisotropy Index $\beta_1^{0,2}$	0.68	[-]
Anisotropy Index $\beta_2^{0,2}$	0.55	[-]
Permeability Computation Results		
Effective Porosity	0.34	[-]
Directional Permeability	$\begin{bmatrix} 13.24 & - & - \\ - & 13.68 & - \\ - & - & 13.11 \end{bmatrix}$	$[D]$

Sample 15: S9

Orthogonal Image Projections:

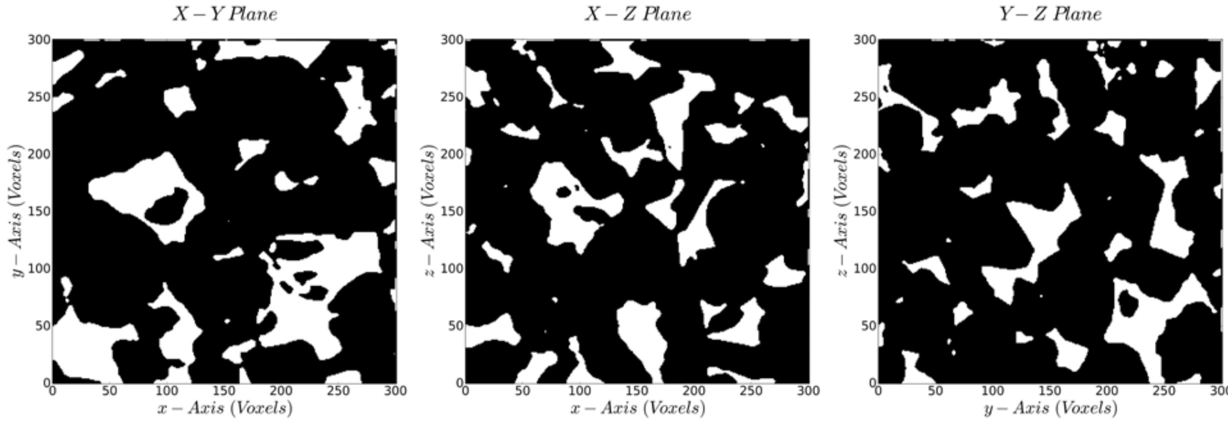

Appendix Figure 50 Orthogonal views of image S9. Views seen from front of sample.

Sample Description:

Aenean at tortor luctus purus euismod aliquet at eu metus. Pellentesque tempor ac libero laoreet ullamcorper. Suspendisse blandit ante id orci iaculis vestibulum id quis lorem. Morbi fermentum iaculis ipsum ut congue. Phasellus bibendum ornare diam, sed tempus lacus pharetra et. Aenean quis laoreet urna, interdum dictum tellus. Mauris congue suscipit tortor et commodo.

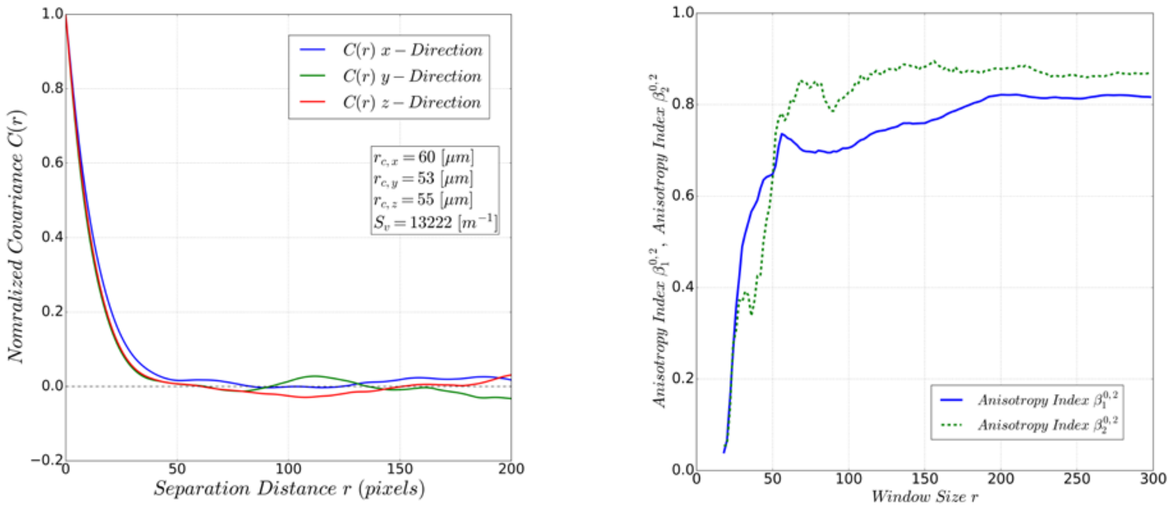

Appendix Figure 51:Left: Anisotropy indices derived from Minkowski tensor functionals. Right: Normalized directional Covariance of the S9 sample.

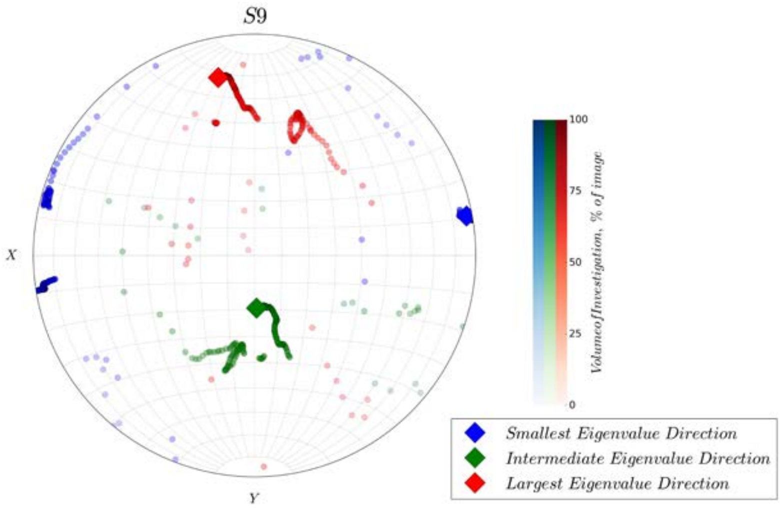

Appendix Figure 52: Stereonet projection of eigenvectors of Minkowski tensor $W_1^{0,2}$ of the S9 sample.

Results Summary		
Image Name	**S9**	
Rock Type	**Sandstone**	
Property	**Value**	**Unit**
Image Resolution	3.398	$[\mu m]$
Image Dimensions	(300, 300, 300)	(Nx, Ny, Nz) [voxel]
Covariance Analysis Results		
Porosity	0.22	[-]
Directional Characterstic Pore Size $[r_{c,x}, r_{c,y}, r_{c,z}]$	60,53,55	$[\mu m]$
Average Characteristic Pore Size $\bar{r_c}$	52	$[\mu m]$
Specific Surface Area	13222	$[m^{-1}]$
Minkowski Tensor Analysis		
Normalised Minkowski Functional $\widehat{W}_1^{0,2}$	$\begin{bmatrix} 0.301 & -0.012 & -0.002 \\ -0.012 & 0.359 & 0.009 \\ -0.002 & 0.009 & 0.339 \end{bmatrix}$	[-]
Normalised Minkowski Functional $\widehat{W}_2^{0,2}$	$\begin{bmatrix} 0.312 & -0.007 & -0.008 \\ -0.007 & 0.351 & 0.006 \\ -0.008 & 0.006 & 0.337 \end{bmatrix}$	[-]
Anisotropy Index $\beta_1^{0,2}$	0.82	[-]
Anisotropy Index $\beta_2^{0,2}$	0.87	[-]
Permeability Computation Results		
Effective Porosity	0.22	[-]
Directional Permeability	$\begin{bmatrix} 2.771 & - & - \\ - & 2.121 & - \\ - & - & 1.868 \end{bmatrix}$	$[D]$

Sample 16: C1

Orthogonal Image Projections:

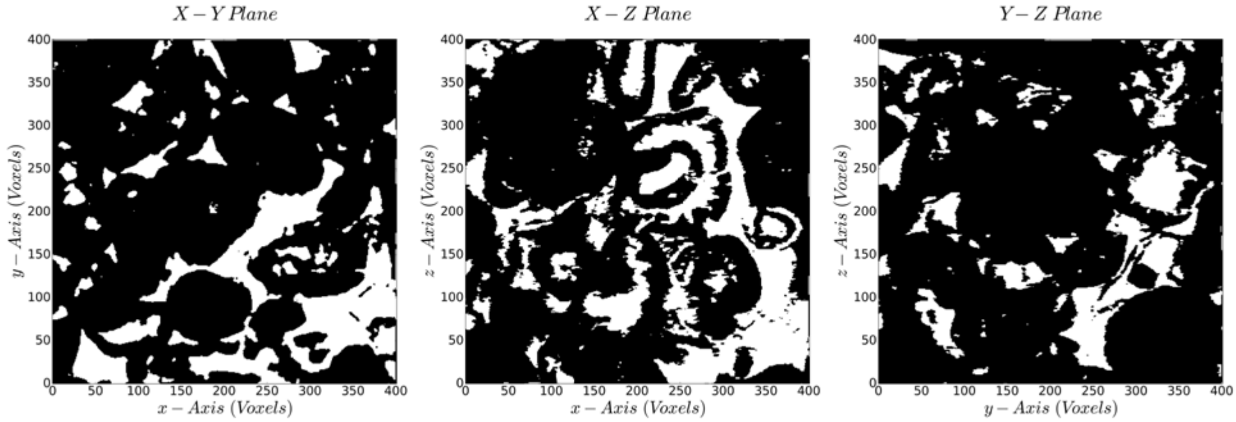

Appendix Figure 53 Orthogonal views of image C1. Views seen from front of sample.

Sample Description:

Aenean at tortor luctus purus euismod aliquet at eu metus. Pellentesque tempor ac libero laoreet ullamcorper. Suspendisse blandit ante id orci iaculis vestibulum id quis lorem. Morbi fermentum iaculis ipsum ut congue. Phasellus bibendum ornare diam, sed tempus lacus pharetra et. Aenean quis laoreet urna, interdum dictum tellus. Mauris congue suscipit tortor et commodo.

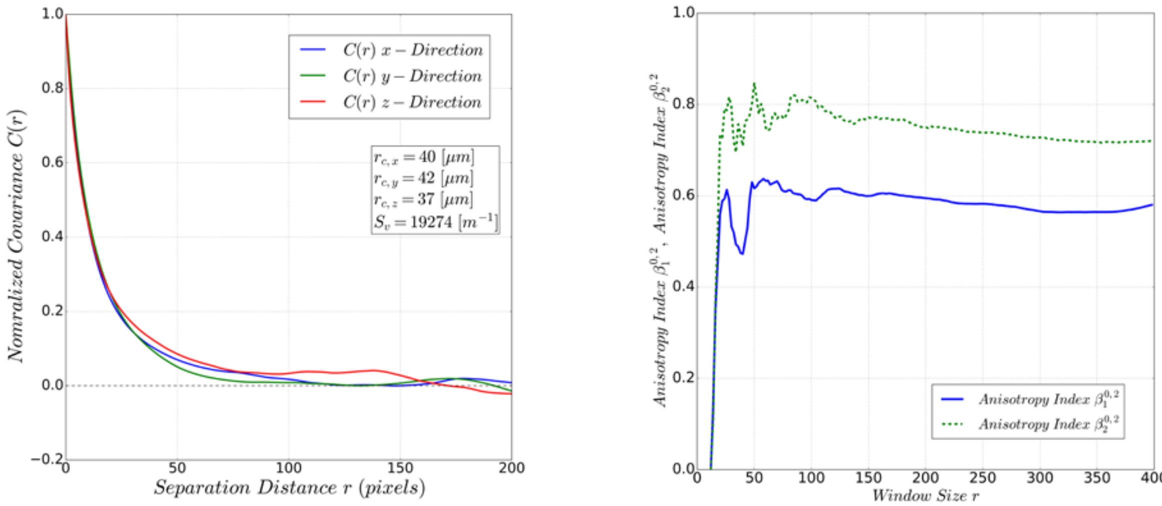

Appendix Figure 54:Left: Anisotropy indices derived from Minkowski tensor functionals. Right: Normalized directional Covariance of the C1 sample.

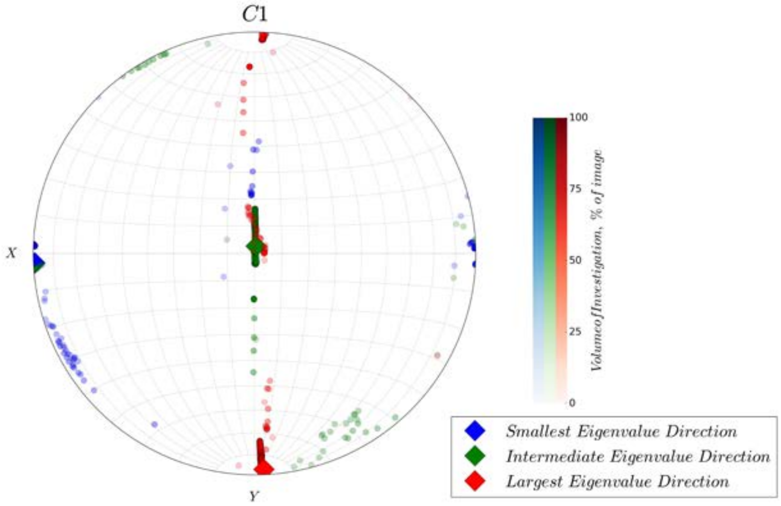

Appendix Figure 55: Stereonet projection of eigenvectors of Minkowski tensor $W_1^{0,2}$ of the C1 sample.

Results Summary		
Image Name	**C1**	
Rock Type	**Carbonate**	
Property	**Value**	**Unit**
Image Resolution	2.85	$[\mu m]$
Image Dimensions	(400, 400, 400)	(Nx, Ny, Nz) [voxel]
Covariance Analysis Results		
Porosity	0.23	[-]
Directional Characterstic Pore Size $[r_{c,x}, r_{c,y}, r_{c,z}]$	40,42,37	$[\mu m]$
Average Characteristic Pore Size $\bar{r_c}$	37	$[\mu m]$
Specific Surface Area	19274	$[m^{-1}]$
Minkowski Tensor Analysis		
Normalised Minkowski Functional $\widehat{W}_1^{0,2}$	$\begin{bmatrix} 0.285 & 0 & -0.007 \\ 0 & 0.263 & 0.002 \\ -0.007 & 0.002 & 0.453 \end{bmatrix}$	[-]
Normalised Minkowski Functional $\widehat{W}_2^{0,2}$	$\begin{bmatrix} 0.306 & 0 & 0 \\ 0 & 0.291 & 0 \\ 0 & 0 & 0.403 \end{bmatrix}$	[-]
Anisotropy Index $\beta_1^{0,2}$	0.58	[-]
Anisotropy Index $\beta_2^{0,2}$	0.72	[-]
Permeability Computation Results		
Effective Porosity	0.23	[-]
Directional Permeability	$\begin{bmatrix} 0.795 & - & - \\ - & 1.488 & - \\ - & - & 1.067 \end{bmatrix}$	$[D]$

Sample 17: C2

Orthogonal Image Projections:

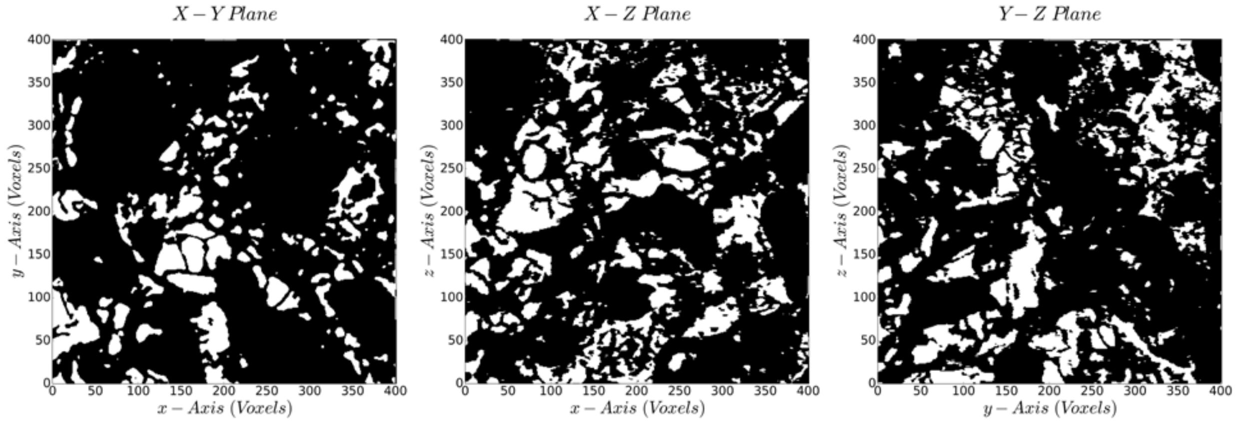

Appendix Figure 56 Orthogonal views of image C2. Views seen from front of sample.

Sample Description:

Aenean at tortor luctus purus euismod aliquet at eu metus. Pellentesque tempor ac libero laoreet ullamcorper. Suspendisse blandit ante id orci iaculis vestibulum id quis lorem. Morbi fermentum iaculis ipsum ut congue. Phasellus bibendum ornare diam, sed tempus lacus pharetra et. Aenean quis laoreet urna, interdum dictum tellus. Mauris congue suscipit tortor et commodo.

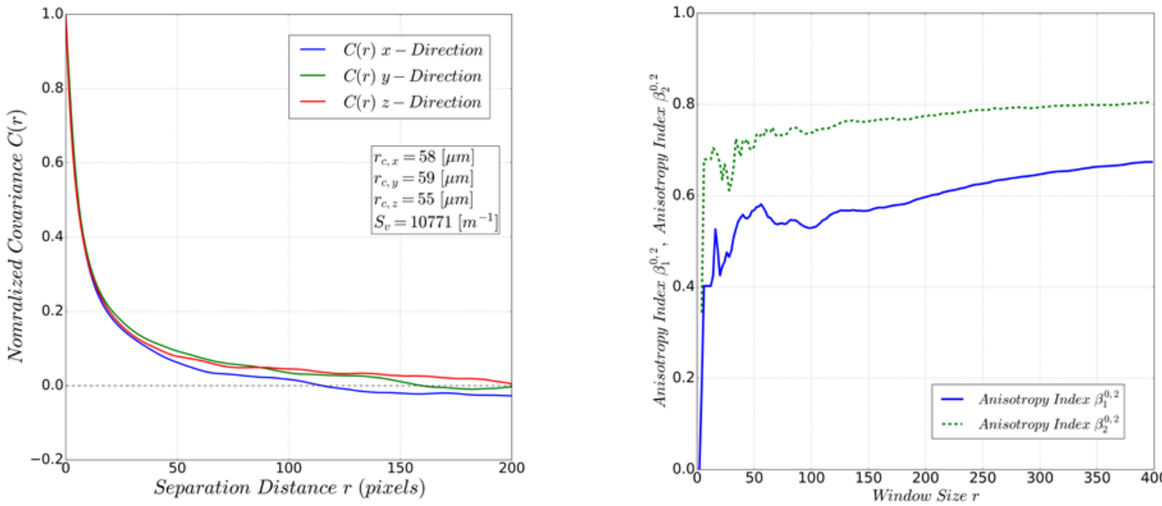

Appendix Figure 57:Left: Anisotropy indices derived from Minkowski tensor functionals. Right: Normalized directional Covariance of the C2 sample.

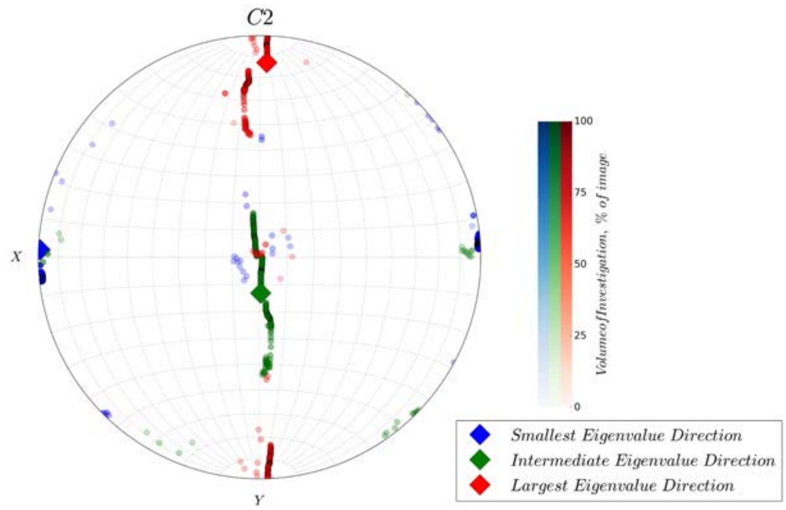

Appendix Figure 58: Stereonet projection of eigenvectors of Minkowski tensor $W_1^{0,2}$ of the C2 sample.

Results Summary		
Image Name	**C2**	
Rock Type	**Carbonate**	
Property	**Value**	**Unit**
Image Resolution	5.345	$[\mu m]$
Image Dimensions	(400, 400, 400)	(Nx, Ny, Nz) [voxel]
Covariance Analysis Results		
Porosity	0.17	[-]
Directional Characterstic Pore Size $[r_{c,x}, r_{c,y}, r_{c,z}]$	58,59,55	$[\mu m]$
Average Characteristic Pore Size $\bar{r_c}$	52	$[\mu m]$
Specific Surface Area	10771	$[m^{-1}]$
Minkowski Tensor Analysis		
Normalised Minkowski Functional $\widehat{W}_1^{0,2}$	$\begin{bmatrix} 0.292 & 0.002 & -0.005 \\ 0.002 & 0.285 & 0.001 \\ -0.005 & 0.001 & 0.423 \end{bmatrix}$	[-]
Normalised Minkowski Functional $\widehat{W}_2^{0,2}$	$\begin{bmatrix} 0.311 & 0 & -0.003 \\ 0 & 0.308 & 0 \\ -0.003 & 0 & 0.382 \end{bmatrix}$	[-]
Anisotropy Index $\beta_1^{0,2}$	0.67	[-]
Anisotropy Index $\beta_2^{0,2}$	0.80	[-]
Permeability Computation Results		
Effective Porosity	0.168	[-]
Directional Permeability	$\begin{bmatrix} 0.039 & - & - \\ - & 0.163 & - \\ - & - & 0.018 \end{bmatrix}$	$[D]$

Sample 18: Isotropic $r_{1,2,3} = 1.2$

Orthogonal Image Projections:

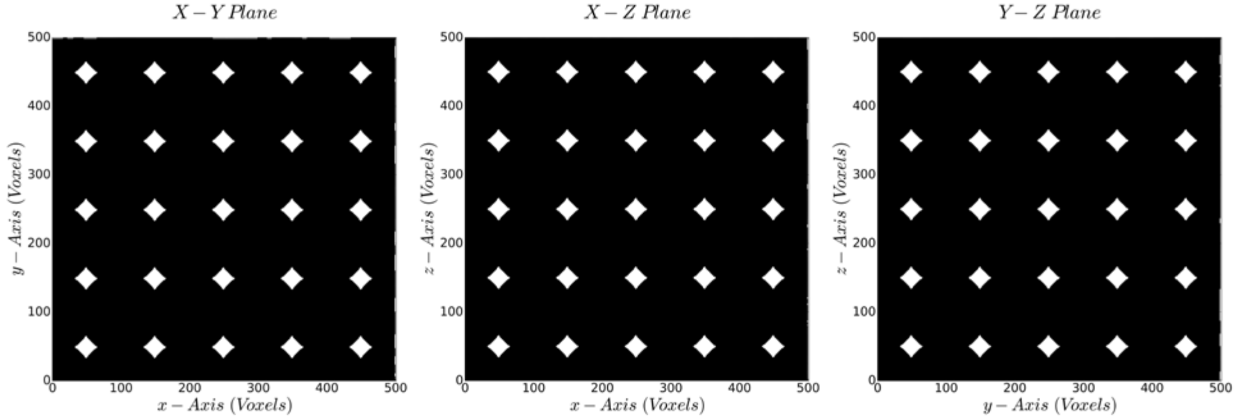

Appendix Figure 59 Orthogonal views of image Isotropic $r_{1,2,3} = 1.2$. Views seen from front of sample.

Sample Description:

Aenean at tortor luctus purus euismod aliquet at eu metus. Pellentesque tempor ac libero laoreet ullamcorper. Suspendisse blandit ante id orci iaculis vestibulum id quis lorem. Morbi fermentum iaculis ipsum ut congue. Phasellus bibendum ornare diam, sed tempus lacus pharetra et. Aenean quis laoreet urna, interdum dictum tellus. Mauris congue suscipit tortor et commodo.

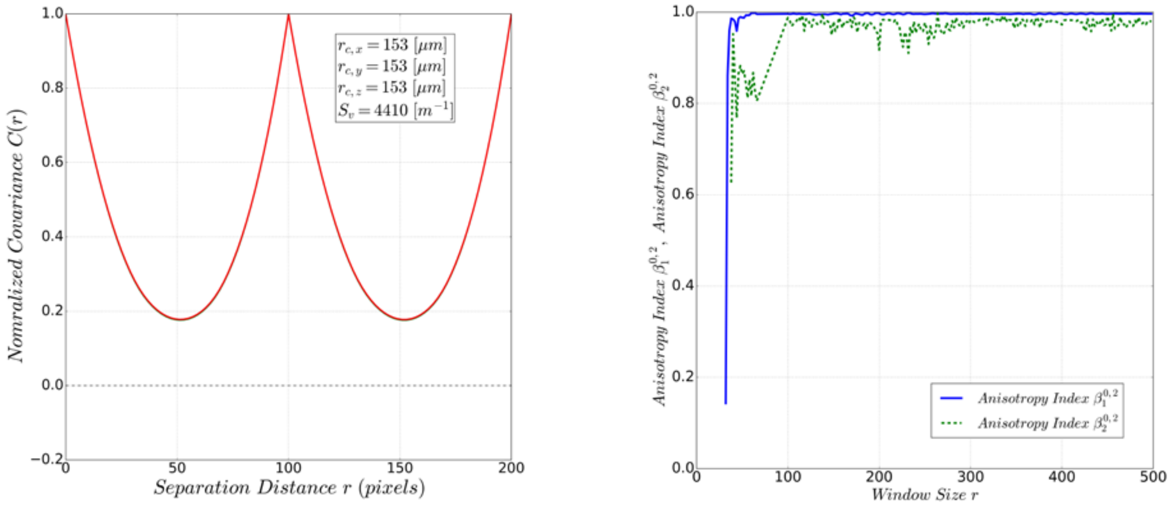

Appendix Figure 61:Left: Anisotropy indices derived from Minkowski tensor functionals. Right: Normalized directional Covariance of the Isotropic $r_{1,2,3} = 1.2$ sample.

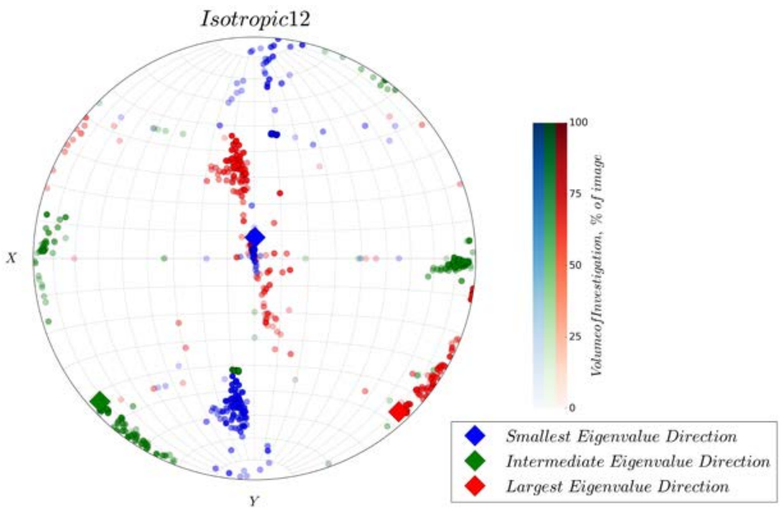

Appendix Figure 60: Stereonet projection of eigenvectors of Minkowski tensor $W_1^{0,2}$ of the Isotropic $r_{1,2,3} = 1.2$ sample.

Results Summary		
Image Name	**Isotropic $r_{1,2,3} = 1.2$**	
Rock Type	**Parametric**	
Property	**Value**	**Unit**
Image Resolution	2.0	$[\mu m]$
Image Dimensions	(500, 500, 500)	(Nx, Ny, Nz) [voxel]
Covariance Analysis Results		
Porosity	0.21	[-]
Directional Characterstic Pore Size $[r_{c,x}, r_{c,y}, r_{c,z}]$	153,153,153	$[\mu m]$
Average Characteristic Pore Size $\bar{r_c}$	153	$[\mu m]$
Specific Surface Area	4410	$[m^{-1}]$
Minkowski Tensor Analysis		
Normalised Minkowski Functional $\widehat{W}_1^{0,2}$	$\begin{bmatrix} 0.333 & 0 & 0 \\ 0 & 0.333 & 0 \\ 0 & 0 & 0.333 \end{bmatrix}$	[-]
Normalised Minkowski Functional $\widehat{W}_2^{0,2}$	$\begin{bmatrix} 0.333 & -0.003 & -0.002 \\ -0.003 & 0.333 & -0.002 \\ -0.002 & -0.002 & 0.333 \end{bmatrix}$	[-]
Anisotropy Index $\beta_1^{0,2}$	1.0	[-]
Anisotropy Index $\beta_2^{0,2}$	0.98	[-]
Permeability Computation Results		
Effective Porosity	0.21	[-]
Directional Permeability	$\begin{bmatrix} 8.621 & - & - \\ - & 8.618 & - \\ - & - & 8.623 \end{bmatrix}$	$[D]$

Sample 19: Isotropic $r_{1,2,3} = 1.3$

Orthogonal Image Projections:

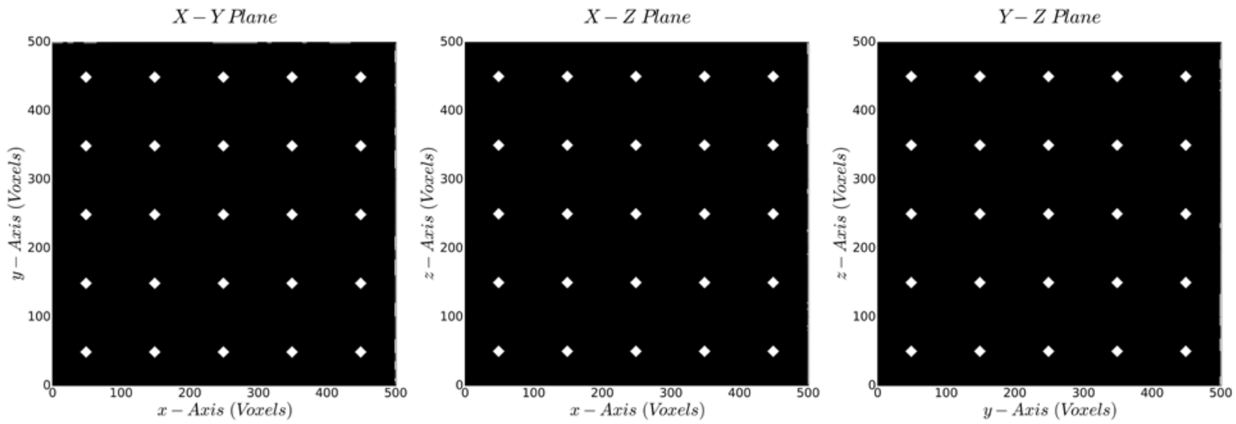

Appendix Figure 62 Orthogonal views of image Isotropic $r_{1,2,3} = 1.3$. *Views seen from front of sample.*

Sample Description:
Aenean at tortor luctus purus euismod aliquet at eu metus. Pellentesque tempor ac libero laoreet ullamcorper. Suspendisse blandit ante id orci iaculis vestibulum id quis lorem. Morbi fermentum iaculis ipsum ut congue. Phasellus bibendum ornare diam, sed tempus lacus pharetra et. Aenean quis laoreet urna, interdum dictum tellus. Mauris congue suscipit tortor et commodo.

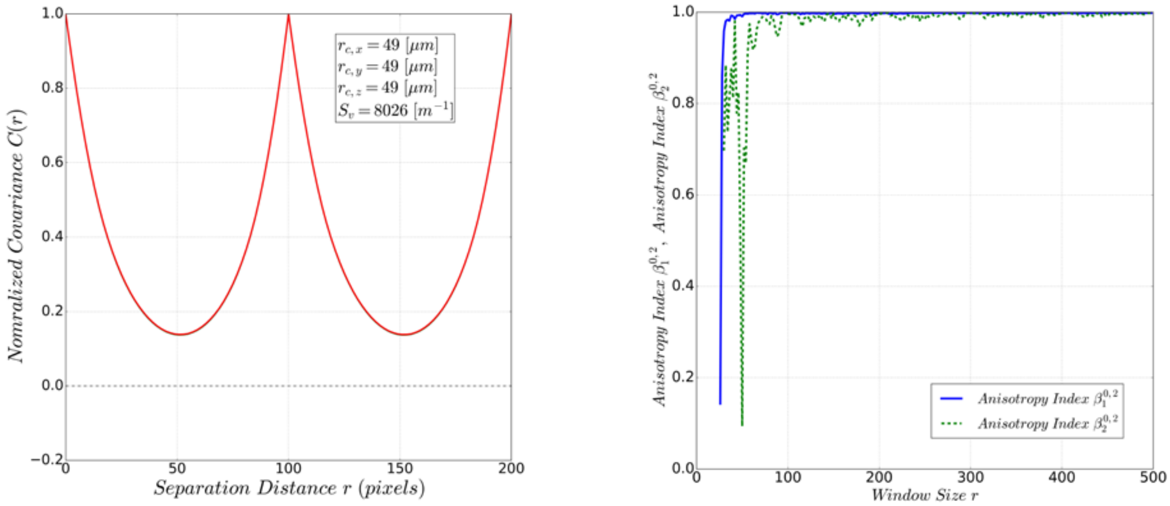

Appendix Figure 64:Left: Anisotropy indices derived from Minkowski tensor functionals. Right: Normalized directional Covariance of the Isotropic $r_{1,2,3} = 1.3$ *sample.*

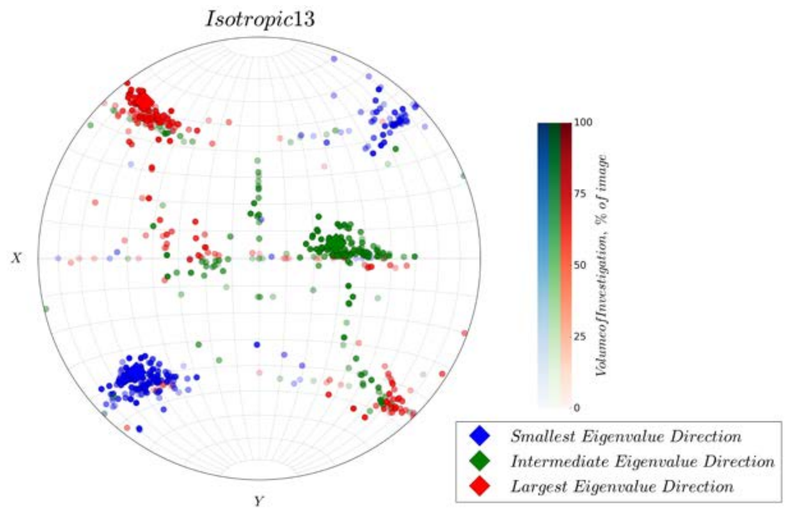

Appendix Figure 63: Stereonet projection of eigenvectors of Minkowski tensor $W_1^{0,2}$ *of the Isotropic* $r_{1,2,3} = 1.3$*sample.*

Results Summary		
Image Name	**Isotropic $r_{1,2,3} = 1.3$**	
Rock Type	**Parametric**	
Property	**Value**	**Unit**
Image Resolution	2.0	$[\mu m]$
Image Dimensions	(500, 500, 500)	(Nx, Ny, Nz) [voxel]
Covariance Analysis Results		
Porosity	0.11	[-]
Directional Characterstic Pore Size $[r_{c,x}, r_{c,y}, r_{c,z}]$	49,49,49	$[\mu m]$
Average Characteristic Pore Size $\bar{r_c}$	49	$[\mu m]$
Specific Surface Area	8026	$[m^{-1}]$
Minkowski Tensor Analysis		
Normalised Minkowski Functional $\widehat{W}_1^{0,2}$	$\begin{bmatrix} 0.333 & 0 & 0 \\ 0 & 0.333 & 0 \\ 0 & 0 & 0.333 \end{bmatrix}$	[-]
Normalised Minkowski Functional $\widehat{W}_2^{0,2}$	$\begin{bmatrix} 0.333 & 0 & 0 \\ 0 & 0.333 & 0 \\ 0 & 0 & 0.333 \end{bmatrix}$	[-]
Anisotropy Index $\beta_1^{0,2}$	1.0	[-]
Anisotropy Index $\beta_2^{0,2}$	1.0	[-]
Permeability Computation Results		
Effective Porosity	0.11	[-]
Directional Permeability	$\begin{bmatrix} 0.931 & - & - \\ - & 0.932 & - \\ - & - & 0.944 \end{bmatrix}$	$[D]$

Sample 20: Isotropic $r_{1,2,3} = 1.4$

Orthogonal Image Projections:

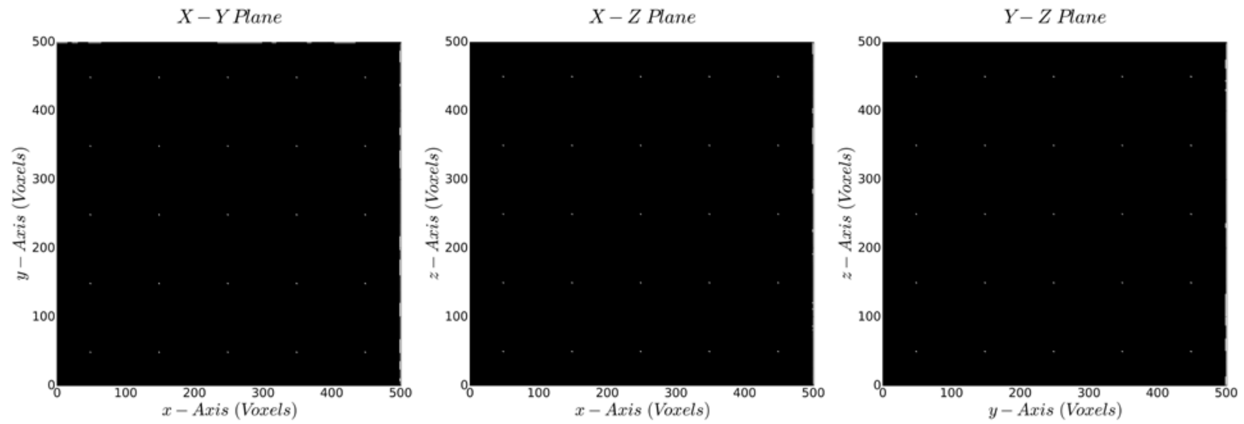

Appendix Figure 65 Orthogonal views of image Isotropic $r_{1,2,3} = 1.4$. Views seen from front of sample.

Sample Description:
Aenean at tortor luctus purus euismod aliquet at eu metus. Pellentesque tempor ac libero laoreet ullamcorper. Suspendisse blandit ante id orci iaculis vestibulum id quis lorem. Morbi fermentum iaculis ipsum ut congue. Phasellus bibendum ornare diam, sed tempus lacus pharetra et. Aenean quis laoreet urna, interdum dictum tellus. Mauris congue suscipit tortor et commodo.

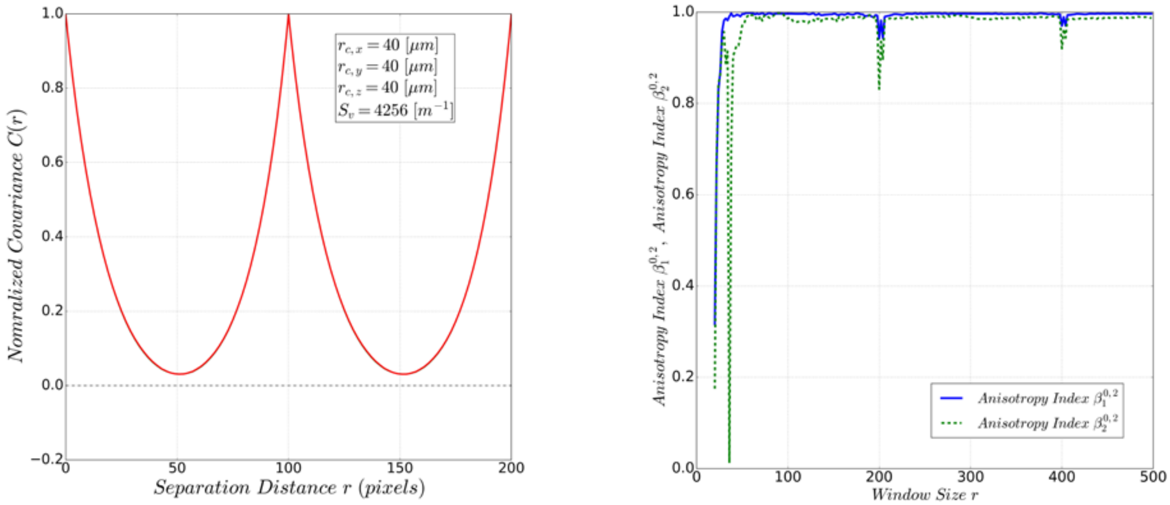

Appendix Figure 67:Left: Anisotropy indices derived from Minkowski tensor functionals. Right: Normalized directional Covariance of the ropic $r_{1,2,3} = 1.4$ sample.

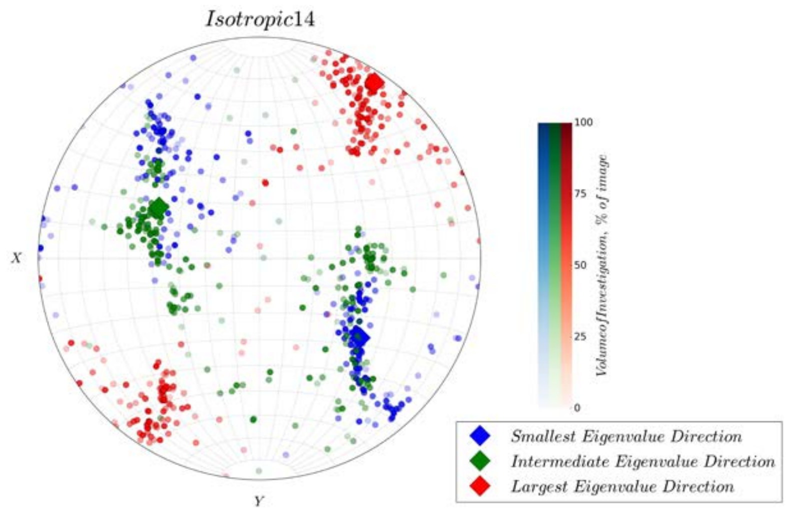

Appendix Figure 66: Stereonet projection of eigenvectors of Minkowski tensor $W_1^{0,2}$ of the ropic $r_{1,2,3} = 1.4$ sample.

Results Summary		
Image Name	**Isotropic $r_{1,2,3} = 1.4$**	
Rock Type	**Parametric**	
Property	**Value**	**Unit**
Image Resolution	2.0	$[\mu m]$
Image Dimensions	(500, 500, 500)	(Nx, Ny, Nz) [voxel]
Covariance Analysis Results		
Porosity	0.04	[-]
Directional Characterstic Pore Size $[r_{c,x}, r_{c,y}, r_{c,z}]$	40,40,40	$[\mu m]$
Average Characteristic Pore Size $\bar{r_c}$	40	$[\mu m]$
Specific Surface Area	4256	$[m^{-1}]$
Minkowski Tensor Analysis		
Normalised Minkowski Functional $\widehat{W}_1^{0,2}$	$\begin{bmatrix} 0.332 & 0 & 0 \\ 0 & 0.333 & 0 \\ 0 & 0 & 0.333 \end{bmatrix}$	[-]
Normalised Minkowski Functional $\widehat{W}_2^{0,2}$	$\begin{bmatrix} 0.332 & 0 & 0 \\ 0 & 0.332 & 0 \\ 0 & 0 & 0.336 \end{bmatrix}$	[-]
Anisotropy Index $\beta_1^{0,2}$	0.99	[-]
Anisotropy Index $\beta_2^{0,2}$	0.98	[-]
Permeability Computation Results		
Effective Porosity	0.042	[-]
Directional Permeability	$\begin{bmatrix} 0.303 & - & - \\ - & 0.303 & - \\ - & - & 0.303 \end{bmatrix}$	$[mD]$

Sample 21: Anisotropic $r_{1,2} = 1.3$ $r_3 = 1.4$

Orthogonal Image Projections:

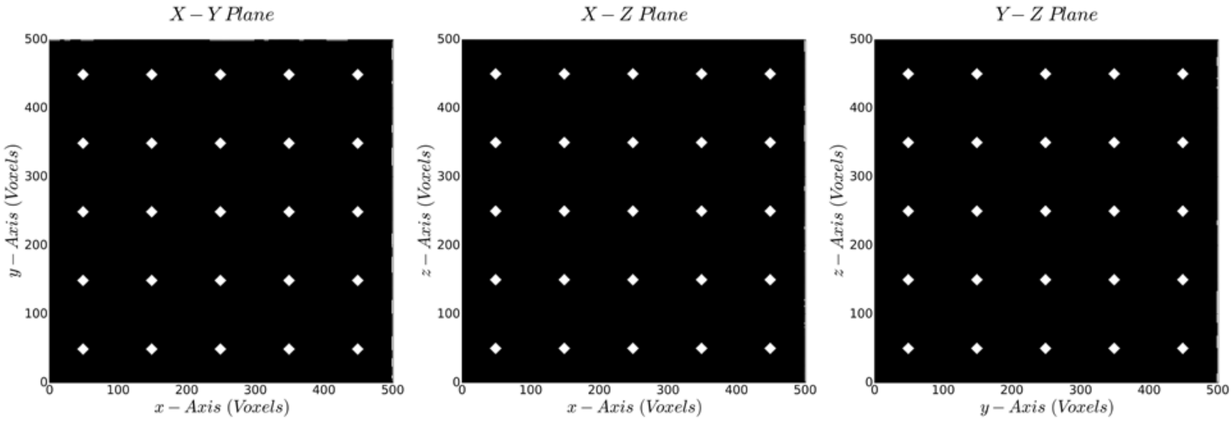

Appendix Figure 68 Orthogonal views of image Anisotropic $r_{1,2} = 1.3$ $r_3 = 1.4$. Views seen from front of sample.

Sample Description:
Aenean at tortor luctus purus euismod aliquet at eu metus. Pellentesque tempor ac libero laoreet ullamcorper. Suspendisse blandit ante id orci iaculis vestibulum id quis lorem. Morbi fermentum iaculis ipsum ut congue. Phasellus bibendum ornare diam, sed tempus lacus pharetra et. Aenean quis laoreet urna, interdum dictum tellus. Mauris congue suscipit tortor et commodo.

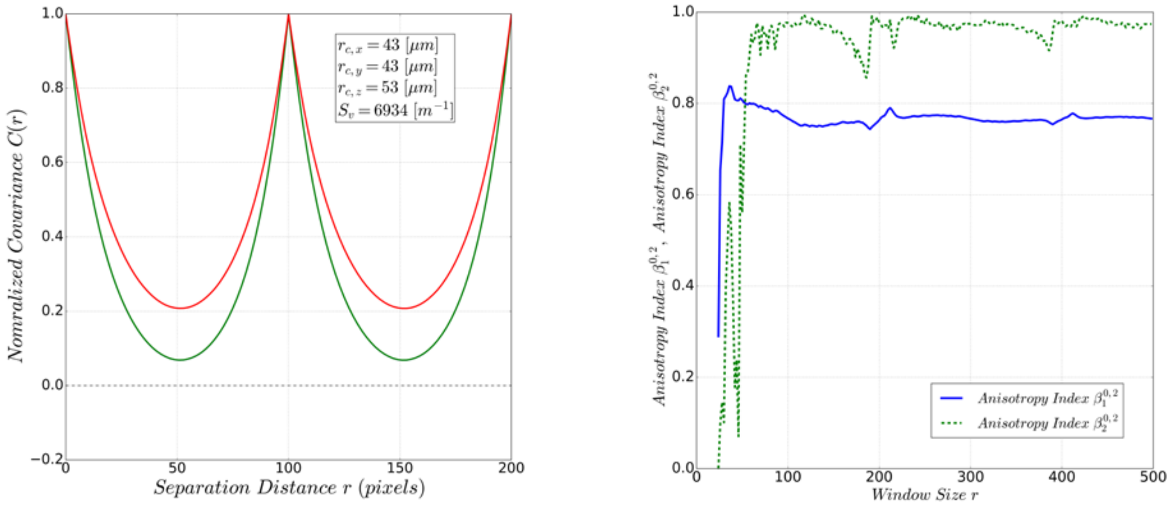

Appendix Figure 70:Left: Anisotropy indices derived from Minkowski tensor functionals. Right: Normalized directional Covariance of the Anisotropic $r_{1,2} = 1.3$ $r_3 = 1.4$ sample.

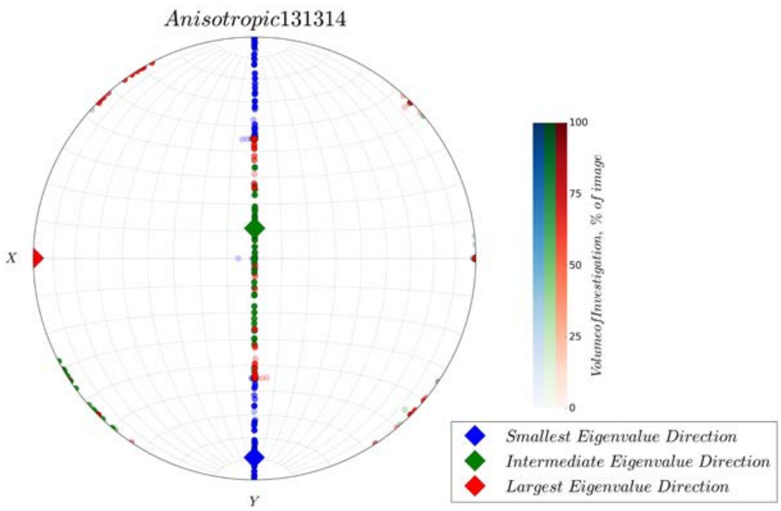

Appendix Figure 69: Stereonet projection of eigenvectors of Minkowski tensor $W_1^{0,2}$ of the Anisotropic $r_{1,2} = 1.3$ $r_3 = 1.4$ sample.

Results Summary		
Image Name	**Anisotropic $r_{1,2} = 1.3\ r_3 = 1.4$**	
Rock Type	**Parametric**	
Property	**Value**	**Unit**
Image Resolution	2.0	$[\mu m]$
Image Dimensions	(500, 500, 500)	(Nx, Ny, Nz) [voxel]
Covariance Analysis Results		
Porosity	0.08	[-]
Directional Characterstic Pore Size $[r_{c,x}, r_{c,y}, r_{c,z}]$	43,43,53	$[\mu m]$
Average Characteristic Pore Size $\bar{r_c}$	44	$[\mu m]$
Specific Surface Area	6934	$[m^{-1}]$
Minkowski Tensor Analysis		
Normalised Minkowski Functional $\widehat{W}_1^{0,2}$	$\begin{bmatrix} 0.361 & 0 & 0 \\ 0 & 0.361 & 0 \\ 0 & 0 & 0.277 \end{bmatrix}$	[-]
Normalised Minkowski Functional $\widehat{W}_2^{0,2}$	$\begin{bmatrix} 0.336 & 0 & 0 \\ 0 & 0.336 & 0 \\ 0 & 0 & 0.328 \end{bmatrix}$	[-]
Anisotropy Index $\beta_1^{0,2}$	0.77	[-]
Anisotropy Index $\beta_2^{0,2}$	0.97	[-]
Permeability Computation Results		
Effective Porosity	0.08	[-]
Directional Permeability	$\begin{bmatrix} 0.130 & - & - \\ - & 0.130 & - \\ - & - & 0.876 \end{bmatrix}$	$[D]$

Sample 22: Anisotropic $r_{1,2} = 1.2$ $r_3 = 1.4$

Orthogonal Image Projections:

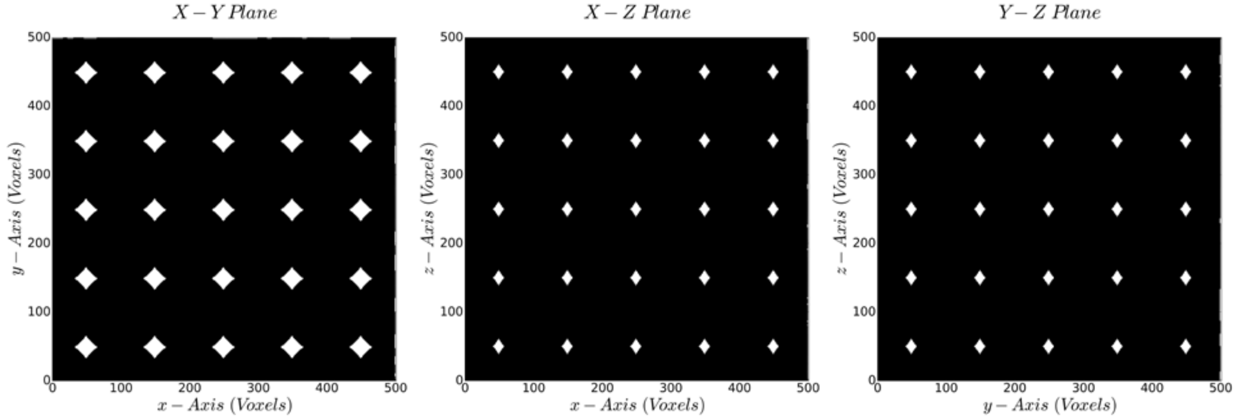

Appendix Figure 71 Orthogonal views of image Anisotropic $r_{1,2} = 1.2$ $r_3 = 1.4$. Views seen from front of sample.

Sample Description:
Aenean at tortor luctus purus euismod aliquet at eu metus. Pellentesque tempor ac libero laoreet ullamcorper. Suspendisse blandit ante id orci iaculis vestibulum id quis lorem. Morbi fermentum iaculis ipsum ut congue. Phasellus bibendum ornare diam, sed tempus lacus pharetra et. Aenean quis laoreet urna, interdum dictum tellus. Mauris congue suscipit tortor et commodo.

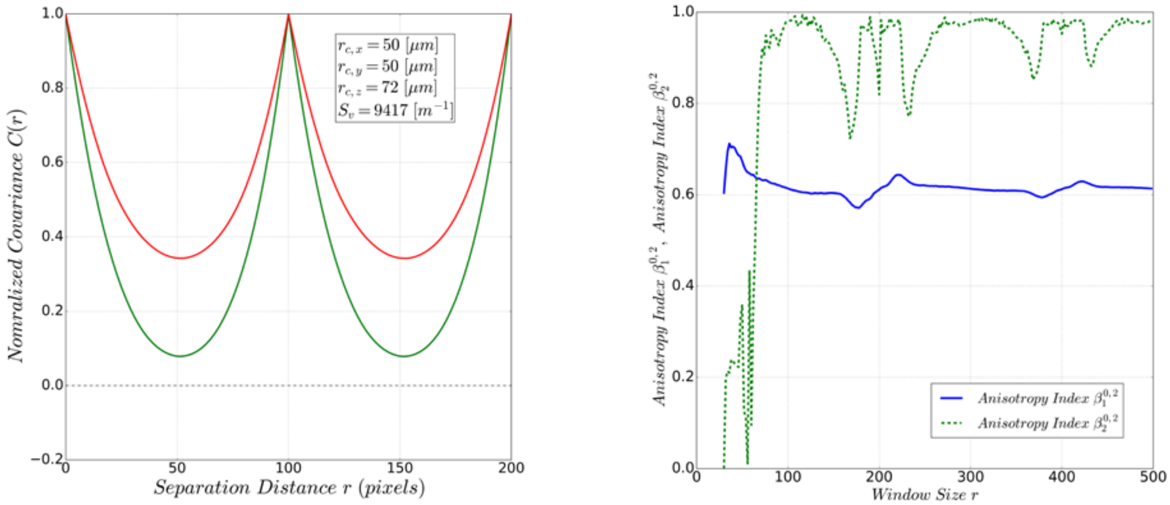

Appendix Figure 73:Left: Anisotropy indices derived from Minkowski tensor functionals. Right: Normalized directional Covariance of the Anisotropic $r_{1,2} = 1.2$ $r_3 = 1.4$ sample.

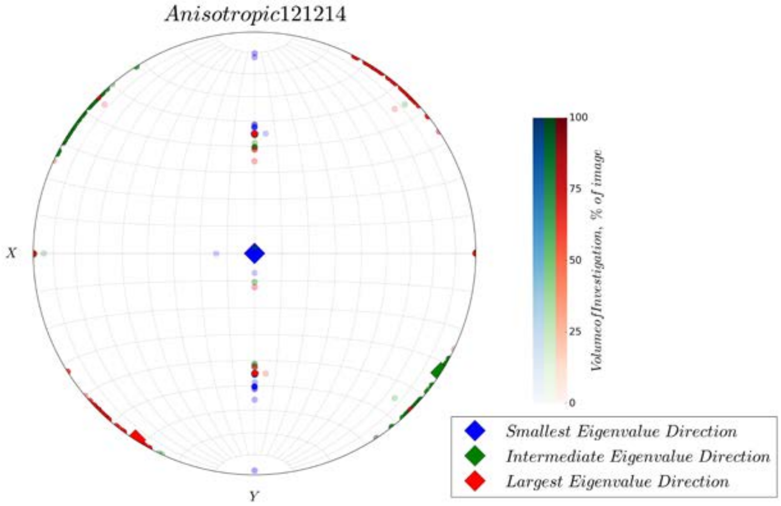

Appendix Figure 72: Stereonet projection of eigenvectors of Minkowski tensor $W_1^{0,2}$ of the Anisotropic $r_{1,2} = 1.2$ $r_3 = 1.4$ sample.

Results Summary		
Image Name	**Anisotropic $r_{1,2} = 1.2$ $r_3 = 1.4$**	
Rock Type	**Parametric**	
Property	**Value**	**Unit**
Image Resolution	2.0	$[\mu m]$
Image Dimensions	(500, 500, 500)	(Nx, Ny, Nz) [voxel]
Covariance Analysis Results		
Porosity	0.15	[-]
Directional Characterstic Pore Size $[r_{c,x}, r_{c,y}, r_{c,z}]$	50,50,72	$[\mu m]$
Average Characteristic Pore Size $\bar{r_c}$	53	$[\mu m]$
Specific Surface Area	9417	$[m^{-1}]$
Minkowski Tensor Analysis		
Normalised Minkowski Functional $\widehat{W}_1^{0,2}$	$\begin{bmatrix} 0.383 & 0 & 0 \\ 0 & 0.383 & 0 \\ 0 & 0 & 0.235 \end{bmatrix}$	[-]
Normalised Minkowski Functional $\widehat{W}_2^{0,2}$	$\begin{bmatrix} 0.335 & 0 & 0.002 \\ 0 & 0.334 & 0.002 \\ 0.002 & 0.002 & 0.331 \end{bmatrix}$	[-]
Anisotropy Index $\beta_1^{0,2}$	0.61	[-]
Anisotropy Index $\beta_2^{0,2}$	0.98	[-]
Permeability Computation Results		
Effective Porosity	0.15	[-]
Directional Permeability	$\begin{bmatrix} 1.3645 & - & - \\ - & 1.369 & - \\ - & - & 7.557 \end{bmatrix}$	$[D]$